# Desing and Simulation of Advanced Fiber Optic Sensors for High Energy Physics Application

Andrea Saccomanno
Department of Biomedical, Electronic and Telecommunication Engineering
University of Naples "Federico II"

A thesis submitted for the degree of
*PhilosophiæDoctor (PhD) in Electronic and Telecommunication Engineering*
Academic Year 2011/2012

Tutor: Prof. Giovanni Breglio

Coordinator of the Ph.D. course: Prof. Niccoló Rinaldi

PhD student: Eng. Andrea Saccomanno

Day of the defense: April 23, 2013

To Dalila,
my future wife, mother of my sons,
and the woman I want to grow old with.

# Acknowledgements

First, I would like to acknowledge my tutor, Prof. Giovanni Breglio for his aid, for his precious advice and for his patience. He has supported me and guided me during this long journey, untill reaching this important goal, that would never have been made without him!

A special thanks is due to Prof. Andrea Cusano, a friend, first of all! He guided me in the post-degree choices and collaborated with me in much of my PhD activities.

A special thought goes to my friend Giuseppe Lanza (simply *Peppe*), who is fighting a hard battle! Go Peppe, hold on! I'm with you!

This thesis work was made possible by the strict cooperation with the researcher from University of Sannio, National Research Council (CNR) and the European Organization for Nuclear Research (CERN).

Finally, a special thanks is due to my dear colleagues from Optolab for the funny moment spent together: thanks to Luca, Lucio, Martina, Matteo, Michele.

# Preface

The research activity of the Eng. Andrea Saccomanno is focused on the area of fiber optic sensors for sensing applications and is carried out in collaboration with the Institute for Composite and Biomedical Materials (IMCB) of the CNR in Napoli, Italy, with the Department of Engineering of the University of Sannio in Benevento, Italy, with the European Organization for Nuclear Research (CERN) in Geneva, Switzerland and with the Optosmart s.r.l.. His field of interest is in the area of optoelectronic sensors dealing with structural health monitoring, temperature monitoring, novel magnetic field sensor by using fiber Bragg grating. He is author or coauthor of 3 publications on scientific journals and 2 communications to international conferences and 1 communication to national conference. He attended several PhD courses and seminaries, national and international conferences and workshops.

# Contents

# List of Figures

# List of Tables

# Abstract

In the last two decades, Fiber Bragg Grating (FBG) sensor were been widely studied and employed in temperature and strain sensing application. Due to their high potentiality in term of radiation hardness and EMI insensitivity, they constitute the ideal device to operate in harsh environments, under ionizing radiation and strong magnetic fields. This thesis work is focused on the research, development and simulation of novel sensors and monitoring systems suitable to operete in these environmental conditions.In particular, the monitoring applications regards room temperature of Compact Muon Solenoid (CERN), cryogenic temperature (up to 4.2 K) of the powerful cooling system of the LHC's superconducting magnets, and magnetic field with magnetostrictive and magneto-optic approaches.

# Introduction

This thesis work is focuses on the study and development of novel sensors and optoelectronic sensing systems based on Fiber Bragg Grating (FBG), suitable to operate in harsh environments, characterized by high magnetic fields and strong ionizing radiation that make useless the classical electronic sensors. The sensing applications for these kind of devices and systems, respond to the needs of High Energy Physics (HEP) experiment sites, in which it is vital to have efficient and reliable measurement systems.
In the first chapter, the theoretical principles underlying the FBG will be tackled by using a very thorough formalism that is useful to define a mathematical and numerical model for the devices under investigation. Preliminarily, the main industrial fields in which the use of optoelectronic sensors assumes fundamental importance, will be examined. On the basis of the specifications resulting from the analysis of such operative environments, the research activities exposed in the thesis, including the applications for HEP, were defined.
Then, will be presented the main research topics addressed that have led, in some cases, to the development and implementation of innovative sensing solutions and novel techniques of sensor calibration:

- Quasi-distributed sensing systems based on FBG with ceramic coating, for continuous temperature monitoring inside the structure of the Compact Muon Solenoid (CMS) at CERN; a thrust application of the Wavelength Division Multiplexing (WDM) adopted to maximize the number of sensing-point per channel with the highest degree of reliability as possible.

- FBG sensors for cryogenic temperature sensing in the range from 77 K to 4.2 K, made by the integration of optical fiber sensors with high-CTE (Coefficient of

Thermal Expansion) materials (PTFE, PMMA, Epoxy resin), for the monitoring of the supermagnet cooling systems of the Large Hadron Collider (LHC) at CERN.

- Definition of novel calibration methods based on look-up-table (LUT) for the dynamic calibration of cryogenic FBG sensors, in quasi-static conditions.
- FBG magnetic sensors integrated with a magnetostrictive material rod to transduce the applied magnetic field in strain measurements.
- Novel magnetic sensors based on a clad-etched FBG integrated by magnetic fluids, whose changes their refractive index as a function of the applied magnetic field.

**Keywords:** Fiber Bragg grating sensors, High Energy Physics, temperature sensing, Wavelength Division Multiplexing, cryogenic sensors, magnetic sensors, magnetic fluid, FEM simulation.

# Chapter 1

# Fiber Bragg Grating sensors

Over the last few decades, Fiber Bragg Grating sensors (FBGs) have attracted particular attention in the scientific community, becoming widely known and popular within and out the photonics community and seen a rise in their utilization and commercial growth. The capability of FBGs to measure a large variety of parameters such as strain, temperature and pressure and many others coupled with their flexibility of design to be used as single point or multi-point sensing arrays and their relative low cost, make them ideal devices to be adopted for a multitude of different sensing applications and implemented in different fields and industries. This chapter first summarizes the theoretical background on which FBGs are based. Successively the major milestones of their technological evolution in thirty years from the discovery of Kenneth Hill in 1978 are discussed. Finally, a brief view on the more relevant FBG industrial applications, is proposed.

## 1.1 Fundamentals of Fiber Bragg Gratings

The propagation of an electromagnetic field in optical fiber is studied starting by the classical form of Maxwell's equations with appropriate boundary conditions. This problem is a particular case of the wave propagation in a dielectric waveguide in which the geometry is cylindrical and the propagation takes in a longitudinal way with respect of the fiber axis. The problem is simplified by taking into account the hypothesis of "weak guidance" [(1)], which permits to decompose the propagative modes in an orthogonal set of transversely polarized modes [(2)]. In optical fibers have been found very often some imperfection including inhomogeneity in the core refractive index or small changes in the size of the fiber core. Imperfections or disruption (e.g. bending) may give rise to mode coupling. In the presence of perturbations a portion of electromagnetic power will be transferred to other guided modes and also to radiative modes. The power transfer to other modes causes distortion of the signal, since each guided mode propagates to its group velocity; also the power transfer to the radiative modes causes losses, since the power is no longer confined in the fiber core. The mode coupling is instead widely desired in particular configurations such as Fiber Bragg Gratings (FBG) or dielectric antennas; in FBG, by means of periodical perturbation in the core refractive index, the mode coupling produces an interferometric phenomena that brings to spectral distortion of the optical signal. Also, in dielectric antennas, the mode coupling in the guiding layer excites radiative modes absorbing radiated power from another source. The most common technique used to solve this electromagnetic problems is the Coupled Mode Theory (CMT). This technique follows the formalism illustrated in [(2)]. It is assumed that the modes of an unperturbed guide do not change in presence of such perturbations. This approach leads to a set of a first order differential equations useful to study the amplitude variation of the fields along the fiber, which has analytical solution for a uniform sinusoidal perturbation. In the following subsection a formal treatise of the CMT is reported, based on modal expansion [(3)].

### 1.1.1 Coupled Mode Theory (CMT)

The Coupled Mode Theory (CMT) is an important mathematical instrument useful to study the complex phenomena of the mode coupling. It aims to solve the Maxwell's equation for a perturbed waveguide assuming that the electric field $\mathbf{E}$ can be expressed as a expansion of ideal modes by two summation: the first on the $l$-guided modes, given by the product between the transversal field distribution associated with the $\mu$-th guided mode $\mathcal{E}_{\mu,t}$ and an amplitude term $A_\mu(z)$ associated with the mode; the second on all the modes (TE, TM, EH, HE) of the integral defined on the continuous set of the radiative modes, give by the product between the transversal field distribution associated with the $\rho$-th radiative mode $\mathcal{E}_{\rho,t}$ and ad amplitude term $A_\rho(z)$ associated with the mode.

$$\mathbf{E}_t = \frac{1}{2}\sum_{\mu=1}^{l}[A_\mu(z)\mathcal{E}_{\mu,t}e^{i(\omega t-\beta_\mu z)}] + \sum\int_{\rho=0}^{\infty}A_\rho(z)\mathcal{E}_{\rho,t}e^{i(\omega t-\beta_\rho z)d\rho} \tag{1.1}$$

The modes fulfill the unperturbed wave's equation:

$$\nabla^2\mathbf{E} = \mu_0\epsilon_0\frac{\partial^2\mathbf{E}}{\partial t^2} + \mu_0\frac{\partial^2\mathbf{P}}{\partial t^2} \tag{1.2}$$

To derive the equation for the coupled modes must be included the perturbation effect, in the hypothesis of a unperturbed waveguide the modes do not change. By considering the effect of a grating in the perturbed system, the polarization vector of the dielectric medium can be expressed as follow:

$$\mathbf{P} = \mathbf{P}_{\mathbf{unperturbed}} + \mathbf{P}_{\mathbf{grating}} \tag{1.3}$$

where

$$\mathbf{P}_{\mathbf{unperturbed}} = \epsilon_0\chi^{(1)}\mathbf{E}_\mu \tag{1.4}$$

equation (1.2) becomes

$$\nabla^2\mathbf{E}_{\mu,\mathbf{t}} = \mu_0\epsilon_0\epsilon_r\frac{\partial^2}{\partial t^2}\mathbf{E}_{\mu,\mathbf{t}} + \mu_0\frac{\partial^2}{\partial t^2}\mathbf{P}_{\mathbf{grating},\mu} \tag{1.5}$$

The nature of the polarization of the perturbed medium, induced by the electric field that propagates across the grating, will be discussed later. By replacing the modal expansion of equation (1.1) in equation (1.5) we obtain:

$$\begin{aligned}
&\nabla^2\left[\frac{1}{2}\sum_{\mu=1}^{l}[A_\mu(z)\mathcal{E}_{\mu,t}e^{i(\omega t-\beta_\mu z)}+c.c.]+\sum\int_{\rho=0}^{\infty}A_\rho(z)\mathcal{E}_{\rho,t}e^{i(\omega t-\beta_\rho z)}d\rho\right]+\\
&+\frac{1}{2}\sum_{\mu=1}^{l}[A_\mu(z)\mathcal{E}_{\mu,t}e^{i(\omega t-\beta_\mu z)}+c.c.]+\\
&-\mu_0\epsilon_0\epsilon_r\frac{\partial^2}{\partial t^2}[\sum\int_{\rho=0}^{\infty}A_\rho(z)\mathcal{E}_{\rho,t}e^{i(\omega t-\beta_\rho z)}d\rho]=\\
&=\mu_0\frac{\partial^2}{\partial t^2}\mathbf{P}_{grating,\mu}
\end{aligned} \tag{1.6}$$

By neglecting the coupling with radiative modes

$$\begin{aligned}
&\nabla^2\left[\frac{1}{2}\sum_{\mu=1}^{l}[A_\mu(z)\mathcal{E}_{\mu,t}e^{i(\omega t-\beta_\mu z)}+c.c.]\right]+\\
&-\mu_0\epsilon_0\epsilon_r\frac{\partial^2}{\partial t^2}[\sum\int_{\rho=0}^{\infty}A_\rho(z)\mathcal{E}_{\rho,t}e^{i(\omega t-\beta_\rho z)}d\rho]=\\
&=\mu_0\frac{\partial^2}{\partial t^2}\mathbf{P}_{grating,\mu}
\end{aligned} \tag{1.7}$$

Now, it is need to develop the left term of the equation (1.7). Without the radiative contribution, the summations are only the modal expansion of the transversal field distribution $\mathbf{E}_t$, which sutisfy the unperturbed wave's equation:

$$\nabla_t^2\mathbf{E}_t-\mu_0\epsilon_0\epsilon_r\frac{\partial^2}{\partial t^2}\mathbf{E}_t=0 \tag{1.8}$$

Then, if we decompose the Laplacian operator in two contributions, transversal and longitudinal, as follow

$$\nabla^2=\nabla_t^2+\frac{\partial^2}{\partial z^2} \tag{1.9}$$

By replacing both the right term of equation (1.9) and equation (1.8) in (1.7), we obtain

$$\frac{\partial^2}{\partial z^2}\left[\frac{1}{2}\sum_{\mu=1}^{l}[A_\mu(z)\mathcal{E}_{\mu,t}e^{i(\omega t-\beta_\mu z)}+c.c.]\right]=\mu_0\frac{\partial^2}{\partial t^2}\mathbf{P}_{grating,\mu} \tag{1.10}$$

By deriving the product between the amplitude term $A_\mu(z)$ and the exponential,

$$\begin{aligned}
&\frac{\partial^2}{\partial z^2}\left[\frac{1}{2}\sum_{\mu=1}^{l}[A_\mu(z)\mathcal{E}_{\mu,t}e^{i(\omega t-\beta_\mu z)}+c.c.]\right]= \\
=&\frac{\partial}{\partial z}\left[\frac{1}{2}\sum_{\mu=1}^{l}[\frac{\partial A_\mu(z)}{\partial z}\mathcal{E}_{\mu,t}e^{i(\omega t-\beta_\mu z)}+c.c.]\right]+ \\
+&\frac{\partial}{\partial z}\left[\frac{1}{2}\sum_{\mu=1}^{l}(-i\beta_\mu)[A_\mu(z)\mathcal{E}_{\mu,t}e^{i(\omega t-\beta_\mu z)}+c.c.]\right]= \\
=&\frac{1}{2}\sum_{\mu=1}^{l}\left[\frac{\partial^2 A_\mu(z)}{\partial z^2}\mathcal{E}_{\mu,t}e^{i(\omega t-\beta_\mu z)}+c.c.\right]+ \\
+&\frac{1}{2}\sum_{\mu=1}^{l}(-i\beta_\mu)\left[\frac{\partial^2 A_\mu(z)}{\partial z^2}\mathcal{E}_{\mu,t}e^{i(\omega t-\beta_\mu z)}+c.c.\right]+ \\
+&\frac{1}{2}\sum_{\mu=1}^{l}(-i\beta_\mu)\left[\frac{\partial^2 A_\mu(z)}{\partial z^2}\mathcal{E}_{\mu,t}e^{i(\omega t-\beta_\mu z)}+c.c.\right]+ \\
+&\frac{1}{2}\sum_{\mu=1}^{l}(-\beta_\mu^2)[A_\mu(z)\mathcal{E}_{\mu,t}e^{i(\omega t-\beta_\mu z)}+c.c.]= \\
=&\frac{1}{2}\sum_{\mu=1}^{l}\left[\frac{\partial^2 A_m u(z)}{\partial z^2}\mathcal{E}_{\mu,t}e^{i(\omega t-\beta_\mu z)}+c.c.\right]+ \\
+&\frac{1}{2}\sum_{\mu=1}^{l}(-2i\beta_\mu)\left[\frac{\partial^2 A_m u(z)}{\partial z^2}\mathcal{E}_{\mu,t}e^{i(\omega t-\beta_\mu z)}+c.c.\right]+ \\
+&\frac{1}{2}\sum_{\mu=1}^{l}(-\beta_\mu^2)[A_\mu(z)\mathcal{E}_{\mu,t}e^{i(\omega t-\beta_\mu z)}+c.c.]
\end{aligned} \tag{1.11}$$

At this point, it is possible simplify the problem bu introducing the Slowly Varying Envelope Approximation (SVEA) in the hypothesis that the mode amplitudes slowly change as a function of the wavelenght [(4)]. From this point the dependence of $A_m u(z)$ from $z$ is omitted.

$$\frac{\partial^2 A_\mu}{\partial z^2} \ll \beta_\mu \frac{\partial A_\mu}{\partial z} \tag{1.12}$$

by applying the SVEA and grouping the terms in (1.11) we obtain

$$\nabla^2 \mathbf{E}_t = \frac{1}{2}\sum_{\mu=1}^{l}\left[-2i\beta_\mu \frac{\partial A_\mu}{\partial z}\mathcal{E}_{\mu,t}e^{i(\omega t-\beta_\mu z)} - \beta_\mu^2 A_\mu \mathcal{E}_{\mu,t}e^{i(\omega t-\beta_\mu z)} + c.c.\right] \tag{1.13}$$

Expanding the second term in equation (1.13), considering that $\omega^2\mu_0\epsilon_0\epsilon_r = \beta_\mu^2$ and by combining these with equation (1.13), the wave equation can be expressed as

$$\sum_{\mu=1}^{l}\left[-i\beta_\mu \frac{\partial A_\mu}{\partial z}\mathcal{E}_{\mu,t}e^{i(\omega t-\beta_\mu z)} + c.c.\right] = \mu_0 \frac{\partial^2}{\partial t^2}\mathbf{P}_{grating,t} \tag{1.14}$$

Here, the subscript $t$ associated to the polarization vector $\mathbf{P}_{grating,t}$ remembers us that the grating presents a transversal profile. By multiplying for $\mathcal{E}_\mu^*$ both the terms of equation (1.14) and integrating on the transverse section of the guide, we have:

$$\begin{aligned}\sum_{\mu=1}^{l}\int_{-\infty}^{+\infty}\int_{-\infty}^{+\infty}\left[-i\beta_\mu \frac{\partial A_\mu}{\partial z}\mathcal{E}_{\mu,t}\mathcal{E}_{\mu,t}^* e^{i(\omega t-\beta_\mu z)} + c.c.\right]dxdy = \\ = \int_{-\infty}^{+\infty}\int_{-\infty}^{+\infty}\mu_0 \frac{\partial^2}{\partial t^2}\mathbf{P}_{grating,t}\mathcal{E}_{\mu,t}^* dxdy\end{aligned} \tag{1.15}$$

Applying the following orthogonality relation

$$\begin{aligned}\frac{1}{2}\int_{-\infty}^{+\infty}\int_{-\infty}^{+\infty} e_z \cdot [\mathcal{E}_{\mu,t} \times \mathcal{E}_{\nu,t}^*]dxdy = \\ =\frac{1}{2}\left[\frac{\beta_\mu}{\omega\mu_0}\right]\int_{-\infty}^{+\infty}\int_{-\infty}^{+\infty}[\mathcal{E}_{\mu,t} \cdot \mathcal{E}_{\nu,t}^*]dxdy = \delta_{\mu\nu}\end{aligned} \tag{1.16}$$

Equation (1.15) becomes

$$\begin{aligned}\sum_{\mu=1}^{l}\left[-2i\omega\mu_0 \frac{\partial A_\mu}{\partial z}e^{i(\omega t-\beta_\mu z)} + c.c.\right] = \\ = \int_{-\infty}^{+\infty}\int_{-\infty}^{+\infty}\mu_0 \frac{\partial^2}{\partial t^2}\mathbf{P}_{grating,t}\mathcal{E}_{\mu,t}^*\end{aligned} \tag{1.17}$$

The last equation can be used to describe a large variety of mode coupling phenomena. Equation (1.17) is applied to progressive and regressive waves. It is intuitive to proof that there is mode coupling by introducing progressive and regressive modes: the transversal field can be described by a summation of both the modes, not necessarily of the same order. We obtain the following set of equation:

$$\mathbf{E}_t = \frac{1}{2}(A_\nu \mathcal{E}_{\nu,t} e^{i(\omega t - \beta_\nu z)} + c.c. + B_\mu \mathcal{E}_{\mu,t} e^{i(\omega t + \beta_\mu z)} + c.c.) \tag{1.18}$$

$$\mathbf{H}_t = \frac{1}{2}(A_\nu \mathcal{H}_{\nu,t} e^{i(\omega t - \beta_\nu z)} + c.c. - B_\mu \mathcal{H}_{\mu,t} e^{i(\omega t + \beta_\mu z)} - c.c.) \tag{1.19}$$

The negative sign of the exponent means a progressive mode, while the positive sign a regressive mode. These modes in an unperturbed waveguide form an orthogonal set than, but in the case of grating a mode coupling takes place. By replacing the equations (1.18) and (1.19) in equation (1.17) we obtain,

$$\begin{aligned} &\left[\frac{\partial A_\nu}{\partial z} e^{i(\omega t - \beta_\nu z)} + c.c.\right] - \left[\frac{\partial B_\mu}{\partial z} e^{i(\omega t + \beta_\mu z)} + c.c.\right] = \\ =&\frac{i}{2\omega} \int_{-\infty}^{+\infty} \int_{-\infty}^{+\infty} \frac{\partial^2}{\partial t^2} \mathbf{P}_{grating,t} \mathcal{E}^*_{\mu,\nu,t} dxdy \end{aligned} \tag{1.20}$$

As mentioned in [4- MANCA REFERENCE], this result plays an important role in the coupled mode theory.

### 1.1.2 Periodic spatial modulation of refrative index

In a material medium in which the dielectric constant $\epsilon$ changes periodically along the propagation direction, the total polarization can be defined by means of the perturbed permittivity, $\Delta\epsilon(z)$, in the following way:

$$\mathbf{P} = \epsilon_0[\epsilon_r - 1 + \Delta\epsilon(z)]\mathbf{E}_\mu \tag{1.21}$$

The terms included in the brackets are equivalent to $\chi^{(1)}$, and $\epsilon_r$ represents the permittivity of an unperturbed medium. In Physics, the relationship between the permittivity and refractive index $n$ of a material medium is expressed as $n^2 = \epsilon_r$, than we obtain

$$[n + \delta n(z)]^2 = \epsilon_r + \Delta\epsilon(z)] \tag{1.22}$$

$$n^2 + \delta n(z)^2 + 2n\delta n(z) = \epsilon_r + \Delta\epsilon(z)] \tag{1.23}$$

By assuming that the intensity of the perturbation $\delta n(z)$ is small with respect to the refractive index $n$

$$\Delta\epsilon(z) \approx 2n\delta n(z) \tag{1.24}$$

it is possible to define the refractive index modulation as

$$\delta n(z) = \overline{\Delta n} \left\{ 1 + \frac{\nu}{2}(e^{1[(2\pi N/\Lambda)z+\Phi(z)]} + c.c.) \right\} \tag{1.25}$$

where $\overline{\Delta n}$ is the average value of the refractive index variation in the fiber core, $\nu$ is the fringes visibility (a parameter of the fabrication process), while the argument of the exponential and the complex conjugate term describe the analytically the shape of the periodic modulation of the core index. $\Phi(z)$ is a generic phase term, $\Lambda$ is the modulation period while $N$ is an integer ($-\infty < N < +\infty$) that indicates the harmonic number. An important parameter of the fiber optic theory, the effective refractive index $n_{eff}$ is strictly dependent from $\overline{\Delta n}$ then, this value plays an important role in the design of a fiber grating. By considering the equations (1.22), (1.24) and (1.25) the final polarization of the medium becomes:

$$\mathbf{P} = \epsilon_0 \left\{ n^2 - 1 + 2n\overline{\Delta n} \left[ 1 + \frac{\nu}{2}(e^{1[(2\pi N/\Lambda)z+\Phi(z)]}) + c.c.) \right] \right\} \mathbf{E}_\mu \tag{1.26}$$

where, the first term at the second member is the permittivity, the second term is the continuous component of the refractive index variation, and the third term is the alternate component. To include the fringes visibility, it is possible to define a new quantity for the modulation intensity, defined as follow:

$$\delta n(z) = 2n \left[ \overline{\Delta n} + \frac{\Delta n}{2} (e^{1[(2\pi N/\Lambda)z+\Phi(z)]}) + c.c.) \right] \tag{1.27}$$

where $\Delta n = \nu \overline{\Delta n}$. Equation (1.27) describes the changes of the refractive index due to the UV writing of a grating in the fiber core. Now, the perturbed polarization can be releted to the refractive index perturbation given by equation (1.27). We have

$$\mathbf{P_{perturbed}} = 2n\epsilon_0 \left[ \overline{\Delta n} + \frac{\Delta n}{2} \left( e^{i[(2\pi N/\Delta)z+\Phi(z)]} + c.c. \right) \right] \mathbf{E}_\mu \tag{1.28}$$

At this point, by using the expression in (1.18) for $\mathbf{E}_\mu$ and by replacing $\mathbf{P_{perturbed}}$ with $\mathbf{P_{grating}}$ in equation (1.18), we obtain

$$\begin{aligned}
&\left[ \frac{\partial A_\nu}{\partial z} e^{i(\omega t - \beta_\nu z) + c.c.} \right] - \left[ \frac{\partial B_\mu}{\partial z} e^{i(\omega t + \beta_\mu z) + c.c.} \right] = \\
&= \frac{i\epsilon_0}{2\omega} \int_{-\infty}^{+\infty} \int_{-\infty}^{+\infty} \frac{\partial^2}{\partial t^2} \delta n(z) \left[ A_\nu e^{i(\omega t - \beta_\nu z)} \mathcal{E}_{\nu,t} + B_\mu e^{i(\omega t + \beta_\mu z)} \mathcal{E}_{\mu,t} \right] \mathcal{E}^*_{\mu,\nu,t} dxdy + c.c. = \\
&= - in\omega\epsilon_0 A_\nu \int_{-\infty}^{+\infty} \int_{-\infty}^{+\infty} \left[ \overline{\Delta n} + \frac{\Delta n}{2} \left( e^{i[(2\pi N/\Delta)z+\Phi(z)]} + c.c. \right) \right] \mathcal{E}_{\nu,t} e^{i(\omega t - \beta_\nu z)} \mathcal{E}^*_{\mu,\nu,t} dxdy + \\
&= - in\omega\epsilon_0 B_\mu \int_{-\infty}^{+\infty} \int_{-\infty}^{+\infty} \left[ \overline{\Delta n} + \frac{\Delta n}{2} \left( e^{i[(2\pi N/\Delta)z+\Phi(z)]} + c.c. \right) \right] \mathcal{E}_{\mu,t} e^{i(\omega t - \beta_\mu z)} \mathcal{E}^*_{\mu,\nu,t} dxdy + \\
&+ c.c.
\end{aligned} \tag{1.29}$$

In the LHS of equation (1.29), the variation rate of $A_\nu$ or $B_\mu$ is determined by the modal order $\mu$ or $\nu$ of the electric field $\mu, \nu, ^*$, chosen as multiplicative term in agree with the orthogonality relation (1.16). This is shown in (1.17) in the case of an electric that propagates in a single direction. Once the LHS is been chosen, it is necessary to choose the RHS. Before to perform the choice, it is useful to evaluate the terms of the RHS in its general formulation. The RHS expressed in equation (1.29) presents two generic components $A$ and $B$ for both the modes.

$$\begin{aligned} RHS =& in\omega\epsilon_0 B_\mu e^{i(\omega t+\beta_\mu z)} \int_{-\infty}^{+\infty}\int_{-\infty}^{+\infty} \overline{\Delta n}\mathcal{E}_{\mu,t}\mathcal{E}^*_{\mu,t}dxdy+ \\ & -in\omega\epsilon_0 A_\nu e^{i(\omega t+\beta_p z+\Phi(z))} \int_{-\infty}^{+\infty}\int_{-\infty}^{+\infty} \frac{\Delta n}{2}\mathcal{E}_{\nu,t}\mathcal{E}^*_{\mu,t}dxdy+ \\ & +c.c. \end{aligned} \tag{1.30}$$

where the argument of the first exponential must be the same of the field generated in the LHS of equation (1.29) which is dependent by the continuous component of the average refractive index variation $\overline{\Delta n}$. For effect of this formulation, each dependence phase-velocity do not remains in-phase with the generated wave. The second term in LHS is composed by two parts: the first depends by the phase-matching factor

$$\beta_p = \frac{2\pi N}{\Lambda} \pm \beta_\nu \tag{1.31}$$

Figure (1.1) shows the physical principle on which is based the phase matching: the radiating dipoles are distributed in the space with the period $\Lambda$, the polarization wave grows up but keeps in-phase with the field. The modal interaction that can take place, are determined by the RHS of equations (1.29) and (1.30). Must be considered two aspects: first, the conservation of angular momentum requires that the phase constants in the LHS and RHS of equation (1.30) must be equals, in this way they condition the mode coupling between propagative and counterpropagating modes; second, the transverse integral in RHS of equation (1.30), that represents the superposition of the refractive index modulation profile and the modal distribution of the fields, determines the strength of the modal interaction.

Figure (1.2) explains the meaning of the integral of equation (1.30) in the fiber optic case, the dotted lines state the core boundaries in which there two modes, the cross section of the fiber shows the fields of the modes $LP_{01}$ and $LP_{11}$, and the transverse profile of the refractive index modulation. The superposition of the two fields and the refractive index modulation profile, changes its sign from one half to the other half of the core, also the amplitude changes, then the integral is non-null. The transverse profile of the refractive index influences the symmetry of the modes whose coupling is allowed.

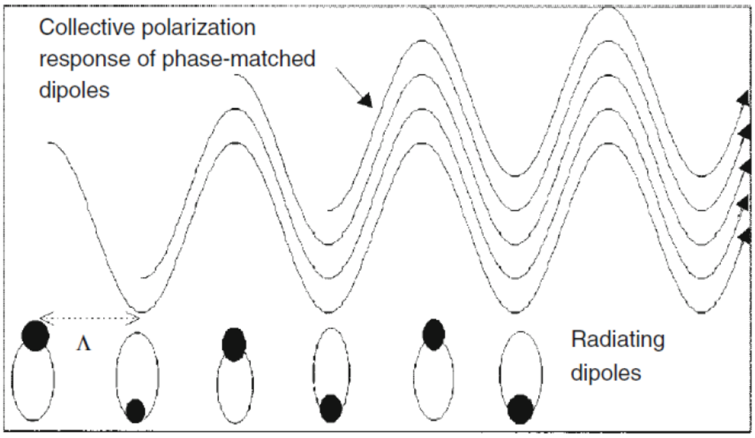

**Figure 1.1:** Phase-matching principle

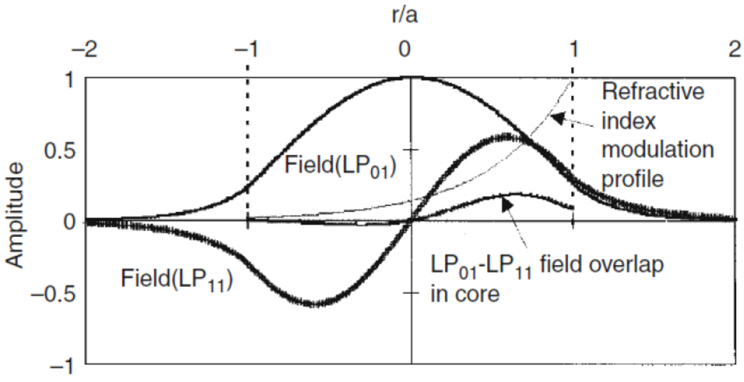

**Figure 1.2:** Superposition of modal distribution and refractive index modulation

### 1.1.3 Counter propagating modes coupling

The simplest manner of interaction takes place between a progressive mode and an identical regressive mode. To extend the treatise to a general case, we consider two different modes whose propagates in opposite directions. Equation (1.29) for this particular case becomes:

$$\begin{aligned}
&\frac{\partial B_\mu}{\partial z} e^{i(\omega t+\beta_\mu z)} + c.c. = \\
&\qquad = in\omega\epsilon_0\beta_\mu \int_{-\infty}^{+\infty}\int_{-\infty}^{+\infty} \overline{\Delta n}\mathcal{E}_{\mu,t}\mathcal{E}^*_{\mu,t} e^{i(\omega t+\beta_\mu z)} dxdy + \\
&\qquad + in\omega\epsilon_0 A_\nu \int_{-\infty}^{+\infty}\int_{-\infty}^{+\infty} \frac{\Delta n}{2} e^{i[(2\pi N/\Delta)z+\Phi(z)]}\mathcal{E}_{\nu,t}\mathcal{E}^*_{\mu,t} e^{i(\omega t-\beta_\nu z)} dxdy + \\
&\qquad + c.c.
\end{aligned} \tag{1.32}$$

By multiplying both the members with $e^{i(\omega t-\beta_\mu z)}$

$$\begin{aligned}
\frac{\partial B_\mu}{\partial z} &= in\omega\epsilon_0\beta_\mu \int_{-\infty}^{+\infty}\int_{-\infty}^{+\infty} \overline{\Delta n}\mathcal{E}_{\mu,t}\mathcal{E}^*_{\mu,t} dxdy + \\
&+ in\omega\epsilon_0 A_\nu \int_{-\infty}^{+\infty}\int_{-\infty}^{+\infty} \frac{\Delta n}{2} e^{i\{[(2\pi N/\Delta)-\beta_\nu-\beta_\mu]z+\Phi(z)\}}\mathcal{E}_{\nu,t}\mathcal{E}^*_{\mu,t} dxdy
\end{aligned} \tag{1.33}$$

that brings to the simple equation for the coupled modes

$$\frac{\partial B_\mu}{\partial z} = ik_{dc}\beta_\mu + ik_{ac}A - \nu e^{-i(\Delta\beta z-\Phi(z))} \tag{1.34}$$

where $\Delta\beta$ is defined as

$$\Delta\beta = \beta_\mu + \beta_\nu - \frac{2\pi N}{\Lambda} \tag{1.35}$$

$k_{dc}$ is the continuous coupling constant defined as

$$k_{dc} = n\omega\epsilon_0 \int_{-\infty}^{+\infty}\int_{-\infty}^{+\infty} \overline{\Delta n}\mathcal{E}_{\mu,t}\mathcal{E}^*_{\mu,t} dxdy \tag{1.36}$$

and $k_{ac}$ is the alternative coupling constant that includes the integral of superposition if $\mu = \nu$

$$k_{ac} = n\omega\epsilon_0 \int_{-\infty}^{+\infty} \int_{-\infty}^{+\infty} \frac{\Delta n}{2} \mathcal{E}_{\nu,t} \mathcal{E}_{\mu,t}^* dxdy = \frac{\nu}{2} k_{dc} \tag{1.37}$$

Also, the variation in amplitude of the forcing mode can be derived by the equation above by following the procedure in (1.29)

$$\frac{\partial|_\nu}{\partial z} = -ik_{dc}A_\nu - ik_{ac}^* B_\mu e^{-i(\Delta\beta z - \Phi(z))} \tag{1.38}$$

Finally, (1.34) and (1.38) are the equation of the mode coupling from whose it is possible to obtain the transfer characteristic of the Bragg grating. To solve the problem of the FBG, we operate the following substitutions, renaming the progressive mode as *Reference* and the regressive mode as *Signal*:

$$R = A_\nu e^{-(i/2)[\Delta\beta z - \Phi(z)]} \tag{1.39}$$

$$S = B_\mu e^{(i/2)[\Delta\beta z - \Phi(z)]} \tag{1.40}$$

By deriving the equations (1.39) and (1.40) with respect to $z$ and replacing in the equations (1.34) and (1.38) we obtain

$$\frac{dR}{dz} + i\left[k_{dc} + \frac{1}{2}\left(\Delta\beta - \frac{d\Phi(z)}{dz}\right)\right] R = -ik_{ac}^* S \tag{1.41}$$

$$\frac{dS}{dz} - i\left[k_{dc} + \frac{1}{2}\left(\Delta\beta - \frac{d\Phi(z)}{dz}\right)\right] S = ik_{ac}R \tag{1.42}$$

The Physical meaning of the terms included in the brackets is the following: $k_{dc}$ influences the propagation because of the average variation of the mode refractive index, as already discussed. Possible loss or gain can be included in the amplitude and sign of the imaginary component of $k_{dc}$. In the parenthesis, $\Delta\beta/2$ is the detuning factor which indicates the power exchange rate between the irradiated field and the polarization. In phase-matching condition, when $\Delta\beta = 0$, the field couples with the wave generated on an infinite distance. The term $\Phi$ represents the changing rate in the grating period and produces an effect similar to the detuning. For uniform gratings we have $\partial\Phi/\partial z = 0$, and for a fringes visibility $\nu = 1$ we obtain $k_{ac} = k_{dc}/2$.

The equations (1.41) and (1.42) can be solved by using classical techniques, under the hypothesis that the amplitude of the incident field at the starting point of the grating ($z = 0$) is $R(0) = 1$, and the field is $S(L) = 0$. The last condition is fulfilled as at the end of the grating the reflected field does not exist because of the absence of perturbation beyond the grating region. These conditions bring to the following analytic solution for the amplitude of the reflection coefficient of the grating:

$$\rho = \frac{S(0)}{R(0)} = \frac{-k_{ac}\sinh(\alpha L)}{\delta\sinh(\alpha L) - i\alpha\cosh(\alpha L)} \tag{1.43}$$

where

$$\delta = k_{dc} + \frac{1}{2}\left(\Delta\beta - \frac{d\Phi(z)}{dz}\right) \tag{1.44}$$

and

$$\alpha = \sqrt{|k_{ac}|^2 - \delta^2} \tag{1.45}$$

Notice that, for a uniform grating, in which the period variation $\Lambda$ is constant, the phase variation $d\Phi/dz = 0$. Moreover, in phase-matching condition $\Delta\beta = 0$ and the alternative coupling constant $k_{ac}$ is real. Finally, the reflection coefficient in power for a uniform fiber Bragg grating is:

$$|\rho|^2 = \frac{|k_{ac}|^2 \sinh^2(\alpha L)}{|k_{ac}|^2 \cosh^2(\alpha L) - \delta^2} \tag{1.46}$$

Depending by $\alpha$ in equation (1.45) is real or imaginary, can be defined the following regimes:

1 $\alpha$ is real when $|k_{ac}| > \delta$, are valid the equations (1.43) and (1.46);

2 $\alpha = 0$ when $|k_{ac}| = \delta$;

3 $\alpha = 0$ when $|k_{ac}| < \delta$, the equations (1.43) and (1.46) can be expressed as follow

$$\rho = \frac{-k_{ac} \sin(\alpha L)}{i\alpha \cos(\alpha L) - \delta \sin(\alpha L)} \tag{1.47}$$

$$|\rho|^2 = \frac{|k_{ac}|^2 \sin^2(\alpha L)}{\delta^2 - |k_{ac}|^2 \cos^2(\alpha L)} \tag{1.48}$$

### 1.1.4 Properties of Uniform gratings

The most common fiber Bragg gratings present a uniform refractive index modulation. Figure 1.3 shows the reflection spectra of two fiber Bragg grating in whose the coupling constant $k_{ac}L$ from equation (1.46) are equal to 2 and 8. It can be noticed that for the weaker grating ($k_{ac}L = 2$, dotted line) the bandwidth of the main lobe is more narrow than the stronger grating ($k_{ac}L = 8$, continuous line), morover the lateral lobes present a higher reflectivity in the case of strong gratings.

In a uniform grating, $d\Phi/dz = 0$ at the phase-matching wavelength, then the reflectivity

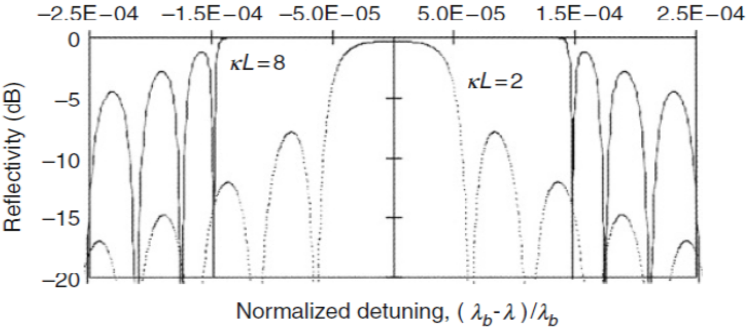

**Figure 1.3:** Reflectivity of two Bragg grating with coupling constants $k_{ac}L = 2, 8$, as a function of the normalized detuning.

can be expressed as

$$|\rho|^2 = \tanh^2(k_{ac}L) \tag{1.49}$$

The Bragg wavelength $\lambda_B$ is defined as the phase-matching wavelength. For two different modes that propagate in opposite direction, it is possible to obtain

$$\lambda_B = 2n_{eff}\Lambda \tag{1.50}$$

where $n_{eff}$ is the effective refractive index of the mode and $\Lambda$ is the grating period. In figure 1.4 is shown the schematic of the operating principle of a uniform fiber Bragg grating written in a single-mode fiber: under an incident broadband light source, only a very narrow portion of the source spectrum, centered in $\lambda_B$, is reflected by the grating, while in transmission there is all the source spectrum except for the reflected portion.

## 1.2 Fabrication of Fiber Bragg Gratings

The formation of permanent grating in optical fibers was first demonstrated by Hill et al. in 1978 [(5)]. They excited a germania-doped optical fiber with intense argon-ion

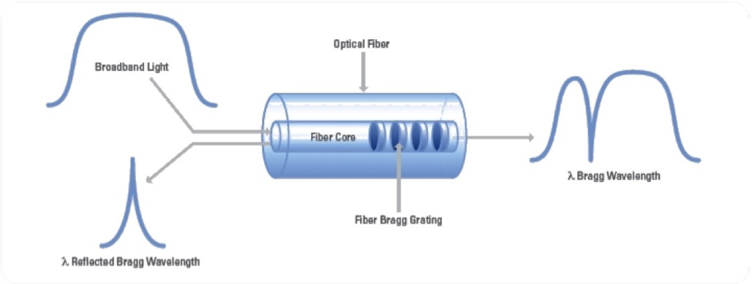

**Figure 1.4:** Schematics of the operative principle of a uniform fiber Bragg grating.

laser radiation at 488nm and observed that after several minutes the intensity of reflected light increased until eventually almost all the light was reflected from the fiber. The growth in back reflected light was explained in terms of non linear effect called photosensitivity, which permits the index of refraction in the core of the fiber to be increased by exposure to intense laser radiation. In this early experiment, a fiber Bragg grating was formed when a small amount of the laser light reflected back from the end of the optical fiber interferes with the exciting laser light to establish a standing wave pattern. Photosensitivity causes the index of refraction to be increased to a much greater extent at position where constructive interference results in a maximum of laser intensity. As the strength of the grating (proportional to the depth of its index modulations) increases the intensity of the back-reflected light increases until it saturates near 100%.

Although photosensitivity appeared to be an ideal means for fabricating these early Hill gratings in optical fibers, their usefulness was extremely limited because they only reflected at wavelengths in the visible close to the wavelength of the writing light, were spread along the optical fiber with varying strength and took a long time to produce. These limitations were overcome 10 years later by Meltz et al. in 1989 [(6)] who recognized from the work of Lam and Garside [(7)] that photosensitivity was a two photon-process that could be made more efficient if it were a one-photon process corresponding to the germania oxygen vacancy defect band, at a wavelength of 245nm (i.e. 5eV) [(8)]. In the experiment of Meltz (1989) the fiber was irradiated form the side with two intersecting coherent ultraviolet laser beams of wavelength 244nm (see figure 1.5), which corresponds to one half of the 488nm, the wavelength of the blue argon laser line.

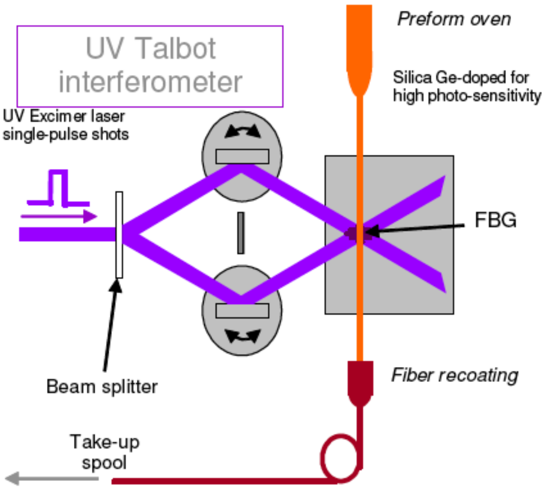

**Figure 1.5:** Schematics of interferometric configuration used by Meltz in 1989 (Source: IPHT Jena).

The transverse holographic method worked since fiber cladding is transparent to UV light, whereas fiber core is highly absorbing of this radiation. The principal advantage with regard grating fabrication is related to the fact that spatial period of photo-induced perturbation depends on intersecting angle between the two interfering beams. This permits a versatile and efficient fabrication of custom Bragg gratings operating at much longer wavelengths than the writing wavelength as shown in figure 1.6.

The periodic perturbation of the core index of refraction gives rise to successive coherent scattering for a narrowband band of the incident light. The grating thus effectively acts as a stop-band filter, reflecting light with wavelengths close to the Bragg wavelength, and transmitting wavelengths sufficiently different from resonance condition. Each reflection from a peak in the index perturbation is in phase with the reflection from the next peak when the wavelength of the light corresponds to the Bragg wavelength as shown in 1.4. Theoretical formulations based on coupled mode theory [(9)] have been developed to analyse fiber grating spectra by Erdogan et associates [(10)]. Successively, a variety of different continuous wave and pulsed lasers with wavelengths ranging from the visible to the vacuum UV have been used to write gratings in optical fiber.

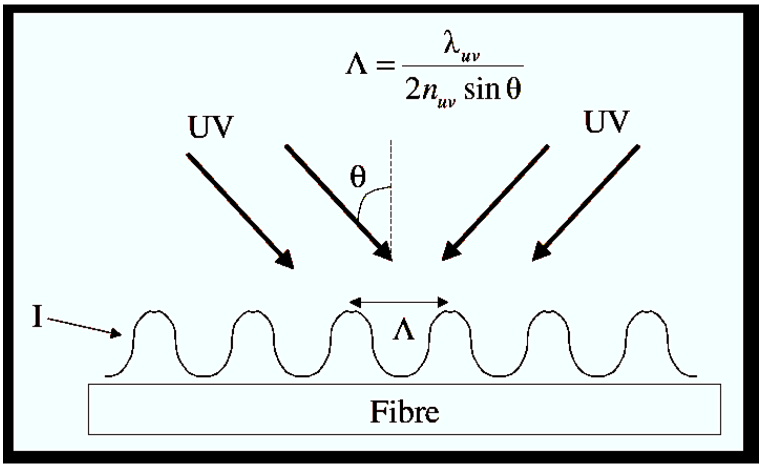

**Figure 1.6:** Grating period depends on intersecting angle between UV beams.

In practice, krypton-fluoride (KrF) and Argon fluoride (ArF) excimer lasers that generate (10 ns) pulses at wavelengths of 248 and 193nm, respectively, are used most frequently to produce FBGs.

The exposure required to produce a FBG is typically a few minutes with laser intensities of 100 to 1000 mJ/cm$^2$ and pulse rates of 50 to 75 s$^{-1}$. Under these conditions, the change in the core index of refraction is between $10^{-5}$ and $10^{-3}$ in germanium doped single-mode optical fiber. Techniques such as hydrogen loading proposed by Lemaire in 1993 can be used to enhance the optical fiber photosensitivity prior to laser irradiation [(11)]. Hydrogen diffusion makes the core more susceptible to UV laser radiation. Changes in refractive index of the order of $10^{-2}$ have been achieved by this means.

Successively, the transverse holographic method of writing fiber Bragg gratings has largely been superseded by the phase mask technique in 1993 [(12)]. Phase mask is a thin slab of silica glass into which is etched (using photolitographic techniques) a one-dimensional square wave periodic surface relief structure as shown in figure 1.7. Since this material is transparent to UV laser radiation the primary effect of the phase mask is to diffract the light into the 0, +1 and 1 diffraction orders.

Careful control of the depth of the corrugations in the phase mask suppresses zero-order diffraction, leaving the +/- 1 diffracted beams to interfere and produce the periodic pattern of intense laser radiation needed to photoimprint a Bragg grating in the core of

an optical fiber. If $\Lambda_{MASK}$ is the phase mask period, the photoimprinted index grating is $\Lambda_{MASK}/2$.
Note that grating period is independent of the writing radiation wavelength. Although, the usual practice brings the optical fiber almost into contact with phase mask, Othonos in 1995 demonstrated the improvements in the spatial coherence of the laser writing, relaxing the need for such close contact [(13)]. The phase mask technique greatly simplifies the manufacture of FBGs through easier alignment, reduced stability requirements on the photoimprinting apparatus, and lower coherence demands on the laser beam. It also permits the use of cheaper UV excimer laser source and tends to consistently yield high performance gratings.

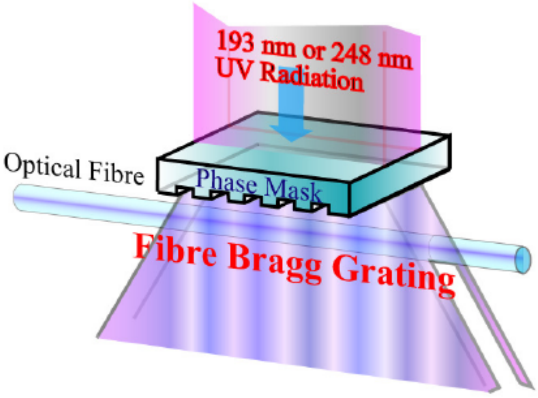

**Figure 1.7:** Diffracted UV beams from phase mask.

The prospect of manufacturing high performance gratings at low cost is critical to the large scale implementation of this technology for sensing applications. The main drawback associated to this approach relies to the need of separate phase mask for each grating with a different operating wavelength. On the other hand, it results very flexible since it can be used to fabricate gratings with controlled spectral responses characteristics. As a consequence of technological assessment, in the mid 1990s many research groups have been engaged in the study and realization of new grating devices through more complex refractive index modulation profiles. Examples include apodized FBGs, chirped FBGs, tilted FBGs, phase shift FBGs and long period fiber gratings

[(14, 15, 16, 17, 18, 19, 20)].

Although the theory and use of FBGs dates back to the late 80s, the commercial transition did not happen until the mid-1990s and was subsequently strongly driven by communications needs and the ramping up of the telecommunications bubble, which saw a tremendous explosion of the number of companies and research groups engaged with the design, fabrication, packaging and use of gratings.

First companies to produce commercial FBGs were 3M, Photonetics and Bragg Photonics in 1995. At the same time, Innovative Fibers was founded by Benoit Lavigne and Bernard Malo in 1995 and was a leader in the design and manufacture of FBG based components for the fiber optics industry including gain flattening filters, 50GHz and 100GHz DWDM filters and 980nm and 1480nm pump laser stabilizers. Successively, in 1997, Ciena Corp a manufacturer of WDM devices became the largest public start-up company in corporate history and with first year earnings of $\sim$ \$ 200 million had the fastest revenue track ever.

Soon after the telecommunications bubble collapse, there was a significant shift by many players in the industry from communications to sensing applications. At the time, this was a prudent and strategic move on the part of FBG manufacturers to keep exploiting the technical and manufacturing infrastructure they had available and ride the telecomm crisis until a possible comeback. Nevertheless, the sensing sector benefited tremendously from this shift and resulted in an increase in activity and demand of FBG-based sensors.

As FBGs made the transition, from optical communications devices to sensing elements in the 1990s, the bulk of the sensing applications centered on discrete, single-point sensing of specific parameterssuch as strain and temperatureusing sensors based on embedded or packaged gratings.

These early gratings were typically written using phase masks or side exposure interferometric techniques. These fabrication methods initially relied heavily on manual skills and labor, severely limiting many of the features and performance of the gratings in terms of production capacity, repeatability, mechanical strength, as well as number and quantity of FBGs written on a continuous fiber. Furthermore, during the boom years of the telecommunication industry in the late 1990s, it was possible to absorb the cost of the low yield from such manufacturing.

Due to this increasing interest in FBG sensing technology, many research studies were devoted to the conception of optoelectronic unit able to demodulate FBGs based sensors. As matter of fact, the first optoelectronic unit able to interrogate FBGs sensors was developed 1996 by ElectroPhotonics corporate solutions and was based on the edge filtering concept [(21, 22)]. However, the sensor industry is much more cost sensitive, demanding multiple sensing points and greater mechanical strength. Such requirements also call for the capability to fabricate an array of multiple FBGs at different locations along a same length of optical fiber. Such needs are being addressed by more sophisticated, on-line, reel-to-reel fabrication processes and systems that allow the writing of complex FBG arrays along a continuous single fiber spool.

## 1.3 The Fiber Bragg Grating as sensor

As described in the previous section and with reference to figure 1.4, the fiber optic intracore grating relies on the narrowband reflection from a region of periodic variation in the core index of refraction of a single mode optical fiber [(23)]. The central wavelength of the reflected Bragg signal is generally called Bragg wavelength and is linearly dependent upon the product of the effective index of refraction of the fundamental mode and the grating period: $\lambda_B = 2n_{eff}\Lambda$. This means that changes in strain or temperature to which the optical fiber is subjected linearly shift the Bragg wavelength leading to a wavelength encoded measurements that is self referencing [(24, 25)]. In particular, the effective refractive index $n_{eff}$ is an intrinsic physical characteristic of the material in which the grating is formed; the grating period $\Lambda$ depends on its design. It is evident that, changes of these quantities produce changes in the Bragg wavelength $\lambda_B$. Changes in temperature or a strain applied on the fiber grating modify directly the effective refractive index or the grating period, respectively. These are the principles that have allowed to take advantage of the FBG as sensor. Furthermore, intrinsic wavelength encoding also provides a convenient and simple method for serial sensor multiplexing (see figure 1.8) [(21)].

The present FBG sensor market is primarily composed of 3 key segments: 1) sensing devices, 2) instrumentation, and 3) system integration & installation services [(26)]. The sensing devices segment is composed of bare FBGs for sensing applications, packaged FBG sensors and FBG arrays. The instrumentation market segment is composed of FBG interrogating instruments and related ancillary components such as multiplexors, switches, data acquisition systems, software and graphical user interfaces. Finally, the third segment is mostly covering services and entails all project management and engineering aspects related to implementing sensing solutions and system installations such as design, planning, system integration, customer training, service and on-site installation.

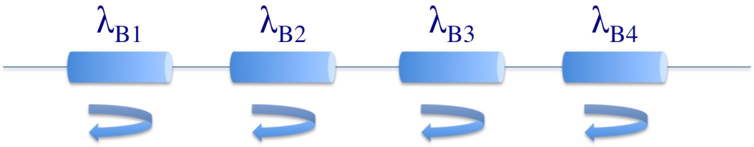

**Figure 1.8:** Multi-point (quasi-distributed) sensing system based on FBGs.

### 1.3.1 Sensing principles for temperature and strain

A change in temperature or strain, acts directly on the Bragg wavelength giving its shifts left or right according to the intensity and the sign of the change. By measuring the Bragg wavelength variation $\Delta\lambda_B$ it is possible to determine the variation in temperature or strain applied to the grating.

A simple equation is used to describe the thermo-mechanical sensing principle of the FBG:

$$\frac{\Delta\lambda_B}{\lambda_B} = G_\epsilon \Delta\epsilon + S_T \Delta T \tag{1.51}$$

where, $\Delta\epsilon = \epsilon - \epsilon_0$ and $\Delta T = T - T_0$ represents the change in strain and temperature with respect to initial reference values ($\epsilon_0$ and $T_0$) and $\Delta\lambda_B/\lambda_B$ is the normalized Bragg wavelength shift for a FBG sensor, $G_\epsilon$ and $S_T$ are the strain factor and the thermal sensitivity, respectively. The parameters $G_\epsilon$ and $S_T$ can be considered constant on a wide range of values [(1)]. Also, the (1.51) can be expressed in the following manner:

$$\frac{\Delta\lambda_B}{\lambda_B} = (1 - p_\epsilon)\Delta\epsilon + (\alpha_\Lambda + \alpha_n)\Delta T \qquad (1.52)$$

where $p_\epsilon$ is the elasto-optic coefficient, $\alpha_\Lambda$ is the coefficient of thermal expansion (CTE) and $\alpha_n$ is the thermo-optic coefficient of the fiber core.

Since each measure of strain is inevitably affected by changes in temperature, in most applications it is necessary to measure the temperature and compensate it. In doing so, the effects of thermal expansion and the influence of the temperature on the index of refraction may be taken into account and can be determined by the effective strain. In the temperature range from -20 °C to 80 °C the thermal sensitivity of a Bragg grating is $S_T \approx 10 \times 10^{-6}$ °C$^{-1}$, in a simpler way if means that for temperature change $\Delta T = 1$ °C, we will observe a Bragg wavelength shift $\Delta\lambda_B = 10$ pm.

The strain sensitivity of a FBG is $G_\epsilon \approx 0.80$. To to better understand this value must be considered only the strain term of equation (1.51):

$$\Delta\lambda_B = \lambda_B G_\epsilon \Delta\epsilon \qquad (1.53)$$

If the Bragg wavelength was fixed (e.g.: 1550 nm), $G_\epsilon = 0.78$, and for a strain of $\Delta\epsilon = 1000\mu\epsilon$ there would be a Bragg wavelength shift of $\Delta\lambda_B = 1.21$ nm.

### 1.3.2 Sourrounding Refractive Index (SRI) sensing principle

In a fiber grating, the Bragg wavelength $\lambda_B$ depends only on the grating period $\Lambda$ and the effective refractive index $n_{eff}$ of the propagative mode. In a standard single-mode optical fiber, the effective refractive index is not affected by the refractive index of the surrounding medium. Consequently, the FBG is insensitive to the Surrounding Refractive Index (SRI) [(27, 28)]. If the fiber cladding diameter on the grating region is properly thinned, the $n_{eff}$ is significantly affected by the SRI: a Bragg wavelength shift and a changes in the reflectivity are observed, due to changes in the propagation characteristics of the mode. Unlike the most common uses of FBG (temperature and strain sensing), in the SRI sensing only the $n_{eff}$ is affected by the measurand (SRI).

## 1.4 FBG read-out techniques and sensor multiplexing

Today several companies are active in the development of efficient FBG demodulator systems. These could be classified into three main groups: 1) passive detection schemes based on pass band edge detection systems using fixed filters; 2) active detection schemes including tunable filters and interferometric systems; and 3) other schemes such as wavelength tunable sources and laser frequency modulation [(21)]. With regard to multiplexing capability, commercial interrogators fall into two main categories: time division multiplexing (TDM) and wavelength division multiplexing (WDM) [(29)]. TDM (see figure 1.9) discriminates between many sensors on a single optical fiber by gauging the time required for a pulse of light to return to the detection system. In TDM, all sensors are nominally written at the same wavelength exhibiting low reflectivity. Blue Road Inc. has successfully developed FBG interrogators based on such idea. However, the most popular approach is WDM.

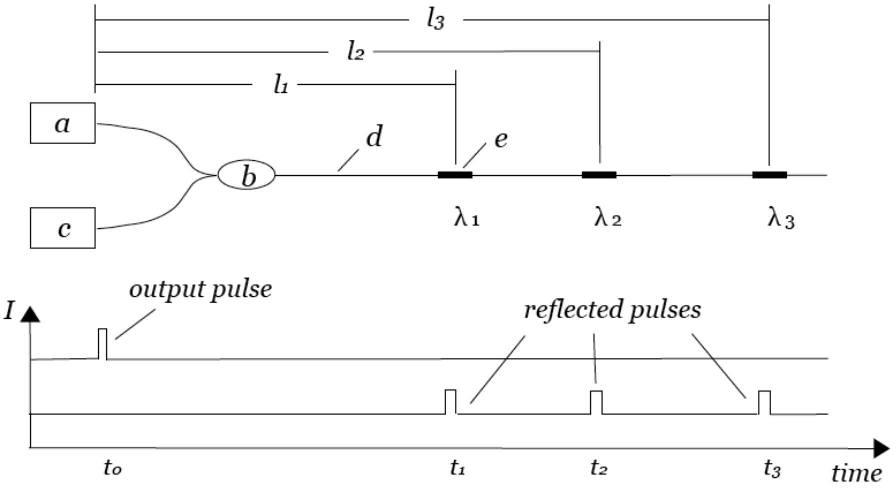

**Figure 1.9:** Schematics of Time Division Multiplexing (TDM). a) light source; b) optical coupler; c) detector; d) optical fibers; e) FBGs.

WDM (see figure 1.10) systems discriminate individual sensors by wavelength. Most WDM read-out systems are designed using one of two basic configurations: broadband source and swept detector and laser source and broadband detector. In the former approach, usually, few tens of sensors on a single fiber can be investigated whereas

laser-based interrogators can illuminate more than 100 sensors per channel.
For instance, Micron Optics Inc. has developed such kind of interrogators. In fact they propose wavelength scanning systems with sub-picometer peak wavelength resolution, broad-spectrum (80 nm) capability, but with a relatively slow-scan, data acquisition rate typically from 1 Hz to 250 Hz up to 512 sensors on four fibers. Also, Micron Optics Inc. offers the si920 high-speed optical sensing interrogator capable of monitoring FBG sensors up to four simultaneous channels with acquisition rates as fast as 500 kHz on a single channel or 100 kHz on four parallel channels. It is built with a patented architecture, using parallel fiber Fabry-Perot tunable filters.
Alternative wavelength scanning systems are available such as the FiberPro2 from Luna Innovations (Roanoke, Va.), operating at data sampling rates of 1 kHz; the HS-FOIS produced by AEDP (Lanham, Md.) with data rates of up to 3.5 kHz; the I*Sense systems produced by IFOS (Santa Clara, Calif.) with data rates of up to 5 kHz; and the FBG read-out systems from Blue Road Research (Gresham, Oreg.) with data rates of up to 2 MHz. Further commercial systems offering from 1 to 16 input channels are available.

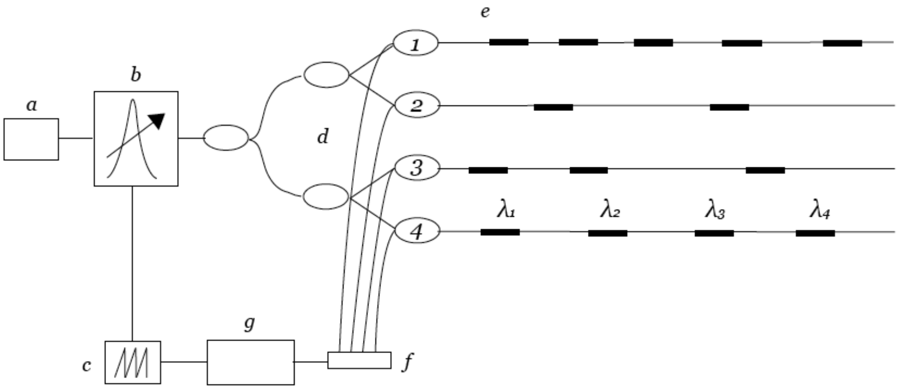

**Figure 1.10:** Schematics of Wavelength Division Multiplexing (WDM). a) light source; b) scanning filter; c) scanning generator; d) optical coupler; e) FBG arrays; f) photodetector; g) processor.

In 2008, Micron Optics, Inc. has announced an enhancement in available dynamic Optical Sensing Interrogator, in terms of increase in scanning range to over 160 nm which means more sensors per channel; up to 640 sensors on four fibers [(30)]. Finally its important to note that, in May 2007 HBM [(31)] (the worlds largest supplier of strain sensing systems) began offering optical strain gages and interrogators based on FBG technology.

Also, to favorite a wide spread out of FBG sensors, the development of appropriate packages was demanded. In particular, there was a need to develop appropriate protective coatings and housings for fiber sensors; to investigate the fundamental transfer of strains, stresses, pressure and temperature from the host specimen or matrix to the sensing fiber and the associated materials inter-play; as well as the development of field installation processes and deployment techniques suitable for different applications and environments [(32)].

On the bases of the FBG principle, a large number of solutions based on it have been proposed in the last decades, for strain, temperature, acoustic waves, ultrasound measurements as well as pressure and magnetic fields [(24, 25)]. FBG-based sensors have been proposed, designed and developed for a wide variety of mechanical sensing applications including monitoring of civil structures, smart manufacturing and non-destructive testing, remote sensing, underwater applications, transportation, High Energy Physics experiment sites.

The present worldwide volume demand for bare and packaged FBG sensors is estimated to be greater than 10,000 pieces per year. The worldwide volume demand for FBG arrays is estimated at several 100s to 1,000s arrays per year. The combined present global market size of this segment is estimated to be in the range of \$ 15M to \$ 35M USD a year, with an annual growth rate of 15% to 25%. The instrumentation market has been growing steadily over the past three years, in part due to a variety of new fiber sensing projects and installations throughout Asia. Furthermore, the global volume for FBG interrogating instruments is estimated at several hundred units a year, with an annual growth rate of 20% to 30%.

The total market size is estimated to be in excess of \$ 50M USD. In following sections the most relevant FBG industrial applications achieved in last years are reported.

## 1.5 Sensing applications of FBGs

Among the reasons why optical fibers are such an attractive are their low loss, high bandwidth, EMI immunity, small size, lightweight, safety, relatively low cost, low maintenance, etc. As optical fibers cemented their position in the telecommunications industry and its technology and commercial markets matured, parallel efforts were carried out by a number of different groups around the world to exploit some of the key fiber features and utilize them in sensing applications [(33, 34)]. Initially, fiber sensors were lab curiosities and simple proof-of-concept demonstrations.

### 1.5.1 Industrial applications

More and more, optical fibers are making an impact and serious commercial inroads in other fields besides communications such as in industrial sensing, biomedical laser delivery systems, military gyro sensors, as well as automotive lighting & control (to name just a few) and spanned applications as diverse as oil well downhole pressure sensors to intra-aortic catheters. This transition has taken the better part of 20 years and reached the point where fiber sensors enjoy increased acceptance as well as a widespread use for structural sensing and monitoring applications in civil engineering, aerospace, marine, oil & gas, composites, smart structures, bio-medical devices, electric power industry and many others [(21, 35, 36, 37)]. Optical fiber sensor operation and instrumentation have become well understood and developed. And a variety of commercial discrete sensors based on Fabry-Perot (FP) cavities and fiber Bragg gratings (FBGs), as well as distributed sensors based on Raman and Brillouin scattering methods, are readily available along with pertinent interrogation instruments. Among all of these, FBG based sensors have become widely known, researched and popular within and out the photonics community and seen a rise in their utilization and commercial growth.

### 1.5.2 High Energy Physics applications

Nuclear radiation effects on optical materials and photonic devices have been studied since several decades. In the early days one of the main concerns was to determine whether advanced technologies could withstand military and tactical environments such as surveillance satellite missions and nuclear weapon explosions. Today many other applications associated with presence of highly energetic radiation can benefit from the enhanced functionalities offered by photonic technologies for communication and sensing. Examples of these application fields include space, healthcare, civil nuclear industry and high energy physics experiments. Future thermonuclear fusion plasma reactors will also rely on optical communication and sensing techniques.

Electronic and photonic components are well known to suffer from exposure to nuclear radiation [(38, 39, 40, 41, 42)]. The radiation interacts with the materials and alters their characteristics. This most often modifies the performance and affects the reliability of the device. Resulting device failures and system malfunctions may have dramatic consequences on safety and carry significant financial repercussions. One has to bear in mind that human intervention to replace components or to repair systems in radiation environments is mostly impossible due to the radioactivity levels involved or for reasons of accessibility. It is indeed almost impossible to repair onboard equipment once a satellite has been put into orbit. One can hence understand the importance of carefully investigating how radiation affects the operation and the reliability of photonic components intended for use in these harsh environments and of ensuring that devices and systems will survive the entire mission.

Several years ago optical fibers carried a relatively bad reputation in terms of resistance to ionizing radiation. The fibers were indeed known to darken rapidly during exposure with substantial levels of so called radiation induced attenuation (RIA) as a result. Modern fiber fabrication technologies now allow obtaining fibers with low to moderate levels of RIA, depending on the wavelength range. This together with the undeniable and well-known advantages of fiber optic technology and the increased availability of compact, efficient and lower cost devices promoted renewed interest in the applications of optical fiber based systems in radiation environments.

A fiber Bragg grating (FBG) is a typical example of a versatile photonic component that can be applied in both optical communication and sensing systems. FBGs are for example being considered as sensor elements for structural health monitoring of spacecrafts and as dosimeter in nuclear facilities. Both types of applications put entirely different demands on the FBGs: for the first application the gratings should be insensitive to radiation whereas for the second they should essentially be as sensitive as possible.

The radiation hardness is one of the key features required to a monitoring system operating in an environment in which High-Energy Physics (HEP) experiments are performed. Such operative condition are considered *standard condition* at CERN (European Organization for Nuclear Research) laboratories (in Geneva, Switzerland). [(43)]

The CERN is the largest laboratory in the word for the HEP studies. From 2008 is active at the CERN the most powerful particle accelerator: LHC (Large Hadron Collider), which in these days has obtained the word record of the produced power: equal to 7 TeV. Compact Muon Solenoid Experiment (CMS) [(44)] is one of the most important experiments active at the CERN, which is designed to found the Higgss boson.

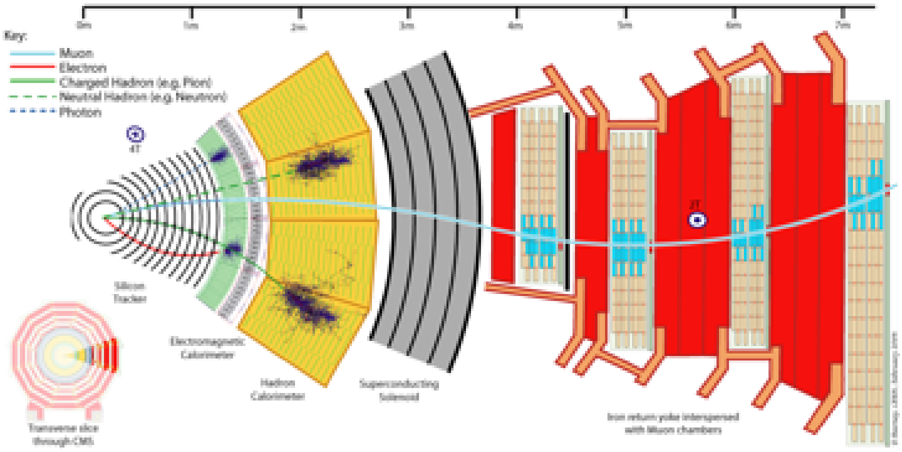

**Figure 1.11:** CMS detector transverse slice. From the left, Pixel, silicon Tracker, Electromagnetic calorimeter (ECAL), hadron calorimeter (HCAL), superconducting solenoid, iron return yoke with moun chambers..

CMS Experiment is a very complex and large detector made of a large superconductive magnetic solenoid (which is able to produce a magnetic field up to 4T) and several particles sub-detectors: the Tracker is the more sensitive part of CMS, it can reconstruct the paths of the high-energy muons, electrons and hadrons (particles made up of quarks) as well as see tracks coming from the decay of very short-lived particles such as beauty or b quarks that will be used to study the differences between matter and antimatter. Photons and electrons, particularly interesting because of their use in finding the Higgs boson and other new physics, are measured using an Electromagnetic Calorimeter (ECAL). The Hadron Calorimeter (HCAL) measures the energy of hadrons, particles made of quarks and gluons (for example protons, neutrons, pions and kaons). Because muons can penetrate several meters of iron without interacting, unlike most particles they are not stopped by any of CMS's calorimeters. Therefore, chambers to detect muons are placed at the very edge of the experiment where they are the only particles likely to register a signal. A particle is measured by fitting a curve to hits among the four muon stations, which sit outside the magnet coil and are interleaved with iron "return yoke" plates (shown in red below, for the barrel region). The CMS experiment is 21 m long, 15 m wide and 15 m high, and sits in a cavern. It is divided into sections: the main body (barrel) is composed of five wheels, while the ends (endcap) are composed of three wheels. As described in the schematic shown in figure 1.11, detectors consist of layers of material that exploit the different properties of particles to catch and measure the energy and momentum of each one. Being unstable the operating conditions of CMS, for its proper functioning it is required a constant monitoring of temperature, structural deformation, relative humidity, and magnetic field especially in the silicon Tracker characterized by having the higher sensitivity. For example, when LHC is activated, the attraction force produced by the strong magnetic field (4-5 Tesla), acts on the Tracker and may deforms the scaffold that sustains the accelerator pipe causing severe damaging to the whole experiment.

Nuclear radiation effects on optical materials and photonic devices have been studied since several decades [(45, 46, 47)]. Ionizing radiation produces wavelength-dependent radiation-induced attenuation in optical fibers [(48, 49, 50)]. Being spectrally encoded, the Fiber Bragg Grating (FBG) sensors [(51, 52, 53)] are insensitive to noise, intensity modulation of the optical carrier and broadband-radiation-induced losses, this permits to realize with them reliable sensors for various HEP applications and extended distance monitoring systems [(54)].

# Chapter 2

# Long-term temperature monitoring at CMS

## 2.1 Introduction

As discussed in the previous chapter, FBG sensor is a suitable device to measure temperature in the room range [from - 20 °C to 80 °C]. In this range, the thermal sensitivity of a Bragg grating has a linear behavior, this encourage the use of this technology to realize temperature sensing system due to a low calibration complexity.

Moreover, in harsh environments such as CERN or generic Nuclear Plants, due to the high level of ionizing radiation, the classical electronic sensor are practically unreliable. Nowadays, all the CMS area is under constant monitoring by using thousands of thermo-resistance sensors (PT100). The main scope of these is having information about of the working condition of some subsystems. The monitoring became crucial for all the equipments that are temperature dependent and/or have to work under particular thermal conditions. Obviously, each PT100 requires two wires to be connected to a single channel of a proper acquisition system. This means that cabling issues have to be addressed when the sensors number increases as the case of CMS experiment where the large amount of electrical sensors is used.

The already high number of detectors and electrical wiring installed at the CMS, does not permit further installation of temperature monitoring systems. Moreover, during the operation of LHC, the level of radiation and magnetic field is too high to allow a good functioning of conventional electronic sensing devices. Radiation immunity represents the most important specification required to a monitoring system operating in such environment; other needs are: low complexity layout, multiplexing and multiparameters measurement capabilities.

Actually, the FBG represents the ideal candidate to be employed as sensor with a high rate of reliability and accuracy, in such environments. In this chapter, the design and the development of a long-term temperature measurement system for CMS experiment site is presented [(55)].

## 2.2 Conventional monitoring systems for HEP Applications: RTD

Nowadays, the monitoring systems used to retrieve temperature measurements from the CMS cavern are based on classical electronic devices. The temperature monitoring is needed to ensure the correct operative condition within the CMS cavern to make safe the impressive and expensive infrastructures and, obviously, the working condition of technicians and scientists.

The actuals temperature monitoring systems are equipped by resistance temperature detectors (RTDs) as sensing elements, used to measure temperature by correlating the resistance of the RTD element with temperature. Most RTD elements consist of a length of fine coiled wire wrapped around a ceramic or glass core. The element is usually quite fragile, so it is often placed inside a sheathed probe to protect it. The RTD element is made from a pure material, platinum, nickel or copper. The material has a predictable change in resistance as the temperature changes; it is this predictable change that is used to determine temperature. They are slowly replacing the use of thermocouples in many industrial applications below 600 °C, due to higher accuracy and repeatability.

Common RTD sensing elements constructed of platinum, copper or nickel have a unique, and repeatable and predictable resistance versus temperature relationship (R vs T) and operating temperature range. The R vs T relationship is defined as the amount of resistance change of the sensor per degree of temperature change. The relative change in resistance (temperature coefficient of resistance) varies only slightly over the useful range of the sensor. Platinum is a noble metal and has the most stable resistance-temperature relationship over the largest temperature range. Nickel elements have a limited temperature range because the amount of change in resistance per degree of change in temperature becomes very non-linear at temperatures over 300 °C. Copper has a very linear resistance-temperature relationship, however copper oxidizes at moderate temperatures and cannot be used over 150 °C. Platinum is the best metal for RTDs because it follows a very linear resistance-temperature relationship and it follows the R vs T relationship in a highly repeatable manner over a wide temperature range. The unique properties of platinum make it the material of choice for temperature standards over the range of -272.5 °C to 961.78 °C, and is used in the sensors that define the International Temperature Standard, ITS-90. Platinum is chosen also because of its chemical inertness. The significant characteristic of metals used as resistive elements is the linear approximation of the resistance versus temperature relationship between 0 °C and 100 °C. This temperature coefficient of resistance is called alpha, $\alpha$. The equation 2.1 defines $\alpha$; its units are ohm/ohm/°C.

$$\alpha = \frac{R_{100} - R_0}{100 \cdot R_0} \tag{2.1}$$

where, $R_0$ is the resistance of the sensor at 0 °C and $R_{100}$ is the resistance of the sensor at 100 °C. Pure platinum has an alpha of 0.003925 ohm/ohm/°C and is used in the construction of laboratory grade RTDs. Conversely two widely recognized standards for industrial RTDs IEC 60751 and ASTM E-1137 specify an alpha of 0.00385 ohms/ohm/°C. Before these standards were widely adopted several different alpha values were used. It is still possible to find older probes that are made with platinum that have alpha values of 0.003916 ohms/ohm/°C and 0.003902 ohms/ohm/°C. These different alpha values for platinum are achieved by doping; basically carefully introducing impurities into the platinum. The impurities introduced during doping become embedded in the lattice structure of the platinum and result in a different R vs. T curve and hence alpha value.

### 2.2.1 Function

Resistance thermometers are constructed in a number of forms and offer greater stability, accuracy and repeatability. Resistance thermometers use electrical resistance and require a power source to operate. The resistance ideally varies linearly with temperature. The platinum detecting wire needs to be kept free of contamination to remain stable. A platinum wire or film is supported on a former in such a way that it gets minimal differential expansion or other strains from its former, yet is reasonably resistant to vibration. RTD assemblies made from iron or copper are also used in some applications. Commercial platinum grades are produced which exhibit a temperature coefficient of resistance 0.00385/°C (0.385%/°C) (European Fundamental Interval). The sensor is usually made to have a resistance of 100 $\Omega$ at 0 C.

Measurement of resistance requires a small current to be passed through the device under test. This can cause resistive heating, causing significant loss of accuracy if manufacturers limits are not respected, or the design does not properly consider the heat path. Mechanical strain on the resistance thermometer can also cause inaccuracy. Lead wire resistance can also be a factor; adopting three- and four-wire, instead of two-wire, connections can eliminate connection lead resistance effects from measurements; three-wire connection is sufficient for most purposes and almost universal industrial practice. Four-wire connections are used for the most precise applications.

### 2.2.2 Limitations

The most common advantages of RTD include:

- High accuracy;
- Low drift;
- Wide operating range;
- Suitability for precision applications.

**Limitations**

RTDs in industrial applications are rarely used above 660 °C. At temperatures above 660 °C it becomes increasingly difficult to prevent the platinum from becoming contaminated by impurities from the metal sheath of the thermometer. This is why laboratory standard thermometers replace the metal sheath with a glass construction. At very low temperatures, say below -270 °C (or 3 K), because there are very few phonons, the resistance of an RTD is mainly determined by impurities and boundary scattering and thus basically independent of temperature. As a result, the sensitivity of the RTD is essentially zero and therefore not useful.

**Sources of error**

The common error sources of a RTD are:

- Interchangeability: the closeness of agreement between the specific RTD Resistance vs. Temperature relationship and a predefined Resistance vs. Temperature relationship;
- Insulation Resistance: Error caused by the inability to measure the actual resistance of element. Current leaks into or out of the circuit through the sheath, between the element leads, or the elements.
- Stability: Ability to maintain R vs T over time as a result of thermal exposure.
- Repeatability: Ability to maintain R vs T under the same conditions after experiencing thermal cycling throughout a specified temperature range.
- Hysteresis: Change in the characteristics of the materials from which the RTD is built due to exposures to varying temperatures.
- Stem Conduction: Error that results from the RTD sheath conducting heat into or out of the process.
- Calibration/Interpolation: Errors that occur due to calibration uncertainty at the cal points, or between cal point due to propagation of uncertainty or curve fit errors.
- Lead Wire: Errors that occur because a 4 wire or 3 wire measurement is not used, this is greatly increased by higher gauge wire. 2 wire connection adds lead resistance in series with RTD element. 3 wire connection relies on all 3 leads having equal resistance.
- Self Heating: Error produced by the heating of the RTD element due to the power applied.
- Time Response: Errors are produced during temperature transients because the RTD cannot respond to changes fast enough.

- Thermal EMF: Thermal EMF errors are produced by the EMF adding to or subtracting from the applied sensing voltage, primarily in DC systems.

Moreover, as discussed in the section above, these devices are unable to furnish reliable measurements during the LHC/CMS operation because they suffer ionizing radiation. Due to the excessive error sources, the RTD sensors do not seem to be the most suitable to use in environments with harsh operating conditions such as the CMS.

## 2.3 Optical temperature sensing system for CMS

The advantages of small size, light weight, electromagnetic immunity [(56)], radiation hardness [(57)],[(58)], etc, make FBG sensors the ideal devices for a large variety of applications [(59)] and, in particular, for HEP experiments.

The general aspects of the fiber optic sensors technology based on FBGs have been widely demonstrated during the last decade [(54)]. These sensors are characterized by a reflected wavelength defined as the Bragg wavelength $\lambda_B$. Quasi-distributed sensing systems based on FBGs can be easily realized by using a Wavelength-Division Multiplexing (WDM) approach [(**?** )] and it permits to use FBG arrays to arrange a simple sensing system with a high number of sensing points per channel distributed along a wide area.

The limitation on the realization of FBG arrays are imposed by the bandwidth of acquisition system that, together with the spectral minimum spacing between sensors, puts a constraint on the maximum number of sensors can be integrated on a single channel. A limitation on the arrays length is set by the optical power loss intrinsic of the fiber (about 0.3 dB/km), bends, junctions, etc. The extremely low loss level permits to realize multi-point sensing systems distributed in a large area. The conventional sensing system with broadband source is limited to 25 km due to Rayleigh scattering [(53)].

### 2.3.1 FBG temperature sensor for HEP environment

The FBG sensor arrays were manufactured by Welltech Inc. on the basis of a standard single-mode optical fiber SMF-28. They are characterized by a temperature range goes from -20 °C to 150 °C, a resolution of 0.1 °C and an accuracy of 1 °C. The sensors are packaged with a ceramic material to mitigate radiation hardness issues and their dimension are 40x10x5mm. Figure 2.1 shows the commercial packaged sensors used in this experiment.

**Figure 2.1:** FBG sensor packaged with a ceramic material.

### 2.3.2 Multiplexing of FBGs

The spectral features of the FBG sensors allow to realize efficient spatially-distributed sensing systems on a single fiber by using the Wavelength Division Multiplexing (WDM) technique together with a spectrally-encoded readout technique based on tunable laser source and broadband detection bench [(60)].

This technique consists in interrogating a certain number of grating at the same time exploiting the spectral diversity between their selves: since a FBG reflects only a narrow portion of the incident light, by putting several gratings in series on the same fiber, the instrument will read a reflection spectrum that is composed by the central wavelengths of each grating.

To determine the minimum spectral spacing between each FBG sensor, it is necessary to take into account the spectral range of variation of the central wavelength of the grating that is affected by the temperature range of the CMS. Table (2.1) shows the central wavelength of each FBG used and the temperature to which it is referred. The wavelength spacing between two spectrally contiguous sensors was chosen in order to

**Table 2.1:** Wavelength Division Multiplexing

| | Fiber no. 1 | | Fiber no. 2 | |
|---|---|---|---|---|
| **Sensor** | **$\lambda_{\mathrm{B}}$ (nm)** | **T [°C]** | **$\lambda_B$ (nm)** | **T [°C]** |
| 1 | 1528.114 | 29.8 | 1528.054 | 29.8 |
| 2 | 1530.965 | 29.8 | 1531.092 | 29.8 |
| 3 | 1534.029 | 29.8 | 1534.165 | 29.8 |
| 4 | 1536.842 | 29.8 | 1536.782 | 29.8 |
| 5 | 1539.757 | 29.8 | 1540.201 | 29.8 |
| 6 | 1546.037 | 29.8 | 1546.360 | 29.8 |
| 7 | 1549.215 | 29.8 | 1549.089 | 29.8 |
| 8 | 1551.937 | 29.8 | 1551.718 | 29.8 |
| 9 | 1555.162 | 29.8 | 1554.990 | 29.8 |
| 10 | 1557.746 | 29.8 | 1557.770 | 29.8 |

guarantee a correct peak detection. We spliced 10 FBGs per fiber. The distance between each adjacent sensor is approximately 2m. The junctions FBG-SMF28 have been made using a fusion splicer that minimizes the power loss induced from the junctions by implementing an auto-alignment facility of the fiber cores.

### 2.3.3 Interrogation unit

A Micron Optics SM 125-500 optical interrogator has been used [(61)]. The most relevant features of this instrument are reported in Table 2.2 [(62)]. The read-out system cyclically carries out a scanning in wavelength and detects each peak upper to a certain threshold. From the resulting dynamic spectrum is possible to determine the spectral changes of the FBGs with respect of the time. A crucial parameter for a proper WDM integration is the wavelength range of the interrogator. Our instrument provides a band of 80 nm that is widely adequate for the respect of the limitation imposed by the WDM. In figure 2.2 the reflected spectrum of fiber no. 1 is shown. The 10 peaks represent the Bragg wavelength of the sensors. This is a good example of WDM in practical applications.

**Table 2.2:** Optical Properties of Micron Optics SM125-500 Optical Interrogator

| Parameter | Value |
|---|---|
| Number of channels | 4 (up to 16) |
| Scan frequency | 2 Hz |
| Wavelength range | 1510 - 1590 nm |
| Wavelength accuracy | 1 pm |
| Wavelength stability | 1 pm |
| Wavelength repeatability | 0.5 pm at 1 Hz/0.2 pm at 0.1 Hz |
| Dynamic range | 50 dB |

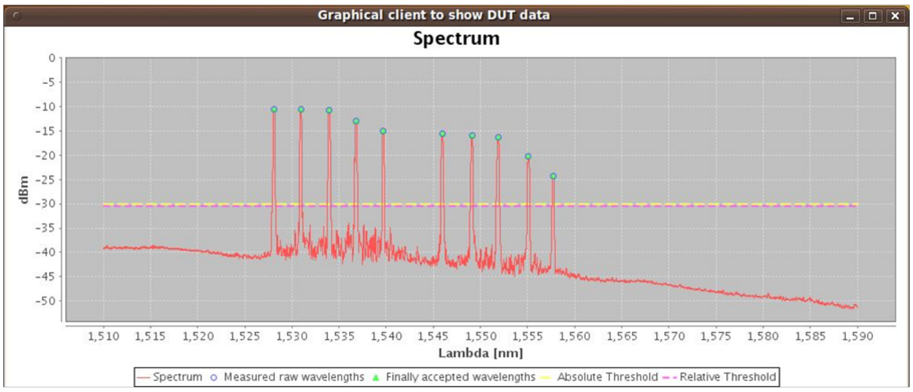

**Figure 2.2:** Correspondence scheme between FBG sensors and PT100 placed on the BulhHead sides Z- (left) and Z+ (right).

### 2.3.4 Calibration

To obtain temperature measurements from the optoelectronic system is necessary a post-processing of the outcoming data, the Bragg wavelength shifts have to be converted in temperature by means of a calibration function determined by a calibration procedure. In the ambient temperature range of CMS, the thermal sensitivity curve of the FBG sensor has a linear behavior then the calibration procedure, carried out

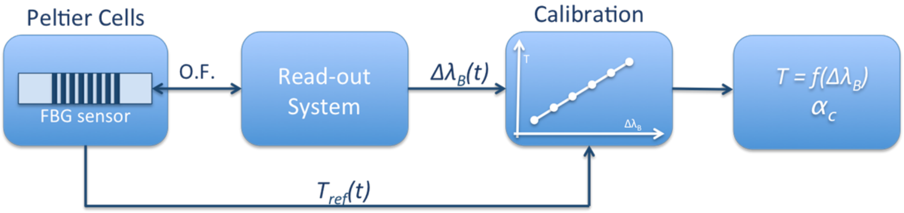

**Figure 2.3:** Schematic of FBG sensor calibration procedure.

by measuring the lambda shift in the temperature range from 20 °C to 150 °C, with a temperature step of 10 °C, has given the first order function: $T_{FBG}(t) = \alpha_c \Delta\lambda_B(t)$, where $T_{FBG}(t)$ is the temperature calculated from the Bragg wavelength shift of the FBG and $\alpha_c$ is the calibration coefficient that is given by the slope of the thermal sensitivity curve. Figure 2.3 shown a schematic of the calibration procedure.

Table 2.3 contains the calibration coefficients calculated from the calibration procedure which were used for the temperature reconstruction.

**Table 2.3:** Calibration coefficient

| | Fiber no. 1 | Fiber no. 2 |
|---|---|---|
| **Sensor** | $\alpha_{\mathbf{c}}$ | $\alpha_c$ |
| 1 | 97.000 | 97.087 |
| 2 | 97.087 | 97.087 |
| 3 | 95.238 | 97.087 |
| 4 | 96.154 | 95.238 |
| 5 | 95.238 | 96.154 |
| 6 | 96.154 | 96.154 |
| 7 | 95.238 | 94.340 |
| 8 | 95.238 | 95.238 |
| 9 | 94.340 | 95.238 |
| 10 | 96.154 | 95.238 |

### 2.3.5 Sensors positioning

The sensor positioning is a crucial part of the experiment in which the technician must have to select the best place to install the sensor to minimize the distance between the optical sensors and the point in which perform the measurement. The aim of this experiment is to provide the temperature monitoring on the *pixel sensors* of CMS. The CMS tracker is made entirely of silicon: the pixels, at the very core of the detector and dealing with the highest intensity of particles, and the silicon microstrip detectors that surround it. As particles travel through the tracker the pixels and microstrips produce tiny electric signals that are amplified and detected. The tracker employs sensors covering an area the size of a tennis court, with 75 million separate electronic read-out channels: in the pixel detector there are some 6000 connections per square centimeter. The CMS silicon tracker consists of 13 layers in the central region and 14 layers in the endcaps. The innermost three layers (up to 11 cm radius) consist of 100 × 150 $\mu$m pixels, 66 million in total. The next four layers (up to 55 cm radius) consist of 10 cm × 180 $\mu$m silicon strips, followed by the remaining six layers of 25 cm × 180 $\mu$m strips, out to a radius of 1.1 m. There are 9.6 million strip channels in total.

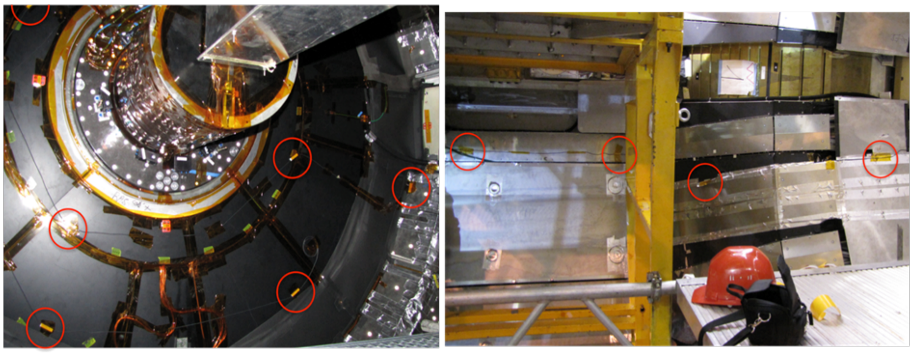

**Figure 2.4:** Pictures of CMS end-flange surface and Tracker cable tray where 10 FBG sensors were installed as temperature sensors. 6 sensors were installed on the bulkhead surface.

Two arrays have been installed on the disk which separates the endcap to the barrel where are located pixel sensors, and along the power line. In figure 2.4, the sensors installed on the BulkHead Z+ side and on the cable tray are shown. The red circles evidence some of the installed sensors. To validate the performance of our optoelectronic monitoring system, it was necessary to associate a PT100 sensor to each FBG. Figure 2.5 reports the correspondence map between FBG and PT100 installed onto the two sides of the Tracker. Each FBG sensor is identified by a acronym pBH or nBH, indicating respectively its position on the positive or negative side of the BulkHead, followed by its serial number that goes from 1 to 10 for each side while, each PT100 reference sensor is identified by the suffix "Trk" followed by its serial number.

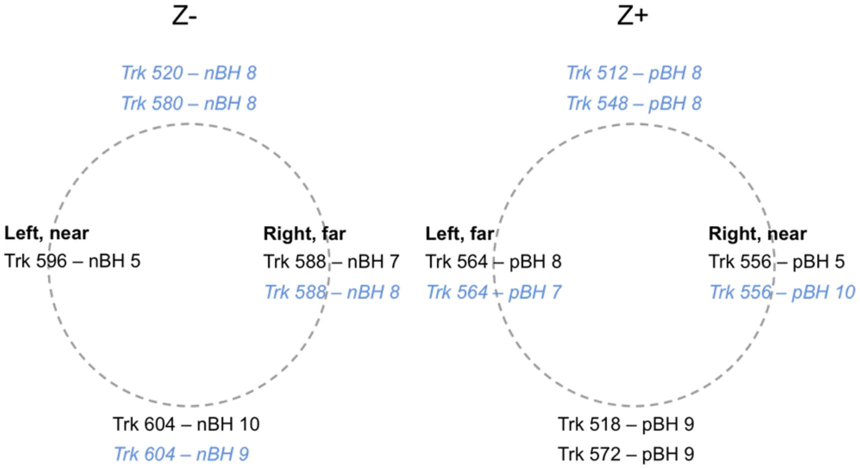

**Figure 2.5:** Schematic of the FBG array installed on the Z+ side: the array was placed at the interface disk barrel-endcap, 6 sensors per array were placed onto the disk and four were placed along the power line that provides electric power to the barrel section.

### 2.3.6 Acquisition System and Data Processing

Optical fibers installed on the BulkHead of the CMS Tracker are then directed to the Underground Service Cavern (USC). USC is a member of the twin caverns of the CMS experiment and is isolated by means of radiation hazards from the experimental one that houses the detector itself. Being radiation safe, this cavern is accessible during the LHC operations as well. The optical fibers are read out by a MO sm125 optical interrogator system that is equipped with an Ethernet interface and can be accessed through a proprietary TCP/IP protocol.

In order to reduce network traffic on the interrogator, it is connected to a mini private network created by the readout computer. This computer has another network interface installed as well, that allows the integration and sharing of the FOS system data with the CMS Detector Control System [(63)]. In order to provide the operating system independence, the read out software is written in Java language by our group. This software communicates with the sm125 interrogator: downloads peak definition parameters and reads out both the peak information and the spectrum of each optical fiber. In order to be able to be integrated into the CMS Detector Control System (DCS), the read out software uses the DIM protocol [(64)] that is a custom protocol over TCP/IP developed at CERN. DCS system of the CMS detector is implemented in the widely used PVSS [(65)] process management software language using the CERN built JCOPS framework [(66)]. In PVSS we also developed a module that connects to the read out software via DIM and then provides the quasi-standard interface required by the experiment. This module besides the relaying commands to the FOS system is responsible for the archiving the recorded data into the CMS online Oracle database. This module is heavily used by the Sensors for CMS (S4CMS) project that collects and visualizes data from various subsystems to allow better understanding of the behavior of the CMS detector. Furthermore, the read out software is also able to dump the raw data into text files to allow offline analysis.

## 2.4 Results and Discussion

This section reports some experimental results collected during all the testing period. The measurement period is almost a full year: it is enough to make an accurate evaluation of the system performance. Figure 2.6 and 2.7 show the temperature measured by FOS during the operation of the BulkHead subsystems Z+. From these two figures it is possible to observe that the system is highly reliable and presents a good measurement stability. The temperature deviation is due to the different sensors location.
Figure 2.8 shows the comparisons between FOS and PT100 temperature measurements..The PT100 data are deadbanded. This causes their sparse appearence and the rapid turns in figure 2.8.

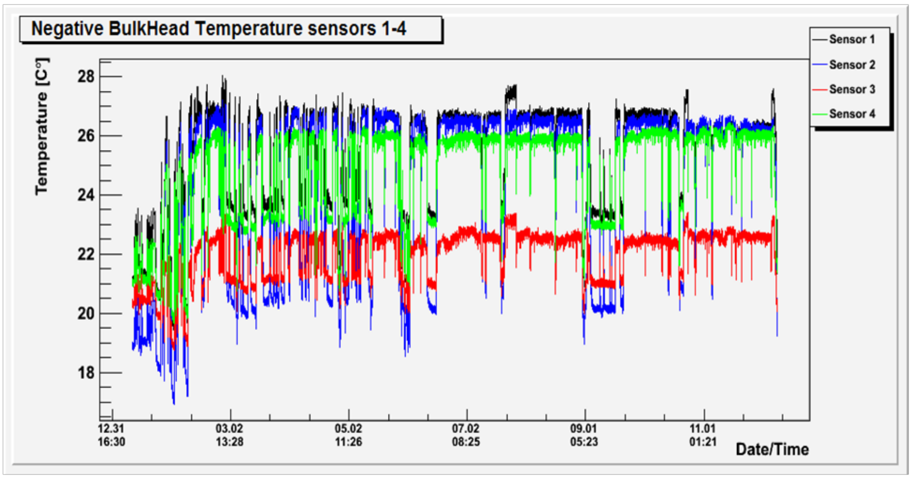

**Figure 2.6:** Temperature data of FBG sensors 1-4 on the cable tray +Z side.

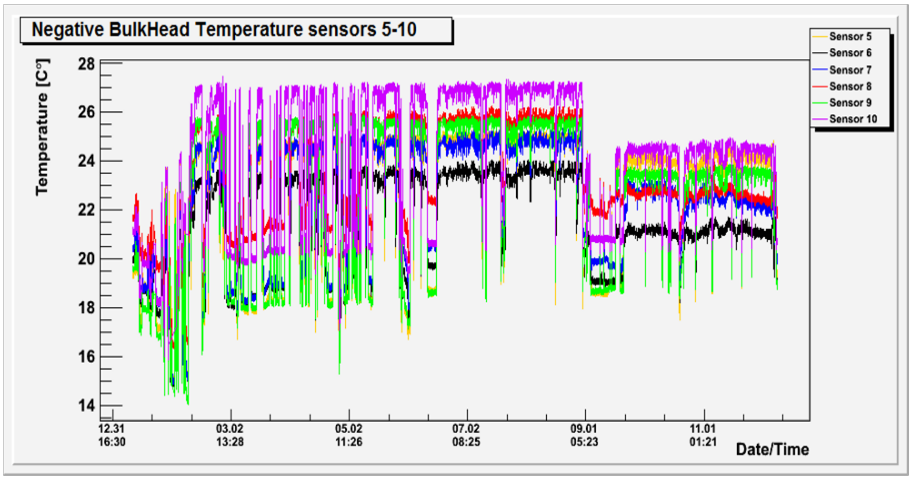

**Figure 2.7:** Temperature data of FBG sensors 5-10 on the BulkHead +Z side.

Moreover, the PT100 and the FBG sensors are placed on the opposite sides of the BulkHead heat shield and their alignments were not very exact (see figure 2.2). For the performance comparison plot we have chosen the ones closest to each other, but these differences cause the slight differences in data. Figure 2.9 shows the temperature correlation between the FOS measurements and the PT100. Each dot shows the correspondent PT100 measurement to each FOS temperature.

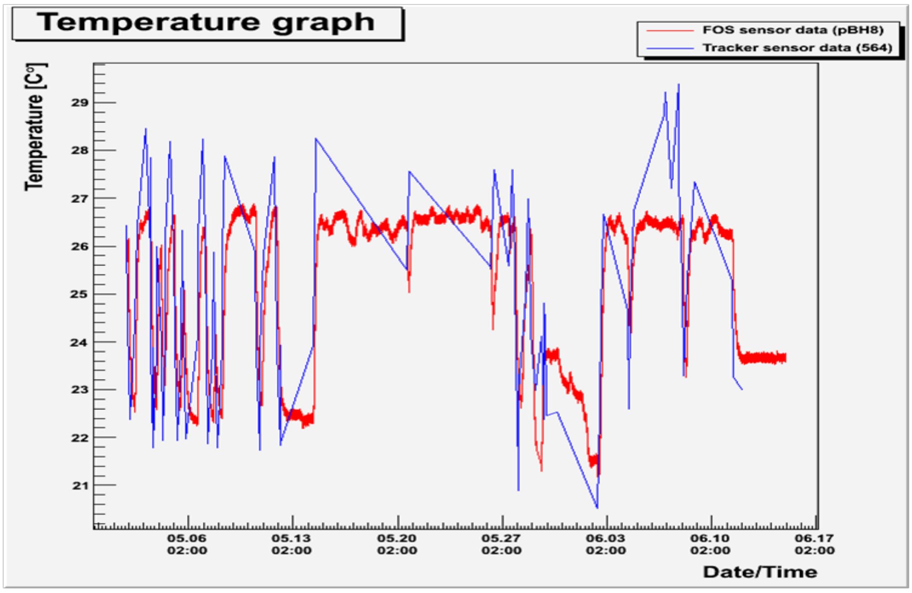

**Figure 2.8:** Performance comparison between FBG sensor (pBH8) and Tracker sensor. The picture shows a good agreement between the two sensing technology.

The overall trend is linear as can be seen, but horizontal lines can also be seen, if many FOS data might get the same PT100. This is due to the deadbanding used on the PT100 data in order to reduce the load on the CMS online database. In order to demonstrate the goodness of the data pairing, it is useful to observe the time-control plot of the pairing shown in figure 2.10: the time of the individual PT100 measurements are shown for those of all FOS measurements. Since they don't deviate from the linear line slope = 1, we can be sure that the pairing always found the valid PT100 and FOS data together.

By taking into account these practical criticalities, from the results obtained during the full year of CMS operation, the FOS monitoring system have shown excellent performance in terms of reliability and agreement to the PT100 sensors.

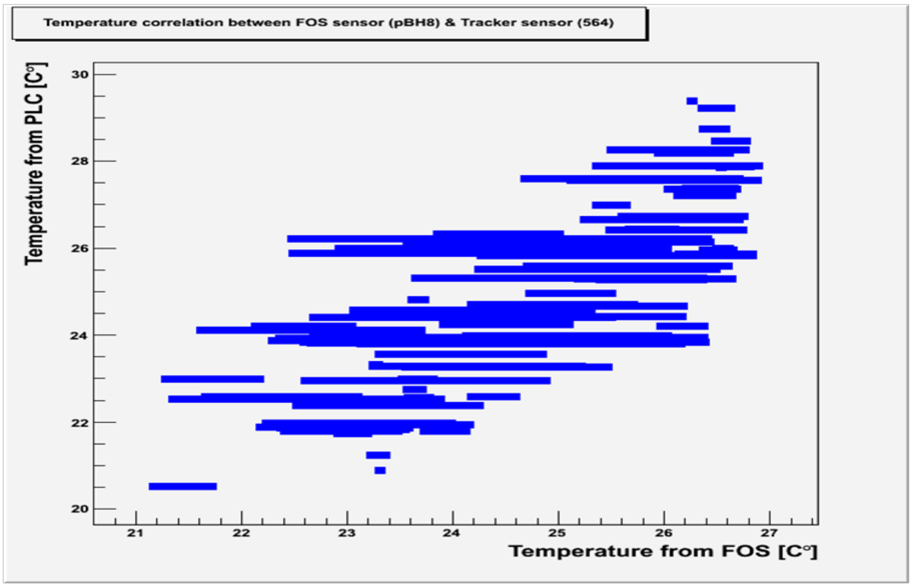

**Figure 2.9:** Temperature correlation between FOS sensor (pBH8) and Tracker sensor (564): it is possible to note the linear trend that confirm the linearity of the FOS measurements.

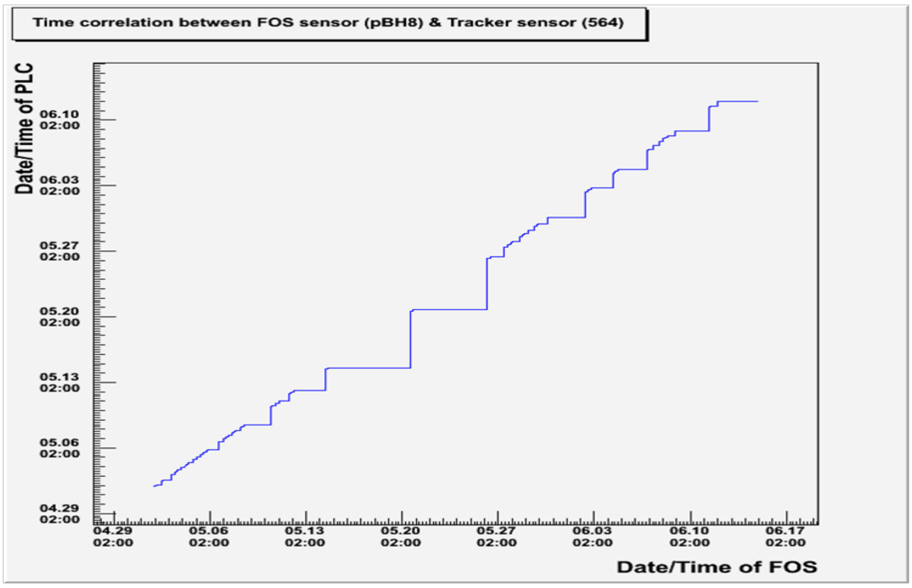

**Figure 2.10:** Time correlation between FOS sensor (pBH8) and Tracker sensor (564): the behavior dont deviate from the linear line slope = 1.

## 2.5 Conclusions

The results obtained have shown a good reliability of the monitoring system during 1 year of operation at CMS. Moreover they have shown a good agreement between FBG sensors and Tracker sensors measurements.

A temperature monitoring system based on FBG sensors has been installed and successfully tested in the very hard environmental conditions of the CMS experiment site. In this work, for the first time we demonstrated the long-term reliability of a temperature monitoring system based on FBG sensors operating in an environment with high levels of ionizing radiation and strong magnetic fields. After more than a year, the sensing system works properly and provides important information about the temperature in the critical areas of the CMS experiment that are very difficult to cover with traditional electronic sensors. During the early part of 2012, an extension of the above discussed system, composed by 60 FBG sensors assembled in 2 arrays (30 + 30 FBGs), has been successful installed to furnish a temperature monitoring on all the areas of CMS experiment.

## Chapter 3

# FBG cryogenic temperature sensor for HEP applications

## 3.1 Introduction

At the CERN experiment sites, one of the most critical issue of monitoring, regards cryogenic temperature sensing under ionizing radiation and high electromagnetic fields. The Large Hadron Collider (LHC) has to use powerful electromagnets to keep its high-energy particles on a circular track. To provide the strong fields needed to grip its high-energy particles, the LHC electromagnets exploit the phenomenon of superconductivity, in which an electric current passes almost without resistance. In this way, the LHC magnets can be powered to very high fields and at minimal cost. Most materials which become superconducting only do so at liquid helium temperatures. As well as being vitally dependent on temperature, superconductivity also depends on other factors. If the current is increased beyond a critical level, the material ceases to be superconducting. This critical current itself depends on temperature as well as on the applied magnetic field. To maintain the required high currents and avoid such problems, the liquid helium bathing the LHC's electromagnets will be cooled down to just 1.9 K, at which temperature helium is a superfluid. Providing cryogenics on this scale calls for some very special technology, providing efficient refrigeration capacity and long-distance transport of this capacity at very low temperatures. The LHC represents a major fraction of the world cryogenic effort, not only in sheer volume but also for research and development work. To maintain its 27-kilometre ring at superfluid helium temperatures, the LHC's cryogenic system will have to supply an unprecedented total refrigeration capacity of some 150 kW at 4.5 K and 20 kW at 1.9 K distributed around the ring. About half of the refrigeration capacity used at the LHC was originally installed for LEP - CERN's electron-positron collider. There its job was to provide the liquid helium supply for the superconducting radiofrequency cavities which boosted the energy of the particle beams. For the LHC, this cryogenic supply had to be doubled in size to provide much more liquid helium, and extended to cool helium from 4.5 K down to 1.9 K using several stages of centrifugal compressors.

The LHC will be installed deep underground in a quasi-circular tunnel, composed of eight 3.3-km long sectors with access shafts to technical service areas at ground level only at the ends of each sector. As a result, the cryogenic layout of the machine features five cryogenic islands concentrating all refrigeration and ancillary equipment, both at ground level (electrical substation, compressor hall, cryogen storage, cooling towers, 4.5 K coldboxes) and underground (lower coldboxes, 1.8 K refrigeration units, interconnecting lines, distribution valve boxes). Each cryogenic island therefore feeds one or two adjacent sectors, via a compound cryogenic distribution line [(67)] distributing and recovering the cooling fluids over a distance of 3.3 km.

The staging of temperature levels in the LHC cryogenic system generates the following loads:

- thermal shielding between 50 K and 75 K as primary heat intercept in all cryostats and transfer lines;
- non-isothermal cooling of the beam screens by supercritical helium between 4.6 K and 20 K, to absorb beam-induced loads (synchrotron radiation, beam image currents, electron cloud) before they reach the 1.9 K level
- quasi-isothermal cooling of the magnet cold mass in superfluid helium below 1.9 K;
- isothermal cooling of stand-alone magnets, acceleration cavities and the lower section of HTS current leads in saturated helium at 4.7 K;
- non-isothermal cooling of the resistive upper section of current leads by forced flow of gaseous helium between 20 K and 290 K.

Most of these loads exhibit static and dynamic components. While the former are produced by heat inleaks and therefore depend on thermal insulation, the latter - both steady-state and transient - result from the powering of the magnets and the circulation of high-energy, high-intensity beams [(68)]. As an example, the heat load on the 1.9 K level will increase in the ratio 3:1 over a period of half an hour, upon current ramping of the magnets and beam acceleration to 7 TeV. Although partially buffered by the heat capacity of the superfuid helium bath, such a variation in demand requires load adaptation of the refrigerators over a large dynamic range. Taking into account these loads, and applying factors for uncertainty of 1.25 on static loads and 1.5 overall, yields the specified installed refrigeration capacity in the LHC sectors (3.1).

**Table 3.1:** Installed refrigeration capacity in the LHC sectors

| **Temperature** | 50-75 K [W] | 4.6-20 K [W] | 4.7 K [W] | 1.9 K [W] | 3-4 K [W] | 20-280 K [g/s] |
|---|---|---|---|---|---|---|
| High-load sector | 33000 | 7700 | 300 | 2400 | 430 | 41 |
| Low-load sector | 31000 | 7600 | 150 | 2100 | 380 | 27 |

In this chapter, the design and the development of a novel class of cryogenic temperature sensors, based on Fiber Bragg Gratings, are illustrated.

## 3.2 Conventional sensing techniques

For the physicists at CERN, instrument and sensor reliability is of paramount concern. Cryogenic temperature sensors are placed on each superconducting magnet to monitor the cooling of each magnet and help detect catastrophic heat surges that could cause magnet field collapse or even explosions in the magnets. If a magnetic field were to collapse on an individual magnet, this could cause subsequent magnetic field collapses on adjacent magnets, essentially creating a domino effect that could cause the collapse of multiple magnets. Downtime to repair a catastrophe like this would be significant, causing substantial delay to the research. The temperature of the cryogenic system of

the LHC is currently monitored by means of PT-100 and Cernox™ sensors. PT-100 sensors are PRT sensors whose resistance at 273 K is 100 Ω and with a lineal dependence on the temperature, as widely discussed in the previous chapter. The working temperature of the LHC cryogenic system is supposed to be between 2-300 K so the value of PT-100 resistance will vary approximately between 10-100 Ω. The uncertainty margin is 1.5 Ω and the DC voltage could reach 1900 V. Also, the use of additional isolated regulators should be avoided although this is not compulsory. Finally, the background radiation will affect the electronic devices. Theoretical simulations have shown that the expected total radiation dose will cause a displacement damage of $5 \cdot 10^{12}$ n/cm$^2$ and a total ionizing dose of 100 Gy within 10 years of LHC functioning [(69)].
Therefore, the development of the measuring system requires special devices whose characteristics fit the electrical specifications of the cryogenic system and that tolerate the expected total radiation dose. Cernox cryogenic sensors have been developed primarily to intercept these specifications and provide a more reliable monitoring system for LHC. These temperature sensing devices are fabricated from sputtered zirconium oxy-nitride thin films and have been commercially available from Lake Shore Cryotronics, Inc. under the tradename Cernox™ Resistance Thermometers (CXRTs) since 1992. These sensors possess many qualities desired in a cryogenic thermometer and are presently widely used. To date, no long term stability data has been available in the literature [(70)]. However, being an electronic device, the Cernox sensor is still affected by strong magnetic fields of the LHC and therefore suffers all the problems that have already been discussed about this topic.

## 3.3 FBG sensing principles at cryogenic temperature

As well described in Chapter 1, FBG sensing principles is based on the Bragg wavelength shift measurement with respect of the time. In particular, the temperature changes act on $\lambda_B$ by means of the coupling of two effects: *thermo-optic effect* (TOE) and *elasto-optic effect* (EOE). The dependence on these two effects is better explained by the following equation (3.1):

$$\frac{\Delta\lambda_B}{\lambda_0} = k \cdot \epsilon + \alpha_\delta \cdot \Delta T \tag{3.1}$$

This is the general form of the strain and temperature sensing for a FBG sensor, where

- $\Delta\lambda_B$ = Bragg wavelength shift
- $\lambda_0$ = base wavelength at test start
- $k = 1 - p$
- $p$ = photo-elastic coefficient, $p = 0.22$
- $k$ = gage factor, $k = 0.78$
- $\epsilon$ = strain
- $\Delta T$ = temperature change in K
- $\alpha_\delta$ = change on the refractive index, $\alpha_\delta = 5...8 \cdot 10^{-6}/K$

$$\alpha_\delta = \frac{\delta n/n}{\delta T} \tag{3.2}$$

The first expression $(k \cdot \epsilon)$ of equation (3.1) describes the strain impact caused by force $(\epsilon_m)$ and temperature $(\epsilon_T)$. The second part $(\alpha_\delta \cdot \Delta T)$ describes the change of the glass refractive index $n$ caused only by temperature.

$$\epsilon = \epsilon_m + \epsilon_T \tag{3.3}$$

where $\epsilon_T = \alpha_{sp} \cdot \Delta T$ in which $\alpha_{sp}$ is the coefficient of thermal expansion of the specimen. In case of a pure temperature sensor a Bragg grating is not stressed (the fiber then is fixed only at one point, sufficiently apart from the Bragg grating). The FBGs $\Delta\lambda_B/\lambda_B$ signal then changes only with the temperature according to equation (3.6). In this case $\alpha$ is the thermal expansion coefficient $\alpha_{glass}$ of the fiber.

$$\frac{\Delta\lambda_B}{\lambda_B} = (1-p) \cdot \alpha_{glass} \cdot \Delta T + \frac{\delta n/n}{\delta T} \cdot \Delta T = (\alpha_\Lambda + \alpha_n)\Delta T \tag{3.4}$$

The thermal sensitivity has been shown to behave nonlinearly with decreasing temperature, decreasing by a factor of two at liquid nitrogen temperatures (77 K), and becoming approximately zero at liquid helium temperature (4.2 K) [(71),(72)]. Below 40 K, the temperature sensitivity of a silica FBG drops to < 0.1 pm/K. The low intrinsic sensitivity of FBG to temperature means, for strain measurements at low temperatures, that there is no need for temperature compensation, while the FBG characteristic becomes fully invariant near temperatures of T = 4.2 K. The equation (3.1) is valid over the whole range of temperature sensing but, depending on the temperature range, the sensor response can be influenced exclusively by the TOE or the EOE or both. Then, is possible to define the following functioning regions for the FBG sensors:

**Table 3.2:** Temperature functioning regions of FBG

| Range | Temperature | Effect | Sensing equation |
|---|---|---|---|
| 1 | from 233 K to 523 K | TOE | $\Delta\lambda_B/\lambda_B = \alpha_n \cdot \Delta T$ |
| 2 | from 40 K to 233 K | TOE + EOE | $\Delta\lambda_B/\lambda_B = (\alpha_\Lambda + \alpha_n)\Delta T$ |
| 3 | from 4 K to 40 K | EOE | $\Delta\lambda_B/\lambda_B = \alpha_\Lambda \cdot \Delta T$ |

Have been defined three functioning regions in which the FBG sensor behaves very differently. In the first temperature range identified (from 233 K to 523 K), the changes in temperature produce effects exclusively on the thermo-optical coefficient of the Ge-doped silica while the contribution dues to the thermal strain is negligible. The thermal sensitivity of the FBG depends only on $\alpha_n$ and the sensitivity curve will present a quite linear behavior. In the second temperature range (from 40 K to 233 K) things get complicated: the thermal sensitivity due to the TOE decrease according to the temperature, also, the low temperature acts mechanically on the optical fibers producing their thermal expansion and a consequent thermal strain (EOE). This is the more complex functioning regime because of the superposition of these effects that are antagonists by an algebraic point of view. The third range (from 4 to 40 K), the contribution due to the thermo-optic coefficient of the Ge-doped silica is practically negligible, and the FBG sensor responds uniquely by means of the thermal-strain induced by the thermal expansion of the fiber. These information allow us to evaluate the feasibility of achieving a temperature sensor operating in the range from 4 K to 300 K but do not allow to predict its performance. In order to assess the real efficiency of a FBG sensor at very low temperature, we must consider its physical characteristics: the classical optical fibers are mainly composed by silica ($SiO_2$ - silicon dioxide) and in a small percentage by silica heavily doped with Germanium (core region) in order to increase locally the refractive index. Therefore, from a Material Science point of view, an optical fiber at cryogenic temperatures is comparable to a glass stick. Despite the thermal sensitivity of FBG sensors in the room temperature range is adequately high for exclusive effect of the thermo-optical coefficient while the thermal strain contribution is almost negligible. With the decreasing of the temperature to the cryogenic range, the thermo-optical effect gradually weakens until it disappears at around 40 K. Therefore, the thermal expansion properties of $SiO_2$ play a fundamental role in the cryogenic sensing: a high Coefficient of Thermal Expansion (CTE) is required in order to sense cryogenic temperature changes. The thermal properties of silica are listed in table 3.3:

**Table 3.3:** Thermal properties of $SiO_2$ (Silica)

| | **Unit of measure** | **SI/Metric** |
|---|---|---|
| Thermal Conductivity | W/m·K (BTU·in/ft$^2$·hr·°F) | 1.38 |
| Coefficient of Thermal Expansion | $10^{-6}$/K ($10^{-6}$/°F) | 0.55 |
| Specific Heat | J/Kg·K (Btu/lb·°F) | 740 |

The coefficient of thermal expansion $\alpha_{glass}$ of the fiber is very low; almost zero. The biggest impact results from the temperature dependent change of the refraction index $\alpha_\delta$, this suggests a low thermal sensitivity in the temperature range in where the thermo-optical does not act and then impossibility of using FBG sensors at very low temperatures. A possible way to ride, in order to realize FBG cryogenic sensors, is to exploit the thermal expansion properties of some high CTE materials by fixing the FBG on them.

### 3.3.1 Integration of FBG sensor with high CTE materials

When a fiber is fixed to a specimen, the FBG signal $\Delta\lambda_B/\lambda_B$ changes with the strain $(\epsilon_m + \epsilon_T)$ of the specimen and therefore the coefficient of thermal expansion is $\alpha_{sp}$ then and not $\alpha_{glass}$:

$$\frac{\Delta\lambda_B}{\lambda_B} = k \cdot \epsilon_m + (k \cdot \alpha_{sp} + \alpha_\delta) \cdot \Delta T \tag{3.5}$$

This suggest that it can be useful to consider the use of particular materials characterized by a high CTE and easily integrable with a fiber sensor. In fact, this would allow to fully exploit the thermo-optic effect of the fiber up to about 40 K, and compensate its intrinsic lack of thermal sensitivity below 50 K by exploiting the mechanical strain induced by the auxiliary material strongly bound to the fiber. Then, the global sensing principle of FBG bounded on a high CTE material sample, in the range from 4 K to 300 K, becomes the following:

$$\frac{\Delta\lambda_B}{\lambda_B} = (1 - p_\epsilon)\Delta\epsilon + (\alpha_\Lambda + \alpha_n)\Delta T \tag{3.6}$$

where $p_\epsilon$ is the elasto-optic coefficient of the silica and $\Delta\epsilon$ is the strain contribution induced (*apparent strain*) by the thermal expansion of the auxiliary material (specimen) on which the grating is fixed. The Bragg wavelength shifts is governed by the strain imposed by the thermal expansion of the sample to which is bonded, and by the refractive index change of the core, determined by the thermo-optic coefficient [(73)]. In the cryogenic range, the temperature-induced apparent strain may amount to several 1000 $\mu m/m$ (which equals a wavelength shift of about 0.64 nm) per 100 K, varying with the thermal elongation of the substrate [(74)]. With bare fibers the apparent strain amounts to $|\epsilon_{app}| < 1\mu m/m$. But when the FBG is fixed to a material of a substantial effective coefficient of thermal expansion (PMMA [(75)]; Teflon[(76)]) or coated with a metal [(77)], FBG-based temperature measurement is possible with high resolution. On the basis of these considerations, it was designed and, successively, developed and tested our early prototypes of cryogenic temperature sensors based on FBG.

## 3.4 FBGs bonded on a high CTE material samples

As showed in the previous section, the bonding of a FBG sensor on a substrate of a high CTE material goes to fill the gap of sensitivity at low temperature. In this section, the development of cryogenic temperature sensors *bonded* on samples of thermo-sensitive materials is treated. The principal characteristics of the sensors, the fabrication process and the experimental validation are presented. In the first class of cryo-sensors different samples of different geometry and material have been chosen to fix the FBGs.

### 3.4.1 FBG bonded on Lead (Pb) sample

Lead is a chemical element in the carbon group with symbol Pb (from Latin: *plumbum*) and atomic number 82. Lead is a soft and malleable metal, which is regarded as a heavy metal and poor metal. Metallic lead has a bluish-white color after being freshly cut, but it soon tarnishes to a dull grayish color when exposed to air. Lead has a shiny chrome-silver luster when it is melted into a liquid. Lead has a coefficient of thermal expansion $CTE_{Pb} = 29 \cdot 10^{-6}$. It was chosen due to its low electric conductivity ($4.81 \cdot 10^6$/ m·Ω) and good thermal conductivity (35,3 W/(m·K)). To realize the sensor, a FBG was glued on a Lead sample of dimensions: 14.0 x 50.2 x 2,0 mm; in the middle of the sample a rectangular groove on the longitudinal direction was made in order to house the fiber sensor, its groove dimensions are: 1.0 x 50.2 x 0.3 mm.

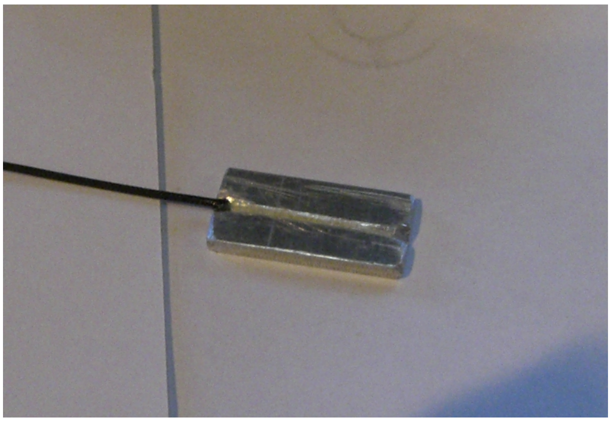

**Figure 3.1:** FBG bonded on a Lead sample.

### 3.4.2 FBG bonded on Polymethylmethacrylate (PMMA) sample

Poly(methyl methacrylate) (PMMA) is a transparent thermoplastic, often used as a lightweight or shatter-resistant alternative to glass. Although it is not technically a type of glass, the substance has sometimes historically been called acrylic glass. Chemically, it is the synthetic polymer of methyl methacrylate. The material was developed in 1928 in various laboratories, and was first brought to market in 1933 by the Rohm and Haas Company, under the trademark Plexiglas. PMMA has a $CTE_{PMMA} = 70 \cdot 10^{-6}$, an enough high value to ensure an adequate contribution of thermal-induced strain to the FBG sensor. To realize the sensor, a FBG was glued on a PMMA sample of dimensions: 14.0 x 26.6 x 1,5 mm; in the middle of the sample a rectangular groove on the longitudinal direction was made in order to house the fiber sensor, its groove dimensions are: 1.0 x 26.6 x 0.4 mm.

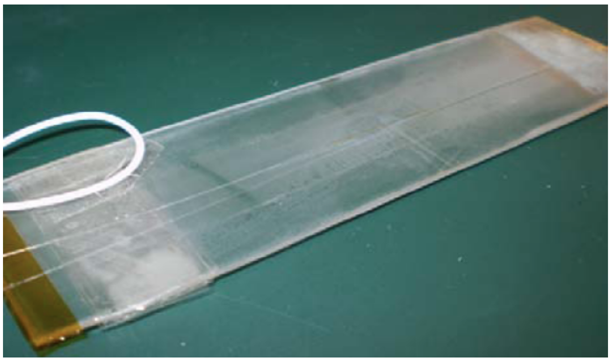

**Figure 3.2:** FBG bonded on a PMMA sample.

### 3.4.3 FBG bonded on Polytetrafluoroethylene (PTFE) sample

Polytetrafluoroethylene (PTFE) is a synthetic fluoropolymer of tetrafluoroethylene that finds numerous applications. The best known brand name of PTFE is Teflon by DuPont Co. PTFE is a fluorocarbon solid, as it is a high-molecular-weight compound consisting wholly of carbon and fluorine. PTFE is hydrophobic: neither water nor water-containing substances wet PTFE, as fluorocarbons demonstrate mitigated London dispersion forces due to the high electronegativity of fluorine. PTFE has one of the lowest coefficients of friction against any solid. PTFE is a thermoplastic polymer, which is a white solid at room temperature, with a density of about 2200 kg/m$^3$. According to DuPont, its melting point is 600 K (327 °C). Its mechanical properties degrade gradually at temperatures above 194 K (?79 °C). PTFE gains its properties from the aggregate effect of carbon-fluorine bonds, as do all fluorocarbons. The only chemicals known to affect these carbon-fluorine bonds are certain alkali metals and most highly reactive fluorinating agents. Its CTE is $CTE_{PTFE} = 86 \cdot 10^{-6}$. A FBG was glued on a PTFE sample of dimensions: 13.0 x 28.5 x 0,5 mm. It was not necessary to create a groove due to its low coefficient of friction.

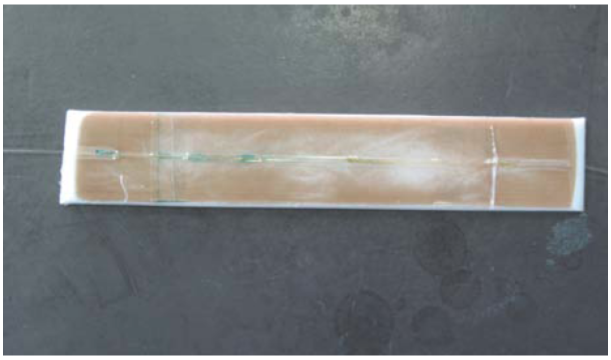

**Figure 3.3:** FBG bonded on a Teflon sample.

### 3.4.4 Gluing process

For the FBG sensor gluing process not any adhesive can be used for cryogenic application. Under CERN experience it was discovered that the M-BOND 610 adhesive from HBM GmbH is suitable for low temperatures. This is an epoxy resin adhesive that requires heat and pressure for curing. On the other hand any radial residual deformations of the fiber after bonding and curing procedure are not allowed. The surface of the sample has been rubbed in order to obtain the right roughness to host the fiber, and then it has been cleaned and dried.

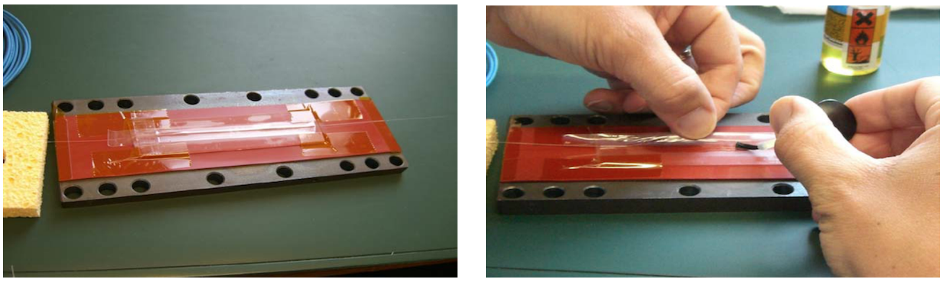

**(a)** Fiber fixed on a PMMA sample.

**(b)** Gluing.

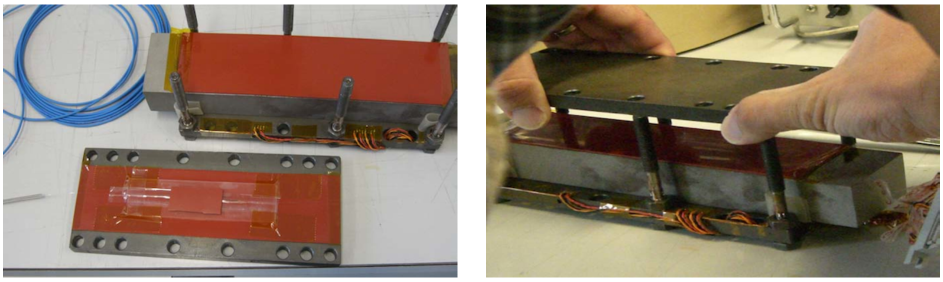

**(c)** Silicon rubber on the part of the fiber without coating.

**(d)** Steel plates with screw-clamp.

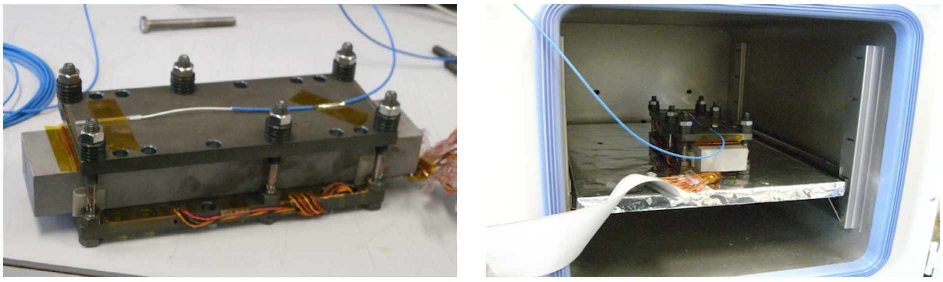

**(e)** Steel plates with screw-clamp screwed.

**(f)** Curing process at 90°C.

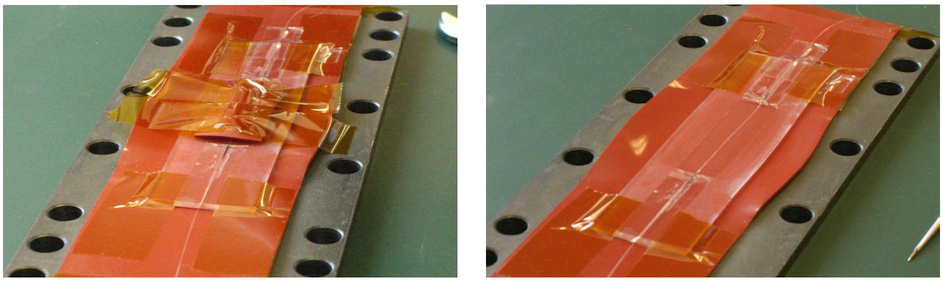

**(g)** Result after heat treatment.

**(h)** PMMA sample and fiber after heat treatment.

**Figure 3.4:** Gluing process sequence.

A chamfer was created on the small side of the sample in order to avoid any break of the fiber when the sample is going to be under pressure. The surface of the optical fiber was degreased by cleaning agent RMS-1. The sample was fixed with kapton tape on a piece of silicon rubber, while the optical fiber was aligned and fixed on the specimen with Mylar tape without applying any prestress Figure 3.4a. To put the glue between the fiber and the PMMA sample the tape has been kept fixed on one longitudinal side, while the other side, with the fiber attached, has been moved away in order to place the glue under the fiber (see Figure 3.4b. At this stage the fiber and the tape have been fixed again, a piece of silicon rubber has been placed on the part of the fiber without coating for an equal partitioning of the load on the fiber (see Figure 3.4c). The sample was placed between two steel plates (see Figure 3.4d and 3.4e) and a low pressure was applied to steel plates using screw-clamp during curing, for an amount of 100-150 $\mu\epsilon$. After six hours of curing at 100 °C the sticky tape was removed and the fiber was left to reach the room temperature.

**Table 3.4:** Wavelength shift and corresponding equivalent strain during the gluing process.

| | **Initial $\lambda_B$ [nm]** | **Final $\lambda_B$ [nm]** | **Wavelength shift [nm]** | **Equivalent strain [$\mu\epsilon$]** |
|---|---|---|---|---|
| 6 h curing | 1550.60 | 1551.06 | + 0.46 | + 460 |
| 24 h from gluing | 1551.06 | 1545.79 | - 5.27 | - 5270 |
| Dismantling plate | 1545.79 | 1543.50 | - 2.29 | - 2290 |
| $1^{st}$ LN cycle | 1543.50 | 1543.20 | - 0.30 | - 300 |
| $2^{nd}$ LN cycle | 1543.20 | 1543.48 | + 0.28 | + 280 |
| $3^{rd}$ LN cycle | 1543.48 | 1543.29 | - 0.19 | - 190 |
| After 3 LN cycles | 1543.50 | 1543.29 | - 0.21 | - 210 |
| **Whole cycle** | **1550.60** | **1543.29** | **-7.31** | **-7310** |

In some cases we observed that during the curing process the fiber was broken in two points in the part without coating, maybe it can be due to the effect of the curing on the piece of silicon rubber (see Figure 3.4g). To avoid this kind of problems we arranged a new gluing test with a polymide recoated FBG (CWL 1550 nm) with the same procedure of the old test. In this case no piece of silicon rubber was placed on the 8 mm recoated part of the fiber but a thin layer of Teflon have been placed on the sample in order to avoid that the two plates of silicon rubber could be glued to each other. During the curing in the oven at 97°C a pre-stress amount of 80 $\mu\epsilon$ was applied instead of 150 $\mu\epsilon$ like in the previous test.

Afterwards three thermal cycles in the liquid Nitrogen were performed in order to verify that the whole process was successful and the sensor could stand the LN temperature (77 K). Finally the sensor was successfully glued on the PMMA sample, during the thermal shock it was possible to see a wavelength variation of the FBG of about 12nm.

### 3.4.5 Experimental setup

The sensors were tested using two different experimental setups to reach different cryogenic temperature states: liquid nitrogen (LN 77 K) and liquid helium (LHe 4.2 K).

**Liquid Nitrigen - 77 K**

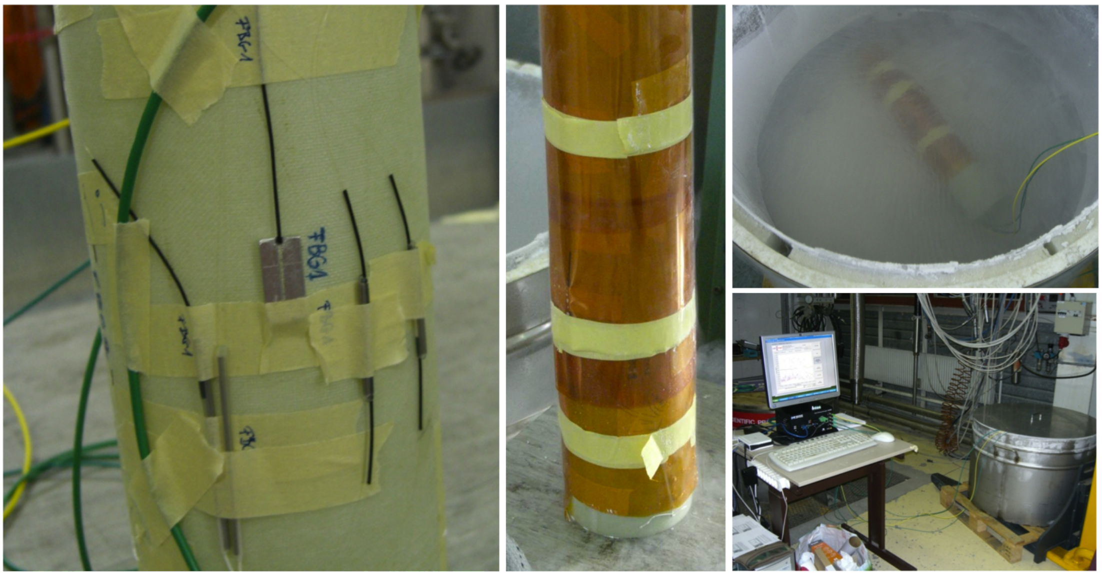

**Figure 3.5:** Experimental setup used in the Liquid Nitrogen tests.

A open dewar filled with liquid nitrogen (LN) was used as test bench. The samples were fixed on a Vetronite tube. To protect the fibers a Kapton foil has been wrapped around the tube. The configuration is shown in Figure 3.5. As optical read-out system we used a Micron Optics sm125-500 Optical Sensing Interrogator, which implements the ENLIGHT Sensing Analysis Software.

In order to compare each FBG response with a reference sensor response in the same conditions, 1 PT100 (a Platinum Resistance Thermometer) per sensor was fixed between the tube and the samples. The reference sensors were glued with Araldite Rapid (Fast- setting epoxy adhesive) and heated with ad infrared lamp (∼30/35°C) in order to have a faster fixing time. Then it was necessary to wait 24 hours before starting the measurements. As PT100 Data Acquisition System (DAQ) was used a Keithley read-out system connected by GPIB bus to a SUNMTA60, the read-out software used is Labview.

Several nitrogen immersion were performed in order to collect enough data from FBG and to compare them with the PT100 responses.

### Liquid Helium - 4.2 K

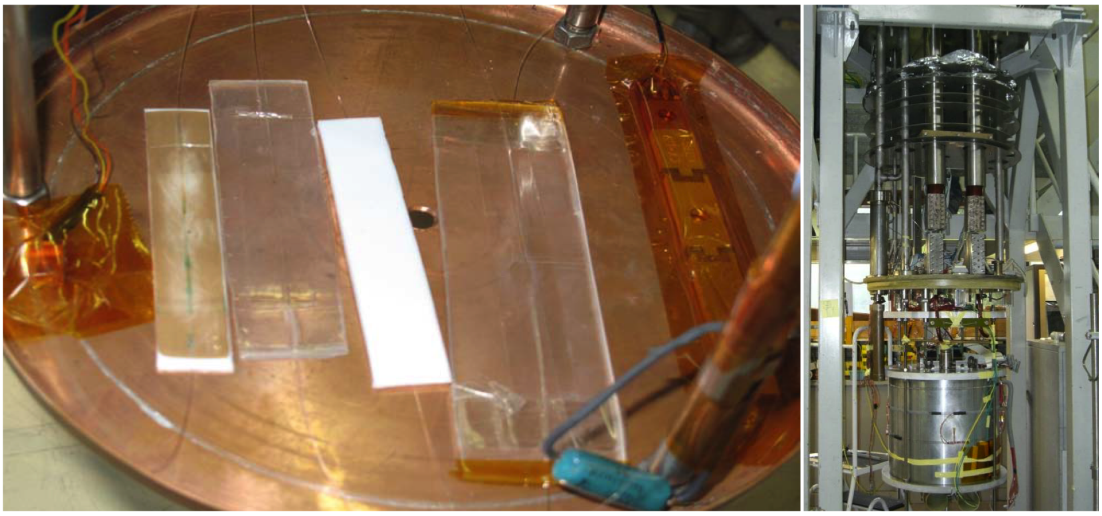

**Figure 3.6:** Experimental setup used in the Liquid Helium tests.

A closed cryostat was used to carry out the tests. The cryostat is filled with 60 cm of Liquid Helium (LHe). The level of the liquid inside the cryostat is read from a level gauge which goes down from the top of the cryostat to the bottom. As soon as the temperature inside the cryostat is stabilized at 4.28 K the heating starts to evaporate the LHe until the level gauge reading is 0 cm. The *warm* gas is collected by a gazometer by the time. The heater power was about 15 W. After the first and the second cooldown, when the temperature was stabilized at 4.28 K, it was possible to heat the cryostat until the Liquid Helium evaporated and the only Helium gas was inside the cryostat. When no more Liquid was inside it, the heater has been switched off and the cryostat has been left to warm up naturally. Dues to this procedure it was possible to have more cycles. Only the last warm up was completely due to the heater which was switched off when the temperature reached 297 K and switched on again when it was 285 K.

The setup consists in a 18.5 cm diameter copper plate, which is at 8 cm of distance from the bottom of the cryostat and where the samples are fixed and placed horizontally. Figure 3.6 shows the the FBG sensors and the reference sensors on the copper plate. As optical read-out system we used a Micron Optics sm125-500 Optical Sensing Interrogator, which implements the ENLIGHT Sensing Analysis Software.

The reference sensors used are PT100 PRT and Cernox (dimensions: 104 x 10 mm) , a Keithley read-out system connected by GPIB bus to a SUNMTA60 and a National Instruments DAQ are used to acquire the reference data, respectively. The reference sensor is fixed by the Kapton tape on the copper plate. On this plate is also placed the heater used to evaporate the LHe soon after the cryostat reaches 4.2 K.

Several liquid helium immersion cycles were performed in order to collect enough data from FBG and to compare them with the PT100 and Cernox responses.

### 3.4.6 Experimental results

Several cryogenic cycles were performed in both LN and LHe setups, in this subparagraph the most relevant results are reported and discussed.

#### Liquid Nitrogen - 77 K

The early cryogenic tests were been conducted in LN in order to obtain preliminary information on the feasibility of FBG cryogenic sensors, due to the lower costs of the experimental setup. The samples were immersed in the filled dewar, leaving completely evaporate the Liquid Nitrogen until the dewar reaches the room temperature. When the sensors were immersed in the liquid nitrogen (cool-down), there has been a sharp Bragg wavelength shift due to the thermal strain on the samples. While, during the heating phase (warm-up), the $\lambda_B$ changes have been slow and without temperature fluctuations. Figure 3.7 shows the FBG response during three cryogenic cycles:

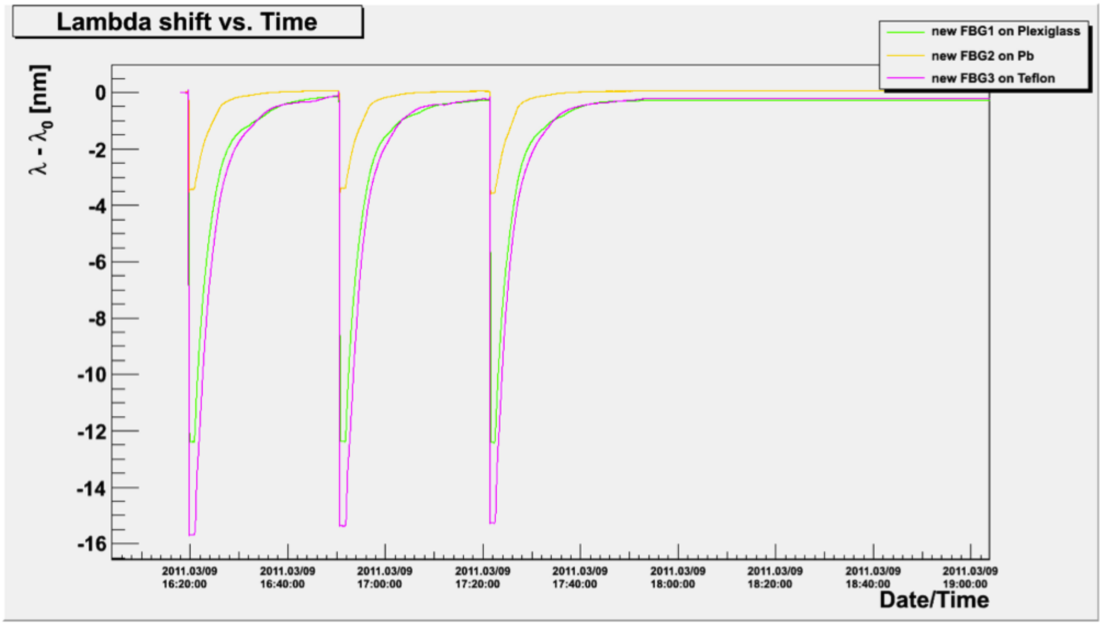

**Figure 3.7:** Bragg Wavelength response with respect of the time, during three cryogenic cycles.

This is the first cryogenic test on these samples: it can be noticed that in the first cool-down the $\lambda_B$ shifts of the FBGs present a larger dynamic due to the need of a *training* phase at cryogenic temperature, the samples need to thermalize. After this phase, the measurement are repeatable with a good agreement. There were been performed further LN cycles to validate the repeatability, the stability and the sensitivity of the FBG sensors. In figure 3.8 there are reported the wavelength shift of the sensors during a long cryogenic test, in which there were been performed five cool-down and five warm-up. As it is clearly evident, the wavelength shift of the FBg sensor bonded on a lead sample presents the smaller dynamic (approximately $|\Delta\lambda_{B,Pb}| = 3.40$ nm), while the wavelength shift of FBG sensors glued on PMMA and PTFE have a dynamic significantly larger ($|\Delta\lambda_{B,PMMA}| = 12.40$ nm, $|\Delta\lambda_{B,PTFE}| = 15.50$ nm). This is in perfect agreement with the theory, in fact, Teflon is the material with the greater CTE, followed by PMMA and Lead.

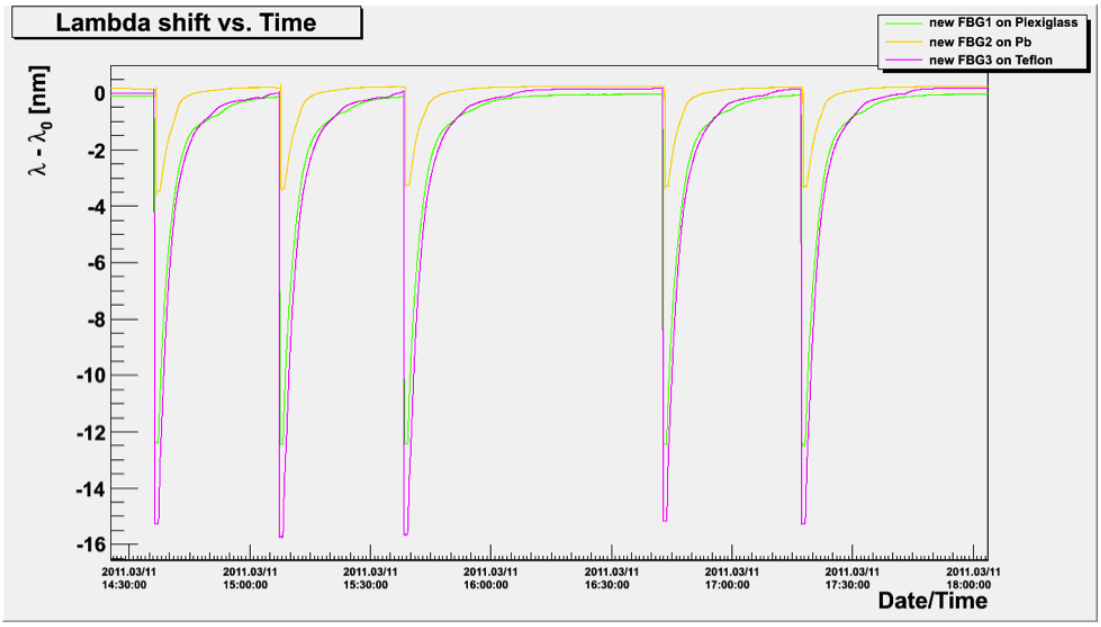

**Figure 3.8:** Bragg Wavelength response with respect of the time, during a long cryogenic test.

By comparing the $\Delta\lambda_b$ measurements carried out by FBG sensors and the T measurements provided by the reference sensors, the sensitivity curves were been calculated on the 8 LN cycles performed by using a specially developed algorithm. The sensitivity curves were calculated exclusively on the basis of the warm-up data as the temperature changes are sufficiently slow to ensure the quasi-static conditions of measurement, needed to get a reliable correspondance between the wavelenght shift and the cryostat temperature. The sensitivity curves and the fitting function for each sensor are reported in Figure 3.9, 3.10 and 3.11.

PTFE and PMMA showed good thermal expansion/contraction properties, also confirmed by the sensitivity curves which show a high slope behavior. On the basis of these considerations, it was decided to discard the configuration FBG-Lead and continue to develop sensors only with PMMA and PTFE.

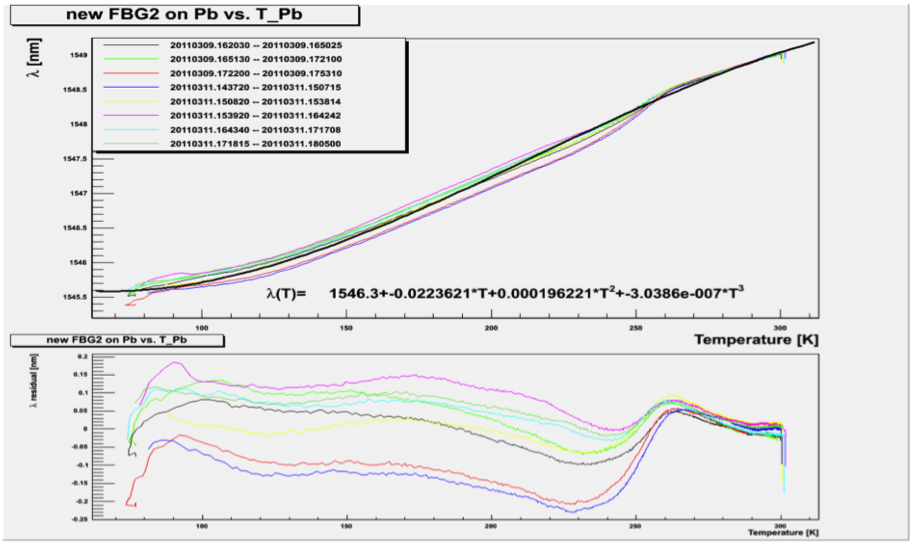

**Figure 3.9:** Sensitivity curve and fitting function from experimental data for FBG bonded on Pb.

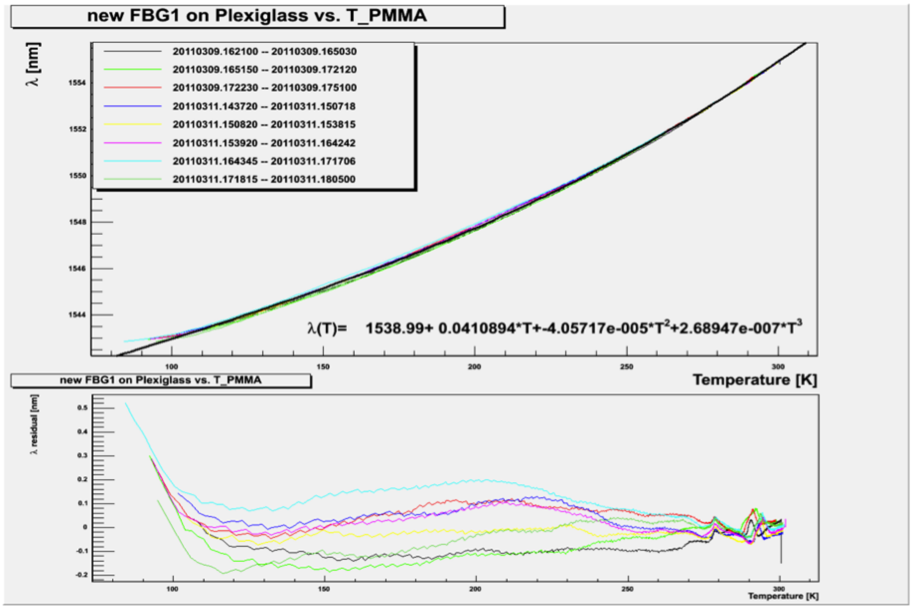

**Figure 3.10:** Sensitivity curve and fitting function from experimental data for FBG bonded on PMMA.

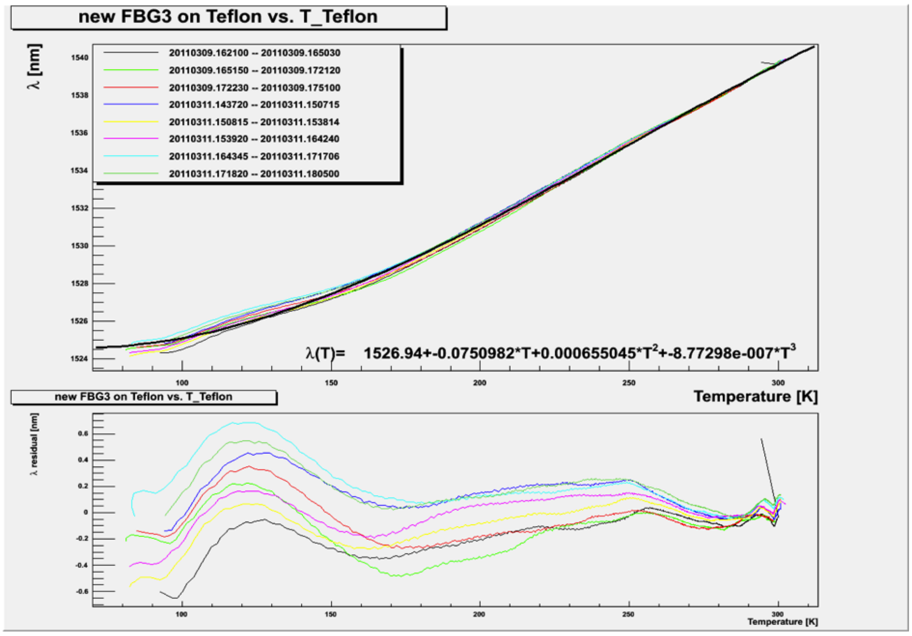

**Figure 3.11:** Sensitivity curve and fitting function from experimental data for FBG bonded on PTFE.

## Liquid Helium - 4.2 K

After the preliminary tests in Liquid Nitrogen, a cryostat filled with 60 cm of Liquid Helium was used to test the cryo-sensors. In these test the lower temperature was 4.2 K and the room temperature was 297 K. Preliminarily, there were been performed only few run in order to allow the sensors to thermalize at 4.2 K and to prevent serious damage caused by low temperature. In these tests only PMMA and PTFE samples were been used as auxiliary substrate due to their good thermal expansion properties. In particular, there were been used 2 PMMA-bonded sensors, 1 PTFE-bonded sensor and 1 PTFE-sandwiched sensor.

A long run was performed in order to reach quasi-static measurement condition, after a sufficient period of thermalization. In the long run, have been necessary about 2 days to warm-up from 4.2 K to 297 K. This allowed to use the data obtained for the sensors calibration in quasi-static condition. In figure 3.12 and 3.13, the PTFE-sandwiched sensor was broken during the test.

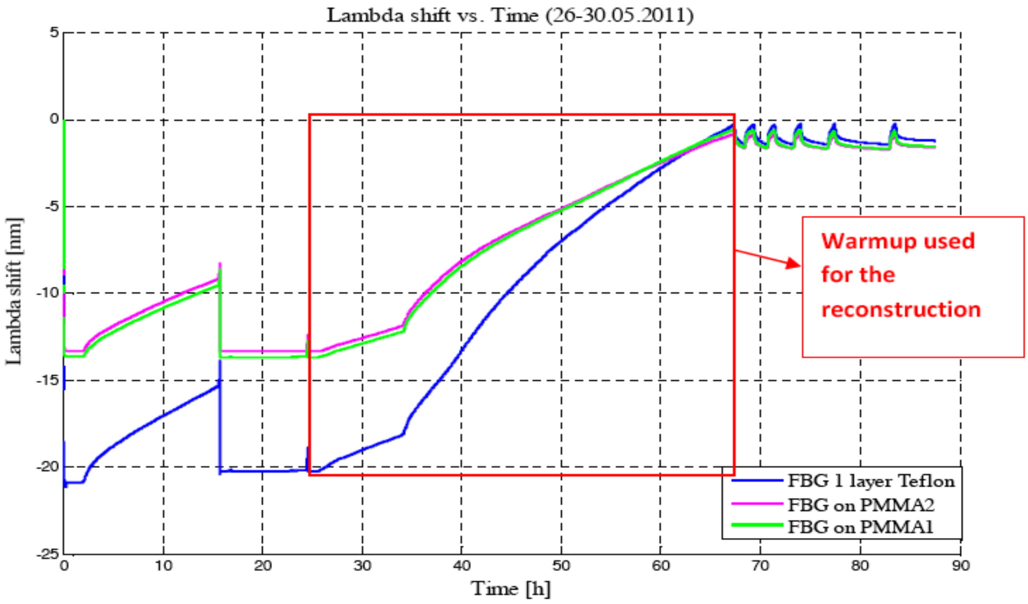

**Figure 3.12:** Bragg Wavelength response with respect of the time, during the long LHe run.

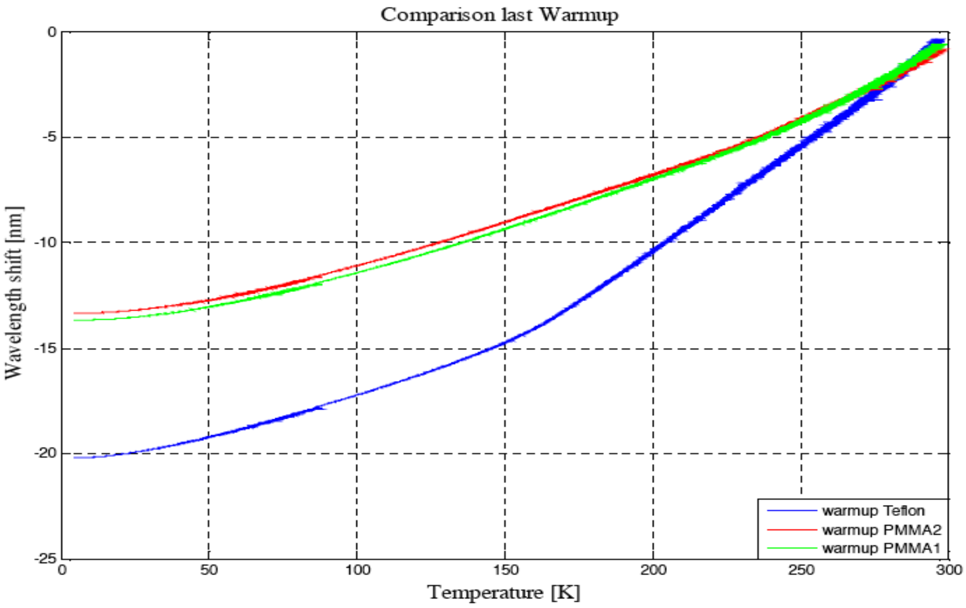

**Figure 3.13:** Sensitivity curve from experimental data for FBG bonded on PMMA and PTFE samples.

As shown in Figure 3.13 the two PMMA-bonded sensors behave in a similar way, except for a slight shift in wavelength, their sensitivity curves are almost superimposable. Instead, the PTFE-bonded sensor behaves differently, presents a dynamic greater than the PMMA-bonded but its sensitivity curve is strongly non-linear and has a sharp change in slope around 168 K. This implies what will be problematic the calibration of these sensors.

### 3.4.7 Bonded FBG Sensor calibration

The calibration procedure of a sensor is a crucial step to achieve a good degree of measurement accuracy. A well-done calibration requires a good measurement stability and a reliable reference sensor. A low variance of the measurements provides a good degree of stability. Being the thermal sensitivity of cryogenic temperature sensors strongly non-linear, to carry out the calibration of these sensors is necessary to use high-order polynomial fitting techniques to obtain a reliable reconstruction of the measurand. For FBG sensors bonded on a PMMA substrate, it was found that by using a fifth-order polynomial fitting function it is possible to make a high resolution in the range 30-300 K [(75)].
The calibration procedure starts from the evaluation of the fitting curves of the long warm-up. because of the strong non-linearity, were considered three cases of study:

1. A single Polynomial function to fit the sensitivity curves in the whole range of temperature;

2. An Impulsive function used to fit the sensitivity curves at low temperature together with a Polynomial function to fit the remaining range of temperature;

3. A Look-Up-Table (LUT) approach to fit the sensitivity curves in the whole range of temperature with a given computational complexity.

Obviously, this study was carried out for each type of sensor. For brevity of discussion, there are taken into account only one PMMA-bonded sensor and one PTFE-bonded sensor.

#### PMMA-bonded sensor: Temperature reconstruction

In order to calibrate the FBG sensors, there were used the following methods.

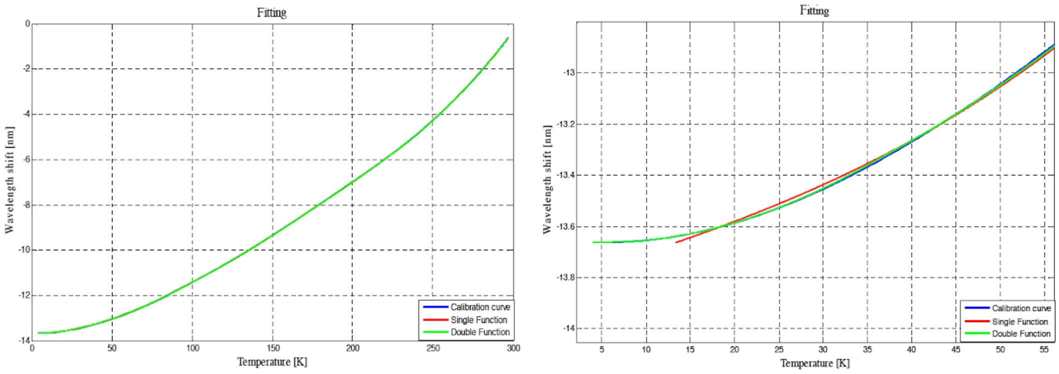

**(a)** Fitting curves comparison.

**(b)** Fitting curves comparison: low temperature zoom.

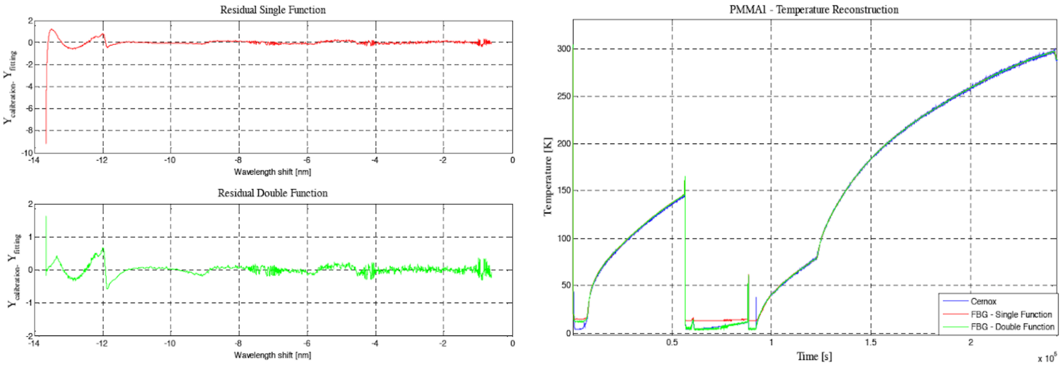

**(c)** Residuals between the calibration curve and the fitting curves.

**(d)** Temperature reconstruction.

**Figure 3.14:** PMMA-bonded FBG sensor.

Single function:

$10^{th}$ order Polynomial Function

$$y = a + bx + cx^2 + dx^3 + ex^4 + fx^5 + gx^6 + hx^7 + kx^8 + lx^9 + mx^{10}$$

Double function:

- impulsive function in the range from 4.28 K to 35 K.

$$y = a + b\left(\frac{x-c}{d}\right)\left(\frac{|x-c|}{d}\right)^{-e}$$

- $10^{th}$ order Polynomial Function

$$y = a + bx + cx^2 + dx^3 + ex^4 + fx^5 + gx^6 + hx^7 + kx^8 + lx^9 + mx^{10}$$

Figure 3.14 reports the most relevant plot about this calibration procedure. As it is evident, the best reconstruction is given by using the double function. This approach can guarantee a good temperature reconstruction over the range from 4.28 K to 300 K but, it is very expensive from a computational complex point of view. To overcome this limitation, it was been proposed a calibration method based on look-up-table (LUT) in order to obtain a high precision with a low complexity. The sensitivity at 6 K of the sensor was estimated to be $\partial\lambda_B/\partial T = 0.7pm/K$.

### PTFE-bonded sensor - Temperature reconstruction

In order to calibrate the FBG sensors, there were used the following methods.

Single function:

$10^{th}$ order Polynomial Function

$$y = a + bx + cx^2 + dx^3 + ex^4 + fx^5 + gx^6 + hx^7 + kx^8 + lx^9 + mx^{10}$$

Double function:

- impulsive function in the range from 4.28 K to 35 K.

$$y = a + b\left(\frac{x-c}{d}\right)\left(\frac{|x-c|}{d}\right)^{-e}$$

- $19^{th}$ order Polynomial Function

$$\begin{aligned} y = {} & a + bx + cx^2 + dx^3 + ex^4 + fx^5 + gx^6 + hx^7 + kx^8 + lx^9 + mx^{10} + \\ & + nx^{11} + ox^{12} + px^{13} + qx^{14} + rx^{15} + sx^{16} + tx^{17} + ux^{18}x^{19} \end{aligned}$$

Figure 3.15 reports the most relevant plot about this calibration procedure. The sensitivity at 6 K of the sensor was estimated to be $\partial\lambda_B/\partial T = 3.2pm/K$

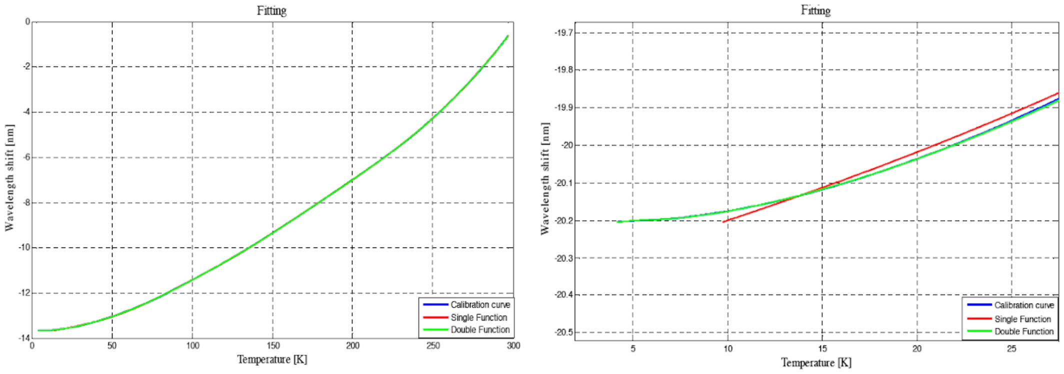

**(a)** Fitting curves comparison.

**(b)** Fitting curves comparison: low temperature zoom.

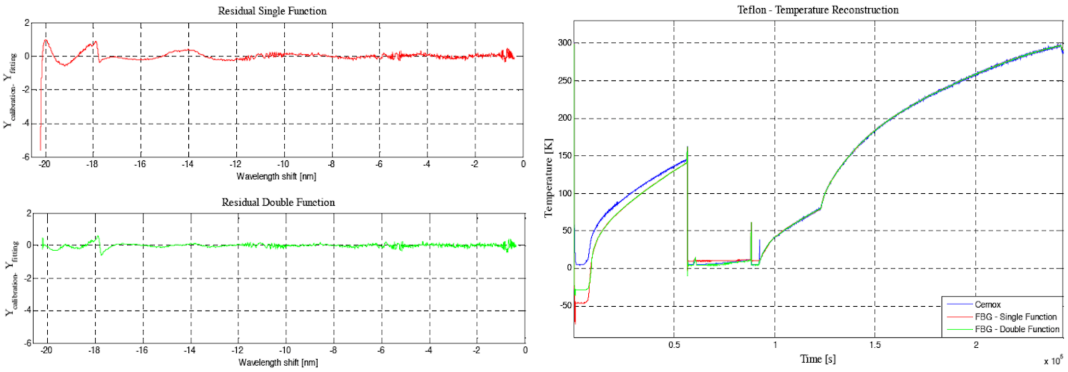

**(c)** Residuals between the calibration curve and the fitting curves.

**(d)** Temperature reconstruction.

**Figure 3.15:** PTFE-bonded FBG sensor.

## Look-Up-Tabel (LUT)

The main limitation due to the use of high-order polynomial fitting function is the high computational complexity because of the large number of elementary operations to be performed for each point. In order to decrease the computational complexity of the polynomial approach, we implemented a calibration technique based on the filling of a look-up-table and the implementation of a quick search function that returns, within the shortest possible time, the temperature value related to the shift in the Bragg wave-

length. The size of the look-up-table can be selected according to the requirements in terms of accuracy and processing time of the measurement data.
Our calibration technique consists in to fill a two-columns table (look-up-table) with the wavelength shift of the FBG sensors and the temperature data from the reference sensors used to determine the calibration curves. In this way we created a correspondence table between temperature and wavelength shift. Being the data very dense (acquisition rate equal to 1 Hz) and the resolution in temperature of an FBG sensor equal to 0.1 K (about 9.9 pm/K), the sizing of the look-up-table was chosen in order to reduce computation complexity while preserving the sensor resolution: given a dynamic of about 300 K, we have compressed the data of sensitivity in order to get 10000 points, which corresponds to having a temperature sampling period of about 0.03 K ($< 0.1$ K) [(78)].

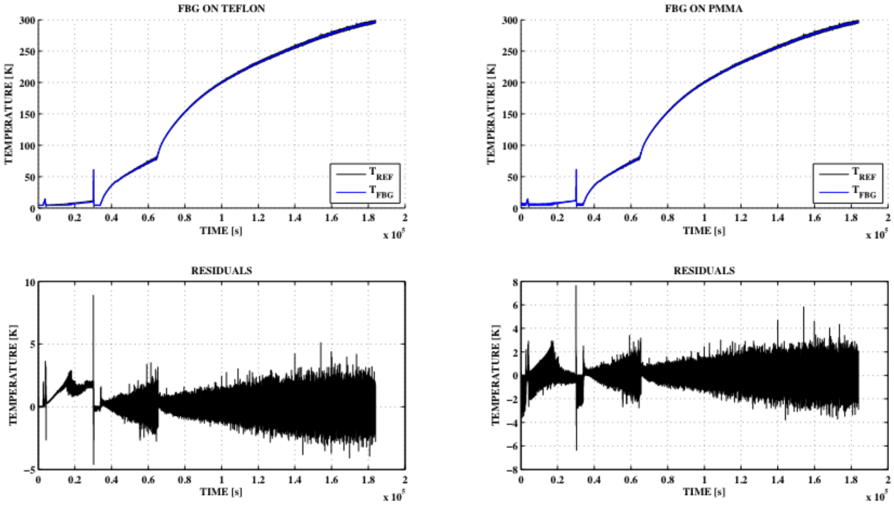

**Figure 3.16:** Reconstruction of a LHe warm-up: in the upper part of the figure, the blue line is the temperature measured by the FBG sensor, the black line is the temperature measured by the Cernox reference sensor. In the lower part are plotter the residuals.

The number of points can be reduced or increased as desired depending on the degree of accuracy and computation complexity to be achive. Once chosen the number of points and filled the look-up-table, we have implemented a quick search function that from an array containing the FBG wavelength shift, creates a new array containing the temperature measurements.

As shown in Figure 3.16, the look-up-table calibration provides a good agreement between the temperature measurements performed with the FBG sensors and those performed with the reference sensors. From the residuals plot the very good agreement of the two curves is evident.

For both types of cryogenic temperature sensors the sensitivity curves have been determined in the temperature range from 4.2 K to 300 K. We observed for the FBG bonded on PMMA (FBG1) a maximum wavelength shift of -13.1 nm. For the FBG bonded on Teflon (FBG2) the maximum wavelength shift is equal to -19.9 nm. The sensitivity curve of FBG2 presents a net slope change between -150 K and -200 K that constrains to use a very complex fitting function to provide an effective calibration of this type of sensor. Also, the sensitivity curve of FBG1 presents a non-linear behavior but without the sharp changes of slope that makes it more suitable to be interpolated with a polynomial function than FBG2. For both FBG sensors, the use of look-up-table (LUT) has allowed to reduce significantly the computation complexity of the measurement software, reducing the processing time and measurement errors caused by the non-perfect fit of the polynomial functions, especially at low temperatures ($T < 30$ K).

### 3.4.8 Conclusions

FBG cyogenic temperature sensors bonded on high CTE material samples have been fabricated, tested and calibrated. The testing was conducted at Cryolab (CERN) by using two different experimental setups that have allowed to reach two different states of cryogenic temperature (77K and 4.2 K). The gluing process of the FBG sensors on substrates has proved suitable for cryogenic applications since there were no partings or breakage. During the testing, it was found that at cryogenic temperature the thermo-mechanical behavior of Lead does not allow to perform low temperature measurements with a adequate sensitivity, this material was discarded. It was found that PMMA and PTFE have excellent thermo-mechanical properties, this allowed us to make measurements at very low temperature and plot the sensitivity curves of these optoelectronic sensors.

The calibration has been performed only on sensors glued on PMMA and PTFE: it was necessary to implement high-order polynomial functions to fit the sensitivity curves of the sensors, which were characterized by strong non-linearity probably due to the inhomogeneity of the sensor geometry. In particular, to calibrate the sensor glued on PMMA has been employed a $10^{th}$ polynomial order function, while for the sensor glued on the PTFE has been employed a $19^{th}$ polynomial order function. The employing of polynomial functions is very onerous from the computational point of view, for which it was developed a proper calibration algorithm based on look-up-table that allow to significantly reduce the computational complexity in order to obtain fast measurements with a chosen degree of accuracy.

## 3.5 FBGs coated with highly thermo-sensitive materials

To overcome the problem of the non-linear response of the bonded sensors, has been proposed a novel configuration FBG-material characterized by having an homogeneous longitudinal section. In fact, it is seen that a FBG glued on a thermo-sensitive substrate, at cryogenic temperature undergo a longitudinal strain mainly along the surface portion in contact with the substrate as the glue is not able to uniformly distribute the tensional stress over the whole volume of the FBG. The new configuration of cryogenic sensor consists of a FBG coated with a thermo-sensitive material, that provide a uniform stress distribution along the FBG. In this section the fabrication process, the testing carried out, the calibration and the results are reported and discussed.

### 3.5.1 Fabrication process

Fiber Bragg Gratings have been provided by Welltech Instrument Company Limited (Hong Kong) with the following specifications: grating length 10 mm; Bragg wavelength tolerance 0.5 nm; reflectivity $> 90\%$; FWHM (full width at half maximum of the spectrum) $< 0.3$ nm.

**Coating materials**

Polymeric coatings around FBGs were produced using two classes of polymeric precursors: epoxy and acrylic. For the epoxy based polymer, precursors are DGEBA high purity liquids with an EEW of 170-175, multi-functional aliphatic amine as hardener and a tertiary amine as catalyst. The employed epoxy system was supplied by Elantas Camattini (Italy) under the label, EC-170 + IG 824-K24. PMMA precursors were arranged in a two-component system: a very fine PMMA powder mixed with a peroxide catalyst and a liquid mixture, characterized by the presence of methylmethacrylate monomers, crosslinking agent and initiator. The acrylic system was supplied by Heraeus (Paladur). The powder and the liquid mixture were premixed in the right proportion and then quickly used due to its rapid reaction time (within a few minutes).

### Coating methods

Epoxy based and acrylic polymers were obtained starting from its liquid precursors by in situ polymerization, and then reactive casting was employed as most suitable manufacturing process to realize the coated FBG samples. This solution allows producing an interface between polymeric material and fiber cladding, which ensures an efficient strain transfer from the polymer system to fiber.

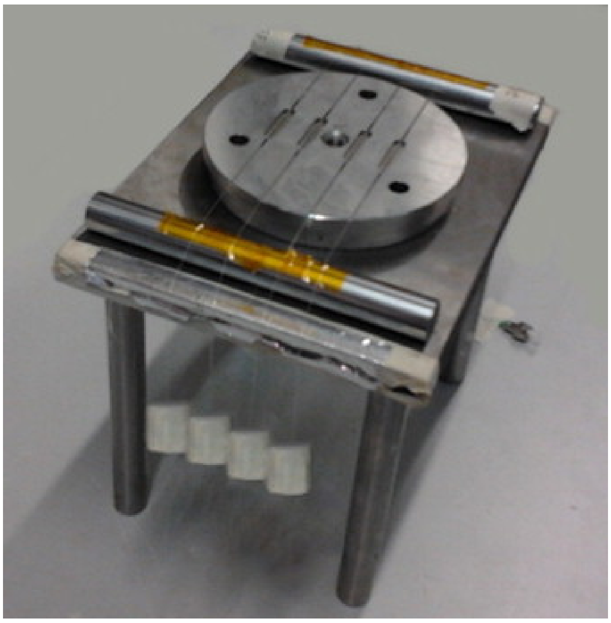

**Figure 3.17:** Mould setup for manufacturing of polymer coating FBG.

Polymer precursors are liquid and highly compatible with silica, which represents the main constituent of the fiber cladding, and thus a good surface wetting could be achieved before polymerization. After the fiber was cleaned with isopropylic alcohol, the polymeric material was casted around the cladding section near the Bragg grating. The final nominal dimensions of coating of the fiber containing the Bragg grating were 2.5 mm height, 5.0 mm width, and 25.0 mm length. To carry out the manufacturing process by reactive casting, an optimized mould was realized (the inferior half mould is reported in Figure 3.17). In the manufacturing setup, a constrain system was accurately designed in order to induce pre-alignment and pre-stress to the FBG sensor and at the same time to control the chemical shrinkage due to the polymerization reaction during the first curing stage. An extra post-curing stage was considered for both reactive systems by using a constrain-free configuration; this was to allow the natural rearrangement of the system and to reduce the local interfacial stresses between polymer coating and cladding near the FBG grating. For each polymeric coating, four different specimens were prepared at once, in order to obtain fully comparable items. Both systems exhibit a very low viscosity at room temperature, which facilitates the casting process but, conversely, it allows air inclusions during premixing operation. To overcome this inconvenience, mixing stage was performed by using a planetary mixer under vacuum (10 kPa abs) at room temperature. For the epoxy based system, all components were premixed in the right proportion (100:14, according to supplier data sheet) to obtain a reactive mixture and, then, degassed to prevent gas entrapment in the final product. After degassing the casting was performed very quickly. The curing profile was then divided in two steps: a preliminary curing stage at room temperature for 12 h and a post-curing stage at 100 °C for 4 h. For the acrylic systems, the premixing stage was slightly different, due to both the presence of the solid component to dissolve in the liquid one and the long lasting degassing stage not suitable for such a quick reactive system. For these reasons, the component mixing was a very critical operation; however, by adding the solid component into the liquid and mixing very carefully it was found that air entrapment sensibly reduce allowing to abbreviate the degassing stage. For the acrylic system the first polymerization stage was very fast, as gelation occurred in a few minutes and solidification in less than 1 h. Post curing stage was the same as for epoxy system.

### 3.5.2 Experimental setup

The samples were positioned in a dedicated sample holder and then inserted into the cryostat as shown in Figure 3.18a. The FBG sensor holder consists in a small copper box assuring a good thermal stability among the FBG fibers and the reference temperature sensors. Two temperature sensors, one of a type Cernox and another thermo resistive Platinum thermocouple (PT100), previously calibrated, where used to monitor the ambient temperature.

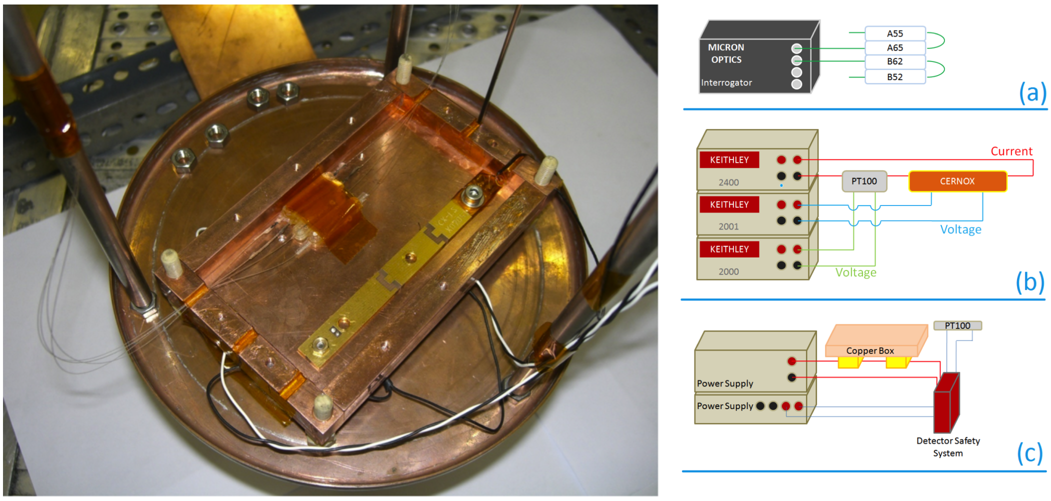

**(a)** Copper plate with FBG sensors and Cernox reference sensor.

**(b)** Schematic drawing of the DAQ: (a) the optical measurement; (b) the readout of the reference temperature sensors; (c) the heater with the PR 4116 Universal transmitter-DSS.

**Figure 3.18:** Experimental setup.

The cooling down of the system was performed by using liquid helium pumped into the cryostat until the final temperature reached 4.2 K. Due to this pumping operation, the cool-down turned to be too rapid and later analysis proved that the thermal equilibrium could not be reached within the sample holder. In contrary, the warmup could take sufficiently long time, since the liquid helium was allowed to boil away in the cryostat. In order to control the warm-up, resistors were placed at the bottom of the sample holder; however, since no further helium was pumped into the holder, this setup did not allowed a suitable temperature stabilization and thus only a slow and poor controlled warming-up stage could be achieved. The two temperature sensors were connected electrically in series and powered by a Keithley 2400 source meter operating in a constant current source mode. Voltage readouts were performed by a Keithley 2000 and a Keithley 2001 precision DMM devices. In order to reduce the bias on the measured temperature associated to the Seebeck-effect, voltage drops on both temperature sensors were read out at different polarities and the voltage drop readouts were averaged to compute temperature values. This temperature value then served as an input for the proportional warm-up control. The resistors were connected to a TTi TSX3510 power supply. All three Keithleys and the TTi devices were connected to a GPIB bus that controlled by customized software through a Prologix GPIB-ethernet controller. A schematic diagram showing all the instruments used in the experimental set up for the data acquisition is reported in Figure 3.18b, where the optical measurement (a), the readout of the reference temperature sensors (b) and the heater with the PR 4116 Universal transmitter-DSS (c) are drawn. Four different FBG sensors were located in the sample holder. In order to increase the reliability of the sensors, two epoxy coated FBGs were spliced together and both ends were brought out from the cryostat. The same setup was built for the PMMA coated sensors.

This configuration, allowed the readout on all sensors from both sides, so data were assured to be recorded even in case of optic fiber break. One end of the epoxy sensors array and one end of the PMMA sensors array were connected to a Micron Optics sm125-500 Optical Sensing Interrogator.

### 3.5.3 Results and discussion

Data acquisition has been performed for several cooling down and warm up cycles. The experimental dataset consists of two types of signal: voltage from the thermal resistive sensors (PT100 and Cernox) and central reflected wavelength signals from FBG sensors. The experimental data from the cryogenic test-bench was stored in a Network-attached Storage unit (NAS) situate at CERN and off-line processed. Figure 3.19(top) shows the temporal evolution of the Bragg wavelength for all the FBG sensors. The letter A represents the epoxy-coated sensor while the letter B represents the PMMA coated sensor. The two digits indicate the sensors reference Bragg wavelength in nanometers at room temperature (e.g. 62 stands for 1562 nm). Figure 3.19(bottom) shows the time evolution of the temperature, as measured by the Cernox sensor. In total 16 different warmup and 16 cool-down steps were performed. Raw data related to the Bragg wavelength and temperature evolution, as reported in Figure 4, were computed according to equation (3.7):

$$ln\left(\frac{\lambda}{\lambda_0}\right) = \left((1-p_\epsilon)\frac{\alpha_c H_c + \alpha_{glass} H_{glass}}{H_c + H_{glass}} + \xi\right)(T - T_0) \tag{3.7}$$

normalizing the sensor responses to the room temperature and to the reference Bragg wavelength. Figure 3.20a reports the normalized sensors output as a function of the temperature (only warm up test were analyzed).

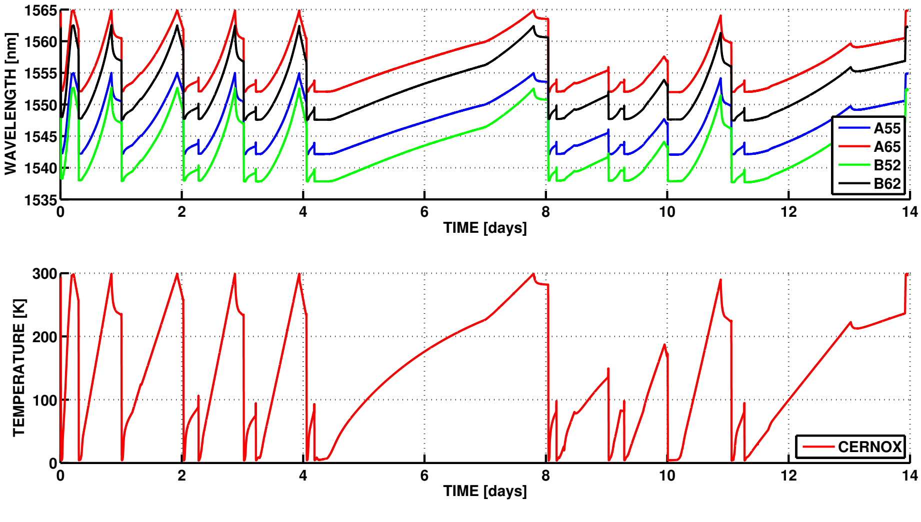

**Figure 3.19:** (top) Bragg wavelength of the FBG sensors vs. time. The blue and the red lines represent the epoxy-coated FBGs (A55 and A65), the green and the black line represents the PMMA-coated FBGs (B52 and B62). (bottom) Reference sensor temperature vs. time.

Epoxy-coated sensors present in general a smaller change of the Bragg wavelength compared to the PMMA-coated sensors within the range from 4 K to 300 K.

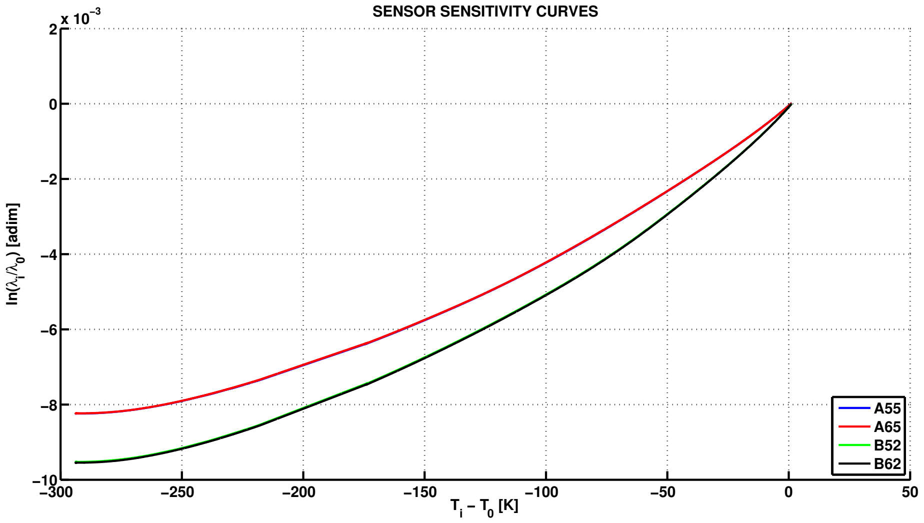

**(a)** Normalization to room temperature and reference Bragg wavelength of FBG sensors outputs vs. temperature (only warm-ups).

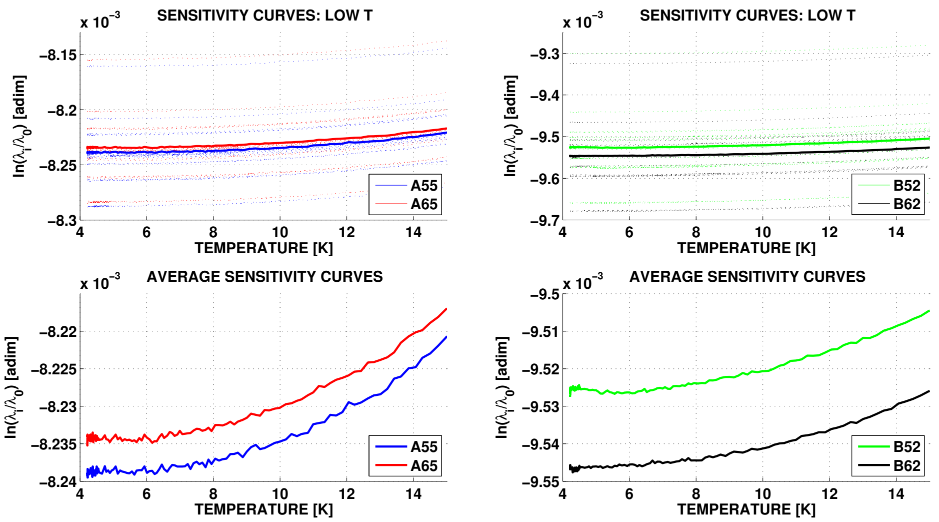

**(b)** Zoom plot for normalized sensor outputs from 4 K to 15 K. (top-left) Epoxy-coated sensors. All the warm-ups. (Top-right) PMMA-coated sensors. All the warm-ups. (Bottom-left) Epoxy-coated sensors. Average sensitivity curves. (Bottom-right) PMMA-coated sensors. Average sensitivity curves.

**Figure 3.20:** Sensitivity curves.

Figure 3.20b shows the normalized sensors outputs in the low temperature range. Figure 3.20b(top-left, top-right) reports the normalized sensors outputs, relative to the epoxy and PMMA coated sensors, respectively. All the thermal cycles are reported. Figure 3.20b(bottom-left, bottom-right) shows the values averaged among all the warming up cycles. The sensitivity of the FBG sensors decreases at low temperatures for both the polymers.

### 3.5.4 Sensor calibration

The sensors calibration was carried out by using the look-up table method discussed in the previous section. This procedure allows to reconstruct the cryogenic temperature measured by the FBG sensors. The results of the calibration are shown in Figure 3.21 and 3.22 for Epoxy-coatef FBG and PMMA-coated FBG respectively.

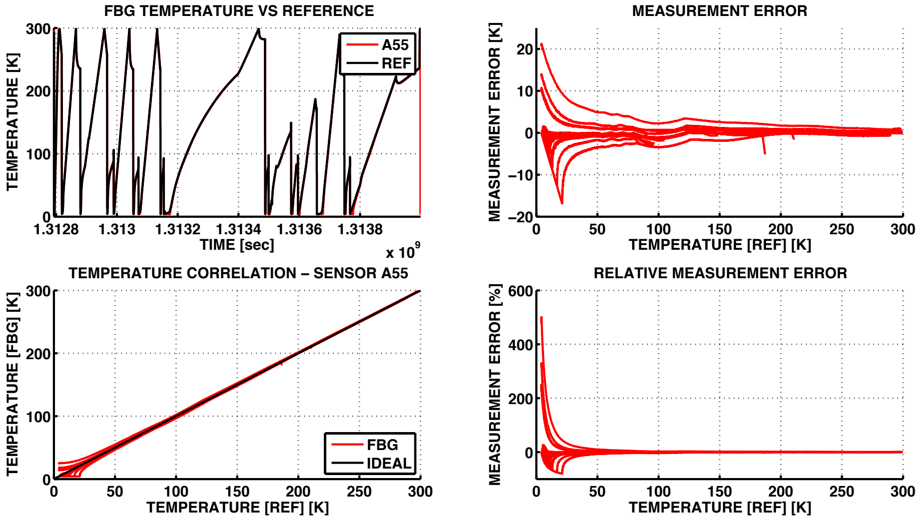

**Figure 3.21:** Temperature reconstruction and performance evaluation of Epoxy-coated FBG (type ”A”).

Figure 3.21 shows the performance of the type ”A” sensor (Epoxy-coated) in terms of temperature reconstruction from the normalized Bragg wavelength shift. In figure 3.21, the sub-plot at the top left shows a comparison between the temperature reconstruction from FBG sensor (red line) and the temperature measurement from Cernox (black line), the data confirmed that the FBG sensor reaches 4.2 K and show a good agreement between measurements. Unfortunately, it is possible to note that at low temperature (4.2 K - 15 K), in correspondence with the starting point of the warm-up stage or with the end of the cool-down, the error rate is high; this is explained by the different response time of the two sensors. In particular, it is seen that the FBG sensor responds more slowly to sharp changes of temperature as the epoxy resin has a lower thermal conductivity ($\lambda_{epoxy} \sim 0.24$ W/(K· m)) than the material which constitutes the Cernox sensor (Zirconium Oxy-Nitride).

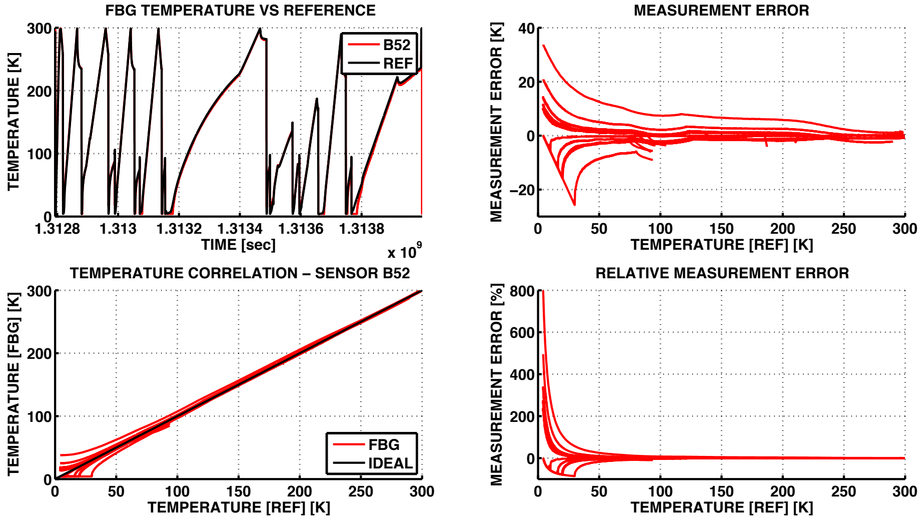

**Figure 3.22:** Temperature reconstruction and performance evaluation of PMMA-coated FBG (type ”B”).

Similar considerations can be made for the FBG sensor of type ”B”. There is a good agreement between the measurements performed with FBG and Cernox but the response time of the sensor FBG coated with PMMA are even greater with respect to the type ”A” response time. The thermal conductivity of PMMA is: $\lambda_{PMMA} \sim 0.19$ W/(K· m).

### 3.5.5 Conclusions

Two novel classes of cryogenic temperature FBG sensors have been manufactured, tested and calibrated. These sensors have been made by integrating a FBG with thermo-polymers able to generate strain due to thermal expansion. The sensors were tested at Cryolab (CERN) by using a cryostat filled with liquid helium (T = 4.2 K), 16 cryogenic cycles were carried out using a Cernox sensor as reference. The experimental results have shown that such sensors are able to perform temperature measurements, with a resolution of approximately 0.1 K, over the range from 4 K to 300 K. A delay of response was observed in both types of FBG sensors, specially at low temperature, due to both the low thermal conductivity of the polymers used as coating and its high thickness. Furthermore, it is seen that the FBG sensors in this configuration, can be used to measure the CTE of its coating [(79)] and thermal strain applied the metallic structures in cryogenic conditions [(80)].

# Chapter 4

# FBG Magnetic field sensors

This chapter proposes a novel magnetic field sensor that integrates the Terfenol-D (TbDyFe) magnetostrictive material with Fiber Bragg Grating (FBG) strain sensor. Nowadays, magnetic field measurement has become a fundamental procedure in many industrial and scientific applications and Fiber Bragg Grating based sensors are a winning choice in this area. The chapter first summarize the applicable techniques for measuring electric current (meaning also magnetic field) divided into non optical and optical ones. Successively, the novel device is presented and the basic features are reported. Because of hysteresis and nonlinear phenomena taking place in such materials, the sensor's performances may be sensibly reduced. Moreover, the dependence of the magnetostrictive response on the pre-stress has been used to improve and fit the performance of Terfenol-D based fiber Bragg grating magnetic sensor. The possibility to tune sensitivity allows to work at different operative conditions and to develop advanced sensors with reconfigurable sensitivity. Results are shown and discussed.

## 4.1 Introduction

Magnetic/current sensors have always gained great interest for several applications in which they could be successfully adopted ranging from the electrical power industry to the active control of structural vibrations in high precision machine-tools, to the micro-displacement in robotics, and, in general, in the construction of precision actuators in biomedical, aerospace, automotive fields and High Energy Physics. They are based on different physical technologies (Electromagnetic induction, Hall effect, superconductivity, magneto-resistance). Each of them has a specific application and, all together, can cover a large range of detection ( from few nanoTesla to several Tesla). In the next two sections a brief excursus of the main traditional techniques for magnetic sensing will be reported focusing on applications and drawbacks.

## 4.2 Non-optical sensing techniques

The only quantities that can directly be measured with conventional electrical methods are current and perhaps voltage. The other quantities are firstly converted to a current or a voltage that can in turn be measured. Even though the measurement seems to be simple in principle, it results complicated in practice. The main obstacles result the power dissipation in the measurement circuit and the need to keep the display unit at ground potential. The most-used device for measurements of alternating currents in electrical high and medium voltage networks is the CT (Current Transformer). A current transformer transforms the current down to a reasonable level and provides an isolation barrier between the primary winding at line potential and the secondary winding at ground potential. The primary current of the transformer is translated to the secondary current ($I_1 = n \cdot I_2$) by the turns ratio n and $I_2$ is measured by an amperometer or other conventional methods. These devices are reliable and have long life cycles but become very costly and massive with increasing voltages. Most current transformers consists of a ferromagnetic core enclosing the conductor. Measurement windings are wound around the core and a voltage is induced according to Faradays induction law. A drawback for this type of sensor is that it only be used for AC measurement. An example of current transformer is described in [(81)].
Another type of current sensor also based on Faradays induction law is the search-coil magnetometer [(82)]. It consists of an iron magnetic core and a coil wound around it. When the magnetic flux through the conductor changes, a voltage proportional to the rate of change is induced in the coil and can be measured between its leads. This sensor can measure fields over a very wide range from 1 pT to 1 kT in a frequency range of [1 Hz - 1 MHz]. Always according to the Faradays induction law only AC magnetic field can be detected even if rotating the coil in the field is possible to measure also

static fields. Another sensor based on the induction law is the Rogowski coil. It is a core less coil toroidally placed around a conductor forming a closed loop. When the current changes, a voltage proportional to the rate of this change is induced into the wound coil. This type of sensor can measure AC currents up to 100kA in a bandwidth from 0.1 Hz to 100 MHz showing good linearity without saturation in virtue the fact of the absence of a magnetic core. In order to overcome the obstacle to measure only AC currents more complex devices exploiting the Hall effect are used.

The Hall effect was discovered by Edwin H. Hall in 1879 and establish that when a current flows along the sheet of conducting material dipped in a magnetic field perpendicular to the surface, a potential difference (Hall voltage) is set up on the sides of the thin sheet [(82)].

Hall elements made of semiconductors have a much larger effect than those made of metallic conductors. Nowadays, Hall sensors are produced at low costs due to standard CMOS technologies and are mostly made of silicon or III-V semiconductors. They have good temperature characteristics, bandwidths from static fields up to 100 MHz, resolutions of 100 nT and a dynamic range from 50 $\mu$T to 30 T [(83)]. Another typology of sensors are magnetordiode, semiconductor diode where the p-region is separated from the n-region by an area of undoped silicon. Magnetodiodes have higher responses than Hall elements at similar bandwidths and resolutions up to 0.5 $\mu$T, but they suffer from a high temperature dependency [(84)]. Magnetoresistors are based on the MR (MagnetoResistance) effect [(82)]. This effect describes the relative change of resistance of a conductor at the presence of a magnetic field. According to the orientation of the magnetic field vector and the electric current vector, the effect is named either longitudinal MR effect (magnetic field and current parallel) or transversal MR effect (magnetic field and current perpendicular). Typically, magnetoresistors for field sensing have a dynamic range from B = 1 $\mu$T to B = 1 T, a resolution of 10 nT and a bandwidth from dc to 10 MHz [(83)]. Magnetoresistors do however, not give information about the direction of the field. The most sensitive magnetometer is, instead, the SQUID (Superconducting Quantum Interference Device), as superconductor magnetometer with a resolution of fT [(82)]. The SQUID is based on the Josephson effect that arises in superconducting rings with a *weak link*. Josephson discovered, that a current can flow through the weak link as an oscillating function of the magnetic field intensity. SQUIDs are very precise and expensive magnetic field sensors and need liquid Nitrogen cooling to allow superconductivity. They typically have a dynamic range from B = 1 pT to B = 0.1 mT, a resolution of 100 fT and a low bandwidth from dc to 5 Hz [(83)] and are therefore not suitable for current fault detection. The high sensitivity of SQUIDs allow them to be used in astronomy [(85)], geological [(86)], and medical applications [(87)]. All presented sensing non optical principles suffer from electromagnetic interference that is expected to be at a very high level in the application environment. Especially Lorentz force based sensors, such as Hall element, magnetodiode are sensitive to EMI due to their typically low signal levels. The same holds for the search-coil magnetometer. Costly high-precision magnetometers such as the SQUID are not suitable due to their cost, dynamic range and low bandwidth limitations.

## 4.3 Optical sensing techniques

In order to overcome the problems caused by electromagnetic interference on the sensor signal, optical signal transmission using optical fibers is the best solution for that purpose. Over the last 30 years, it has been recognized that optical current sensors have many advantages compared to conventional iron-core current transformers, including their immunity to electromagnetic interference, high dynamic range, bandwidth, compact design, especially reduced complexity, and cost of insulation construction [(88)], [(89)]. However the competition with mature technologies is very hard being the customers attracted to good performance with reasonable price devices. The most interesting magneto-optic effect in transmission for magnetic field sensing is the Faraday effect. The phenomenon was discovered in 1845 by Michael Faraday. When a beam of linearly polarized light is sent through a material exhibiting the Faraday effect previously placed in a magnetic field and the beam is in the direction of the field, a rotation of the plane of polarization of the light will occur, as depicted in Figure 4.1. The effect is non-reciprocal in nature. This means that when the direction of a light beam that passes twice through the medium in opposite directions will thus acquire a net rotation which is twice that of a single pass. In paramagnetic and diamagnetic materials the magnetization and, thus, also the polarization rotation is practically proportional to the magnetic field strength, H. One can then describe the rotation in terms of the Verdet constant, V:

$$\theta = \int_L V \cdot \hat{H} dl \tag{4.1}$$

where H is the component of the magnetic field strength parallel to the light propagation direction. (The Verdet constant is sometimes expressed in terms of the magnetic flux density, B, which for these materials is linearly related to the magnetic field strength, B=mH.).

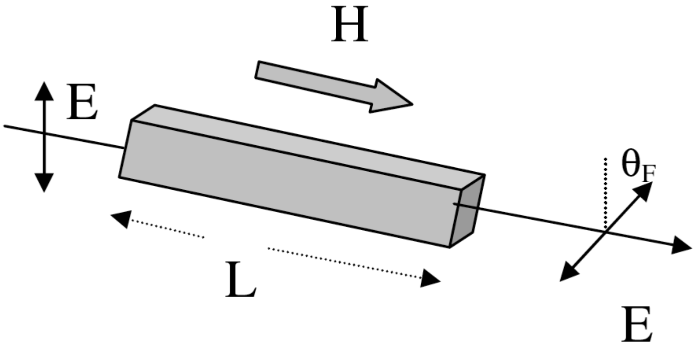

**Figure 4.1:** The Faraday effect.

A common magneto-optic material for field sensing is terbium gallium garnet, which has a Verdet constant of 0.5 min/(G cm). Along with a relatively high Verdet constant, this material also can take on a permanent magnetization. Because of this unique combination of magnetic characteristics, this material also has applications in magneto-optical memories. The unique advantage that the magneto-optical sensor has over other magnetic sensors is its very fast response time. Sensors with gigahertz response have been fabricated [(82)]. Unfortunately, due to the low value of the Verdet coefficient, they showed very low sensitivity.

### 4.3.1 Terfenol-D based Fiber Bragg Grating magnetic sensor

As reported in the previous section, in general, the common mechanism used to detect magnetic field with fiber optic sensors is Faraday effect, but due to the low value of the Verdet coefficient, they showed very low sensitivity. Therefore, different transducers have been employed in order to improve performances. The idea to integrate a magnetostrictive material with optical fiber strain sensors to detect weak magnetic fields, was proposed in [(90)]. In such early paper an optical fiber with a magnetostrictive jacket was considered in such a way to exploit both magnetostrictive (controlled by the field, through the material) and elasto-optic effect shown by the fiber. Later, in [(91)], such idea was successfully implemented. However, the sensitivity of the optical fiber based magnetic sensors can be considerably improved by using fiber Bragg gratings (FBGs). In last decades, moreover, a great interest has been devoted to the development of materials with strong magneto-elastic coupling (Terfenol-D and Ni-Mn-Ga alloys), [(92, 93)], and to devices employing them. Even if based on different physical behavior, they are able to strongly deform in response to a magnetic field. In particular, Terfenol-D shows strains up to thousands ppm, while Ni-Mn-Ga alloys can reach $10^5$ ppm but need much higher fields. The integration of such strongly coupled magneto-elastic materials to a FBG-based sensor could yield to a passive, small size, magnetic field sensor. Such idea has been recently developed and exploits a Terfenol-D alloy (generally a rod), as field-strain transducer, and a FBG strain sensor to measure the deformation due to magnetic field. The study and design of such devices have been tackled in several recent contribution, we cite in chronological order. In [(94)], the analysis of a current sensor was considered, while a device obtained by the coupling of a FBG with a magnetostrictive material has been proposed to reduce sensors temperature dependence, in [(95)]. In [(96)] a temperature compensated current sensors was analyzed. Liu et al. proposed in [(97)] the analysis of a new temperature-compensated field sensor where materials with different magnetostriction and the same thermal expansion coefficient were employed. In the same year, Satpathi et al. [(98)] described the development of a current transducer, employing FBG and Terfenol-D material; a similar paper by Mora et al., [(99)], proposed an AC current and temperature sensor. In particular, the latter applied a simple memoryless model relying the strain response to the field in order to extract the current measurement; conversely, in [(98)] magnetostriction phenomena has been analyzed with more detail. There, it was observed that magnetostriction is a unipolar phenomena with hysteresis. Such characteristics yielded, as well-known, [(100)], to supply the rod with a bias current, in order to circumvent the former problem, and to pre-stress the rod in order to obtain a more linear response of the sample. In any case, however, any hysteresis phenomena has been disregarded. Nevertheless, non negligible rate-independent memory effects (i.e. hysteresis), impact the performance of such a device and could represent a severe drawback for its development. However, recently, hysteresis modeling has seen great progress, [(101, 102)], resulting in suitable techniques to model hysteresis. All such assessed knowledge, yielded to the development of a novel magnetic sensor, based on the integration of fiber Bragg grating and magnetostrictive material (Terfenol-D), where hysteresis compensation is performed by proper algorithms. For the developed device, the FBG is used as strain sensor and the Terfenol-D as magnetic field transducer.

**Figure 4.2:** Picture of the FBG magnetic sensor: the black block is a magnetostrictive rod (Terfenol-D) on which is bonded a bare FBG. The sensor is placed in a pre-stress holder.

The device is built up by bonding FBG and magnetostrictive material together, as shown in Figure 4.2. Magnetic field deforms the magnetostrictive rod, which actuates the FBG bonded on it, so modifying its Bragg wavelength. In the present chapter the description of the device is provided. The features of the whole device are experimentally demonstrated through a wide number of measured data. An important element to be considered, when magnetostrictive materials are considered, is the dependence of their characteristic on applied mechanical loads (i.e. the applied pre-stress). In fact in dependence of the applied load, the magnetostrictive branches change their shape [(100)] and their slope, modifying the sensitivity for the sensor and the measurable range for magnetic field. Such dependence is usually disregarded, as the device is characterized to work at constant pre-stress level. Also in this chapter this dependence has been investigated in order to exploit it to optimize the design of sensor toward specific applications.

### 4.3.2 Experimental setup

The experimental setup, employed to develop the field sensor, is composed by an optoelectronic, a magnetic and a mechanical setup, that will be discussed in what follows.

**Optoelectronic setup**

The interrogation system used for the proposed magnetic sensor is passive and relies on a low cost technique based on optical filtering combined with broadband interrogation. In particular, the optoelectronic setup used for the proposed magnetic sensor relies on the following devices:

- n. 5 FBG, with a central wavelength $\lambda_B$ in the 1550 nm telecom band;
- superluminescent diode (SLED) source with 40nm FWHM bandwidth centered at 1550nm;
- photodiode as read-out element;
- DAQ.

After a suitable bonding protocol choice, followed to improve sensor performances, the fiber Bragg grating has been bonded with cyano-acrilate glue on the Terfenol sample oriented along the principal axis of the active element. The output voltage from photodiode was aquired by a DAQ and stored in a laptop equipped with a read-out software from National Instruments.

**Mechanical setup**

The sample of Terfenol-D magnetostrictive material, by ETREMA, on which the FBG is bonded, is a 20 mm rod with a 4.7 mm diameter. Variable pre-stress levels ranging from 15 cNm to 75 cNm were provided by a pre-stressing holder, specially designed for this application, applied by a torque wrench. There were considered the following pre-stress values: 0 cNm, 25 cNm and 50 cNm. There was used a swivel in order to align the sensor to the magnetic field:

- Y-axis: sensor placed vertically along the magnetic field direction;
- X-axis: sensor placed horizontally, perpendicularly to the magnetic field (90° rotation with respect to Y);
- Z-axis: sensor placed horizontally, perpendicularly to the magnetic field (90° rotation with respect to X).

Such device in connection to the optoelectronic setup, would allow a full mechanical characterization of the sample.

**Magnetic setup**

A 0.5 Tesla magnet was employed in order to test the devices. The magnetic field generated is controlled by the current supply in the range from 0 A to 350 A with step of 25 A or 50 A. The magnetic induction B was measured by a 3-axis Hall reference sensor.

### 4.3.3 Results and discussion

The experimental results are reported in Figures 4.3 and 4.4 for FBG1 and FBG2, respectively. For brevity of discussion, are shown only the results relating to the sensors FBG1 and FBG2 because the responses of FBG1, FBG3 and FBG5 are superimposable, while those of FBG2 and FBG4 differ from the previous ones for the response along the axes X and Y. The results can be summarized as follow:

- The response that we get when the sensors are placed along the Y-axis (with prestress other than 0) is always larger than those that occur along the other two axes. In the first case, there are variations of the output voltage of the order of V, while the latter have variations on the order of hundreds of mV.
- The response along the X and Z axes are always very close to each other.

- When the sensors are placed along the Y-axis without prestress, the power saturation is reached immediately due to the strong variations of the output voltage.
- Along the X and Z axes, without applying pre-stress, the sensor response is reversed. In particular, it seems that along the X-axis the sensors require a training cycle before having a steady response.
- By applying a prestress of 50 cNm, in general the sensors exhibit a lower hysteresis and improved linearity.

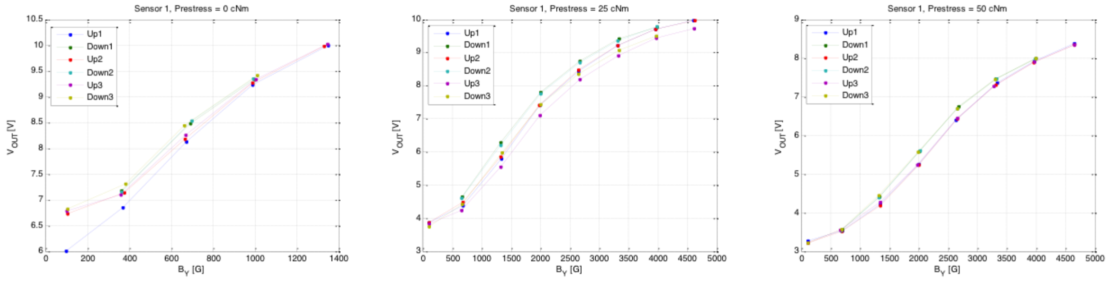

**(a)** Y-axis, 0 cNm. **(b)** Y-axis, 25 cNm. **(c)** Y-axis, 50 cNm.

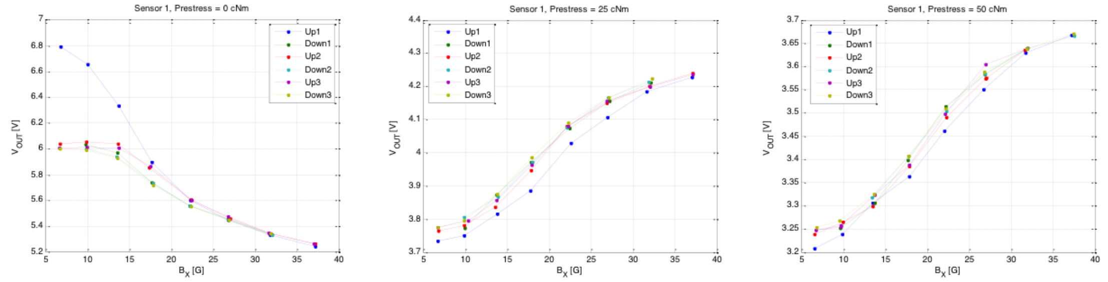

**(d)** X-axis, 0 cNm **(e)** X-axis, 25 cNm. **(f)** X-axis, 50 cNm.

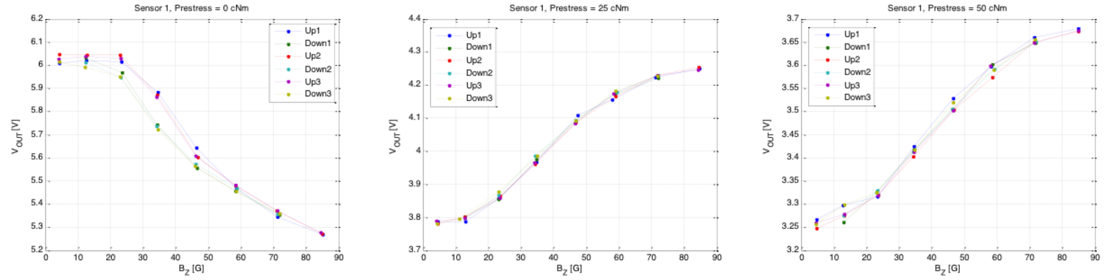

**(g)** Z-axis, 0 cNm. **(h)** Z-axis, 25 cNm. **(i)** Z-axis, 50 cNm.

**Figure 4.3:** Sensor 1 magnetic characterization.

As discussed in the previous bulleted list, the response of FBG2 and FBG4 along X and Z axes is strangely very different from the other sensors. In particular, the response has a quasi-Gaussian shape. Furthermore, with respect to the sensors FBG1, FBG3 and FBG5, the response dynamics along the Y axis is significantly lower (2000 vs. G. G 5000).

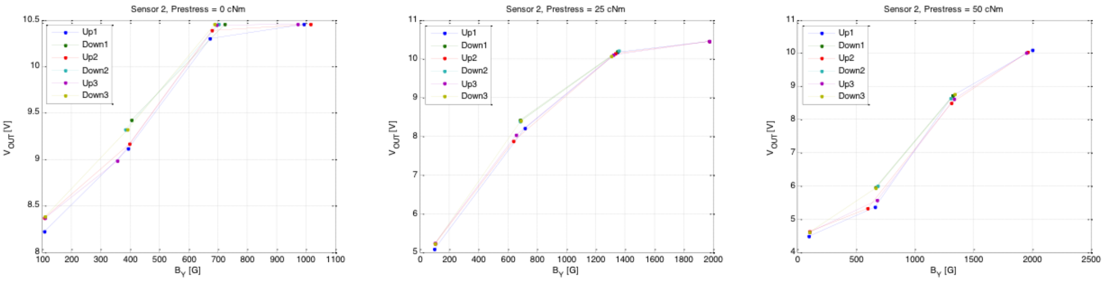

**(a)** Y-axis, 0 cNm. **(b)** Y-axis, 25 cNm. **(c)** Y-axis, 50 cNm.

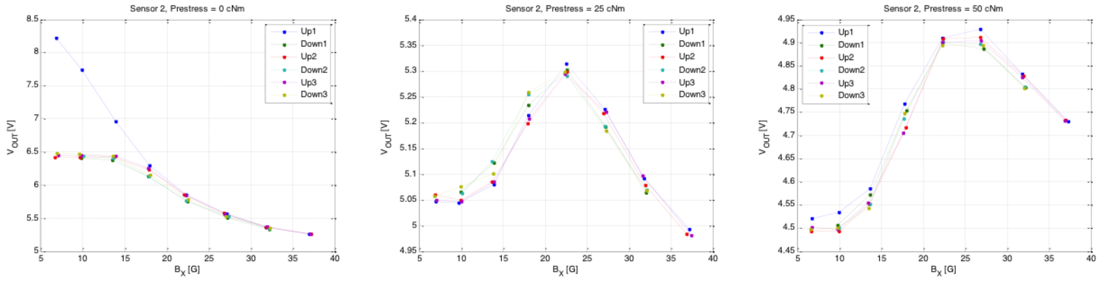

**(d)** X-axis, 0 cNm **(e)** X-axis, 25 cNm. **(f)** X-axis, 50 cNm.

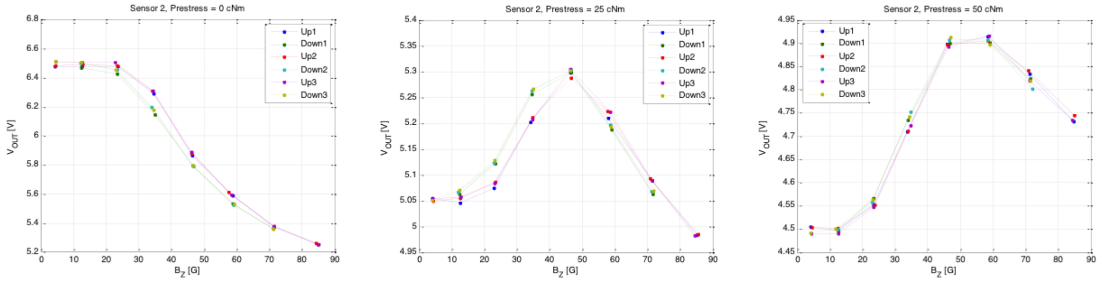

**(g)** Z-axis, 0 cNm. **(h)** Z-axis, 25 cNm. **(i)** Z-axis, 50 cNm.

**Figure 4.4:** Sensor 2 magnetic characterization.

## 4.4 Conclusions

Magnetic field sensors based on a FBG bonded on a magnetostrictive rod are developed and tested. The magnetic characterization shown a quite good sensing capability mainly along the Y axis (sensor placed vertically along the magnetic field direction). Magnetic saturation was observed for FBG1, FBG3 and FBG5 at B = 0.5 T, while for FBG2 and FBG4 at B= 0.2 T,. Hysteresis was been observed in all the magnetic cycles. These limitations suggest to study and develop a new configuration sensor-material able to cover an increased range of detection with lower hysteresis. The development activities of the sensors was conducted at the following institutions: Institute of Composite and Biomedical Materials of CNR, Naples; Engineering Department of the University of Sannio, Benevento; Electric and Information Technology Engineering Department of the University of Naples "Federico II". The testing of the sensors was carried out at the "Fermilab" at CERN in Geneva.

# Chapter 5

# Magnetic field sensor based on clad-etched FBG

In the previous chapter there was discussed of an interesting optoelectronic sensing device based on the magnetostrictive effect of some iron alloys. The cited limitations have led us to the need of developing a novel magnetic field sensor designed to have a wider dynamic and a greater sensitivity than the magnetostrictive sensor. In this chapter, a novel concept of magnetic sensor that uses magnetic fluid as sensitive element in which immerse a clad-etched FBG, is presented. In particular, the theoretical principles underlying the proposed technology will be exposed, then it is shown the implementation of a numerical model useful to assist the sensor design, finally the results were discussed.

## 5.1 Introduction

Magnetic field optical sensors are widely used in near-field measurement (when electric and magnetic components of EMF have to be separately estimated). Many of these sensors exploit magnetostrictive effect that produce a strain in a ferromagnetic material by rotation of the magnetizing direction of each magnetic domain of the material in the direction of the magnetic field (de Lacheisserie, Gignoux, & Schlenker, 2004). Sensors proposed in (Bucholtz and Udd, 1991; Bucholtz, Koo, Kersey, and Dandridge, 1987; Heaton, 1980; Kersey, Jackson, and Corke, 1985; Lee, 1995; Rashleigh, 1981; Yariv and Winsor, 1980) operate measuring the longitudinal strain induced in an optical fiber by a magnetostrictive jacket. As descrived in the previous section, the variation in length ($l$) of magnetostrictive material-coated optical fiber is given by

$$\frac{\delta l}{l} = C_{eff} H_{ext}^2 \tag{5.1}$$

where

$$C_{eff} = \frac{3\lambda_{av}}{2H_a^2}\left(\frac{R(\omega)}{(1 + A_f E_f / A_m E_m)(1 + N\chi)^2}\right) \tag{5.2}$$

and $H_{ext}$ is the external magnetic field, $\lambda_{av}$ is the magnetostrictive constant of material, $H_a$ is the anisotropy field, $R(\omega)$ is the response factor due to mechanical resonances, $A_m$ and $A_f$ are the cross-sections of fiber and jacket, $E_m$ and $E_f$ are Young modulus of fiber and jacket, $N$ is the demagnetization factor, $\chi$ is the susceptibility.
At present most research is based on bulk magnetostrictive materials [(96, 103, 104, 105)] and magneto-optical crystal [(106, 107, 108)], there are rarely investigations using FBG dipped in magnetic fluid as sensing element. It is reported that long-period fiber grating (LPFG) has a high wavelength shift [(109)] when immersed with magnetic fluid. However, LPFG is not easy for commercial application due to its broad full wavelength at half maximum (FWHM) which limits the measurement accuracy. It is also demonstrated magnetic fluid can be used to detect magnetic field by Faraday Effect [(110)], but this method is susceptible to the effect of light sources intensity. Recent advancement in the magnetic sensing, led to a novel conceptual class of magnetic sensors, based on the refractometric magneto-optical effect. In 2011 Jixiang et al. [(111)] developed and tested a clad-etched FBG magnetic sensor integrated with a magnetic fluid as sensing element.
As it is well known, the reflected wavelength ($\lambda_B$) of FBG has correlation with its effective refractive index ($n_{eff}$) and grating pitch ($\Lambda$) [(112)]. In general conditions, the $n_{eff}$ of FBG is not influenced by the external refractive index. However, if fiber cladding diameter is reduced along the grating region to certain extent, the $n_{eff}$ is significantly affected by external refractive index [(28)]. FBG refractive index sensors are based on the interactions between the fundamental mode and the external medium. From this result it follows that, in principle, it is possible to realize a magnetic sensors

by using a FBG as SRI sensor immersed in a magnetic fluid.

## 5.2 Review on Magnetic fluids

The interest in magnetic fluid arises from the fact that they exhibit rheological properties of fluids from the dynamic viewpoint, but can be controlled directly by the application of a magnetic field which can not happen with any natural fluid. Magnetic fluids are stable colloidal dispersions of ultra-fine (mostly) spherical ferro- or ferri-magnetic particles, such as magnetite ($Fe_3O_4$) or maghemite ($\gamma$-$Fe_2O_3$), in a nonmagnetic liquid carrier [(113)], which may be chosen to conform to a particular application. The most used magnetic fluid is based on an aqueous solution of $Fe_3O_4$ nanoparticles, prepared by the chemical co-precipitation method [(114)]. Its ion reaction is described in the following form:

$$Fe^{2+} + Fe3+ + 80H^{-} = Fe_3O_4 + H_2O$$

In the synthesis process, $Fe^{2+}$ is added in excess ratio to get stable $Fe_3O_4$ magnetic fluid with super paramagnetic characteristic [(115)]. The dispersion of the ferrophase is ensured by coating the nanoparticles with adequate surfactant (able to assure steric or electrostatic stabilization) [(116)]. Thus, the attraction forces between magnetic dipoles as well as the Van der Waals forces can be balanced while the tendency of precipitation in gravitational or magnetic field could also be compensated, the magnetic colloid stability being assured [(117)]. The magnetic properties of magnetite, that make it a desirable component of magnetic fluids, are derived from its crystal structure. Magnetite crystallizes in the inverse spinel structure [(118)], consisting of iron oxide ions in a cubic close-packed arrangement. The 1/4 of the octahedral holes are occupied by $Fe^{2+}$ ions while the $Fe^{3+}$ ions are equally divided between 1/8 of the tetrahedral holes and 1/4 of the octahedral holes; electron spins of $Fe^{3+}$ ions in octahedral holes are aligned anti-parallel to those in tetrahedral holes while the Fe2+ ions tend to align their spins parallel with those of $Fe^{3+}$ ions in adjacent octahedral sites, leading to a net magnetization.

The properties of magnetic fluids have been intensively studied due to their multiple applications [(119)], in both technical and life sciences. The behaviors of ferromagnetic particles in magnetic fluid are dependent on the external magnetic field, so the refractive index of magnetic fluid is shown to be magnetic field dependent [(120, 121, 122)]. The refractive index $n$ is expressed in the following equation [(109)]:

$$n = \sqrt{\epsilon_r} = \sqrt{1+\chi} \tag{5.3}$$

where $\epsilon_r$ is the dielectric constant and $\chi$ is the electric susceptibility. When the external magnetic field is perpendicular to the propagation direction of light,

$$\frac{\partial \chi}{\partial H} < 0 \tag{5.4}$$

Then the magnetic fluid refractive index will decrease when the magnetic field is increasing. Magnetite nanoparticles with superparamagnetic properties have great potential to achieve convenient properties for biomedical applications due to their biocompatibility, it is known that the human body contains around 3 g Fe within the proteins like ferritin, hemosiderin, transferritin and hemoglobin and, also that the iron oxides are gradually recycled naturally. Various synthesis methods, adequate for magnetic nanoparticle preparation have been described in literature, like chemical coprecipitation [(123)], sonochemical reactions [(124)], sol-gel [(125)], microwave heating [(126)], mechanochemical [(127)], micelle microemulsion [(128, 129)] or solvothermal reduction [(130)]. Compared to other methods, chemical routes have often been found as most convenient methods used for the production of high quality magnetic nanoparticles [(131)].

## 5.3 Clad-etched FBG as Surrounding Refractive Index (SRI) sensor

Magnetic optical sensors based on magnetic fluid are a promising technology and from few years, is the subject of much attention by several research groups. To date, very few papers are published on this topic. The most relevant work consist in the injection of magnetic fluid in hollow core fibers [(132)] in order to cause changes in the $n_{eff}$ by means of the external magnetic field. However, his approach is poorly applicable as it requires a sophisticated instrumentation for the injection of fluids into the fiber and, mainly, requires unreliable read-out methods based on the measurement of the transmitted optical power.

The sensing principle of the proposed device relies on the dependence of the clad-etched

FBG resonance on different effective refractive index which is caused by magnetic fluid setting in changing magnetic field. So the $\lambda_B$ of FBG has correspondence with the magnetic fields value. In standard optical fibers, effective refractive index is not influenced by the external one; thus, no sensitivity to the surrounding refractive index (SRI) is expected. However, if cladding diameter is reduced along the grating region, the effective refractive index is significantly affected by the SRI. Consequently, shifts in the Bragg wavelength combined with a modulation of the reflected amplitude, due to changes in the guiding properties, are expected. Differently from the common use of this class of sensors, such as for temperature and strain measurements, in this case, only the refractive index $n_{eff}$ is affected by measurand changes while the grating pitch is practically unchanged. This effect was used by Kumazaki et al. to realize an in fiber tunable filter [(133)].
Recently, thinned fiber Bragg gratings (ThFBGs) have been used to realize a refractive index sensor [(28)]. In this paper, a complete numerical and experimental analysis on the use of ThFBGs for refractive index measurements is presented. In particular, three layers model for the thinned optical fiber has been used to identify the dependence of the effective refractive index on the SRI. From these results, the dependence of the sensor sensitivity on the SRI in terms of wavelength shift has been analyzed. Sensor fabrication has been carried out by using standard SMF-28 optical fibers and wet chemical etching in a buffered hydrofluoric acid (HF) solution. Finally, experimental characterization of the sensor response to external refractive indices varying in the range 1.3331.450 has been carried out by using broadband interrogation and a commercial optical spectrum analyzer. Finally, a novel approach based on the selective etching of the grating region has been presented and analyzed. In particular, the spectral changes in the grating response due variation of the SRI have been investigated leading to new sensing configurations [(27)].

## 5.4 Modeling and Simulation of a SRI FBG-based sensor

In order to realize a SRI sensor based on a FBG, it must be consider and define two important aspects: 1) the SRI sensitivity range; 2) the etching depth. These two parameters are antagonistic: to maximize the sensor sensitivity it must be maximized the etching depth which can compromise the structural integrity of the FBG. To assist the design of a SRI FBG-based sensor, it can be useful to model and simulate the sensor behavior in a proper software ambient.

An important activity carried out during the PhD course, has concerned the development of a multi-physics simulation tool for in-fiber sensing devices. In particular, the developed simulation tool, useful for any in-fiber grating device (Fiber Bragg Grating and Long Period Fiber Grating), has been developed in Matlab and linked to Comsol Multiphysics, a powerful multi-physics simulator based on the finite element method (FEM).

Being well-known the sensing principles for strain and temperature, which depend directly on the grating period $\Lambda$ and the effective refractive index $n_{eff}$, it is interesting to study the dependence between the refractive index of a surrounding medium and the spectral response of the grating. As described in the first chapter, the effective refractive index of a fiber grating is strictly linked to the propagation properties of the fundamental mode along the grating region. A way to engineer the spectral response of a fiber grating is to modulate the effective refractive index of the grating. In a single-mode optical fiber, the diameter of the fiber core is 9 $\mu m$ and the cladding diameter is 125 $\mu m$. The electric field which propagates in the fiber core, is weakly affected by what happens in the cladding but, by appropriately thinning the cladding, the effective refractive index of the grating will be affected by the changes in the refractive index of the surrounding medium (Evanescent Wave Effect).

To fully exploit this interesting feature of the fiber grating sensors, it is necessary to dispose of a tool capable to simulate the physical phenomena due to the changes in Surrounding Refractive Index (SRI) for a clad-etched grating. From these considerations, we proceeded to define a mathematical model for a fiber Bragg grating sensor.

### 5.4.1 Definition of the mathematical model

In the first chapter the theoretical fundamentals of the fiber Bragg gratings were introduced. The discussion, based on the Coupled Mode Theory (CMT), can be summarized as follows: by means of the Maxwell equations and the modal expansion, the effect of the presence of a dielectric grating was analyzed with the non-perturbative approach; then, by assuming that the interaction of the fundamental mode with an identical counter-propagating mode, we obtained a set of coupled differential equations. These allow closed form solution when the grating is uniform. As seen in the first chapter chapter, by applying proper boundary conditions and solving we obtain the following expression:

$$R = \frac{\sinh^2\left(\sqrt{(k^2-\hat{\sigma}^2)}L\right)}{\cosh^2\left(\sqrt{(k^2-\hat{\sigma}^2)}L\right)-\frac{\hat{\sigma}^2}{k^2}} \tag{5.5}$$

where, L is the grating length, $k = \frac{\pi}{\lambda}\nu\Delta n_{eff}$ is the alternative coupling constant, $\hat{\sigma} = \delta + \sigma$ is the continuous coupling constrant, $\delta = 2\pi n_{eff}\left(\frac{1}{\lambda} - \frac{1}{\lambda_B}\right)$ is the detuning, $\lambda_B = 2n_{eff}\Lambda$ is the Bragg wavelength which is linked to $\sigma$ as follow:

$$\sigma = \frac{2\pi}{\lambda}\Delta n_{eff}$$

$\Delta n_{eff} \simeq \Delta n$ depends on both the amplitude of the sinusoidal perturbation and the refractive index of the fiber core. The effective refractive index $n_{eff}$ depends on the physical and geometrical properties of core and cladding and also on the SRI if the cladding is thinned.

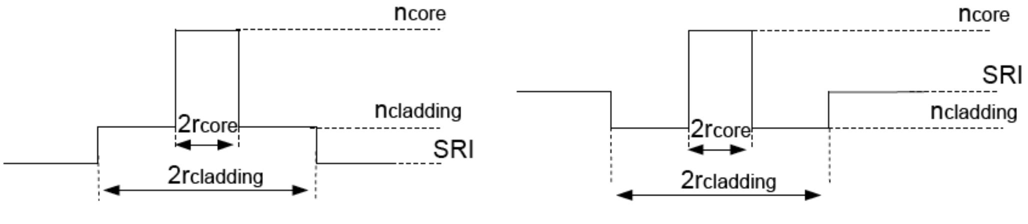

**Figure 5.1:** Refractive index variation along a cross section of a double cladding and weakly guiding fiber.

The dependence of the effective refractive index on cladding diameter and on SRI was evaluated by numerically resolving the dispersion equation of the doubly cladding fiber mathematical model [(134, 135)], massively used to study the radiation loss. In this model, the cross-section of the fiber is composed by three different domains: core, cladding and surrounding (assumed to be infinitely extended). A schematic of the simulated structure is shown in Figure 5.1: A weakly guiding fiber with a core radius

$r_{core}$ and a refractive index $n_{core}$, the inner cladding with radius $r_{cladding}$ and a refractive index $n_{cladding}$, the SRI (outer cladding) has been indicated with $n_{SRI}$.
It has been assumed and $\Delta n = n_{core} - n_{cladding}$ and $\Delta n' = n_{cladding} - n_{SRI}$. Note that can be positive or negative, as in Figure 5.1 (left, right), respectively. However, for the mathematical guiding condition the propagation constant $\beta = k_0 n_{eff}$ must be greater than $k_0 n_{SRI}$, where $k_0$ is the vacuum wave number. This is only the mathematical cut-off condition, but practically the $\mathrm{LP}_{01}$ mode is physically guided whatever is $\Delta n'$, if $b/a$ is sufficiently large. The dispersion equation is given by imposing the continuity of the transverse components of the electrical and magnetic fields at the interfaces between core and inner cladding and between inner cladding and outer medium. This leads to a system of four equations with four unknown magnitudes. To ensure a nontrivial solution, the determinant of (4 × 4) coefficients matrix must be equal to zero. For a doubly-clad fiber, the dispersion equation is given by [(134)]: for $\beta < k_0 n_{cladding}$

$$\frac{[\hat{J}_m(u) - \hat{Y}_m(u'c)][\hat{K}_m(v) - \hat{J}_m(u')]}{[\hat{J}_m(u) - \hat{J}_m(u'c)][\hat{K}_m(v) - \hat{Y}_m(u')]} = \frac{J_{m+1}(u'c)Y_{m+1}(u')}{J_{m+1}(u')Y_{m+1}(u'c)} \tag{5.6}$$

and for $\beta > k_0 n_{cladding}$

$$\frac{[\hat{J}_m(u) - \hat{K}_m(v'c)][\hat{K}_m(v) - \hat{I}_m(v')]}{[\hat{J}_m(u) - \hat{I}_m(v'c)][\hat{K}_m(v) - \hat{K}_m(v')]} = \frac{I_{m+1}(v'c)K_{m+1}(v')}{I_{m+1}(v')K_{m+1}(v'c)} \tag{5.7}$$

where

$$\hat{Z}_m(x) = \frac{Z_m(x)}{xZ_{m+1}(x)}$$

(Z representing the Bessel function $J$, $Y$, $I$ or $K$)

$$c = \frac{a}{b}$$

and

$$u = a\sqrt{k_0^2 n_{core}^2 - \beta^2}$$
$$u' = b\sqrt{k_0^2 n_{cladding}^2 - \beta^2}$$
$$v = b\sqrt{\beta^2 - k_0^2 n_{cladding}^2}$$
$$v' = b\sqrt{\beta^2 - k_0^2 n_{SRI}^2}$$

### 5.4.2 Numerical simulation and results

The mathematical model described in the previous paragraph was implemented in Matlab and numerically analyzed, in order to calculate the evanescent field distributions, by using a powerful finite element simulator, commercially named Comsol Multiphysics. The parameters of the optical fiber for the numerical analysis have been chosen according with SMF-28 standard: core diameter of 8.3 $\mu m$, original cladding diameter 125 $\mu m$, core refractive index of 1.4600, refractive index difference of $\Delta n = 0.36\%$, and effective refractive index of 1.4588 at an operating wavelength of 1550 nm. The model is graphically represented in Figure 5.2.

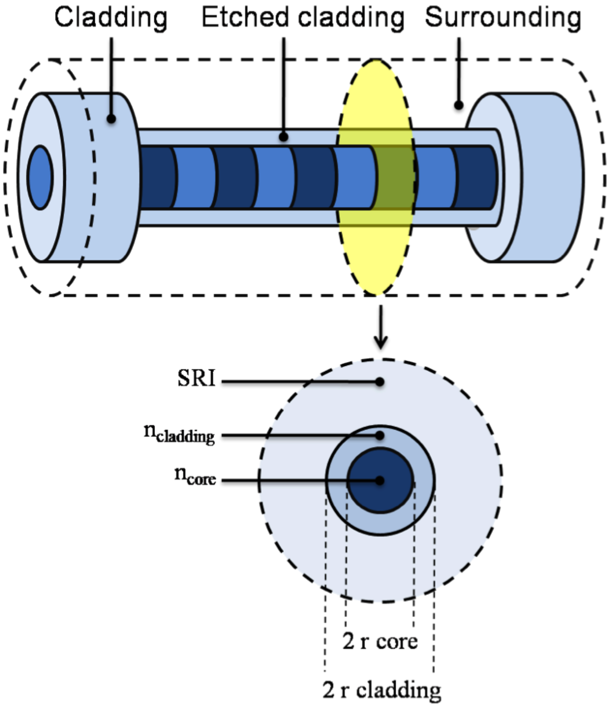

**Figure 5.2:** Schematic of a clad-etched Fiber Bragg grating.

The tool developed, allows to analyze the dynamic behavior of a clad-etched FBG sensor, for fixed values of $r_{clad}$ and $n_{SRI}$. In the detail, the Matlab code implements the numerical model of the FBG and the functions to handle the FEM simulations in Comsol. Moreover, it was necessary to implement a Matlab function able to create a live-link and run the Comsol through Matlab. This tool allows a preliminary assessment of the sensor performance and perform a sensitivity tuning ahead of the fabrication of the device [(136)].

The FEM simulator is entrusted with the task of calculating the evanescent field distributions at the boundary core-cladding. Figure 5.3 shows the field distribution for different values of $r_{clad}$ and $SRI$.

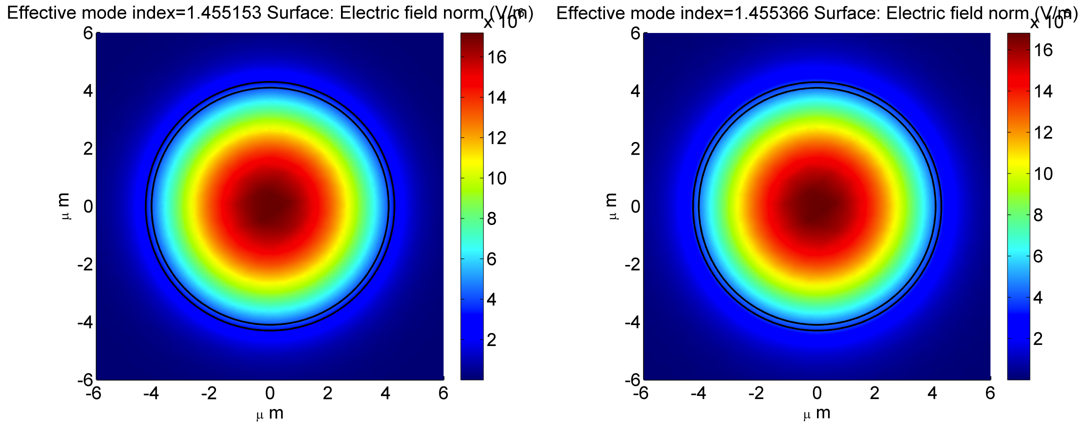

**(a)** SRI = 1.42 **(b)** SRI = 1.43

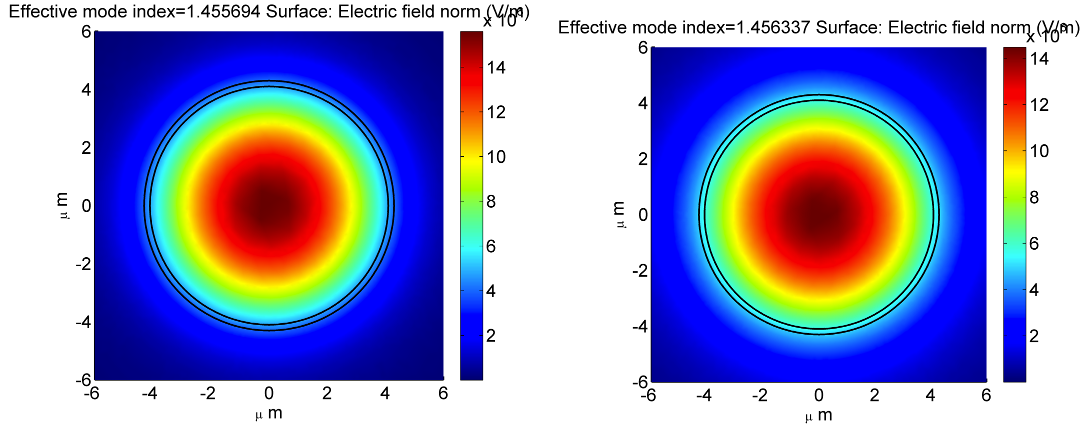

**(c)** SRI = 1.44 **(d)** SRI = 1.45

**Figure 5.3:** Simulation of the Electric field distribution on the interface core/cladding for a fixed value of the cladding radius ($r_{clad} = 4.3\mu m$).

Figure 5.4 shows the nonlinear behavior of versus the SRI for different cladding diameters in the case of uniform etching. In the same plot, the induced Bragg wavelength shift, evaluated according to the following expression simply derived from $\lambda_B = 2n_{eff}\Lambda$, is reported

$$\frac{\Delta\lambda_B}{\lambda_B} = \frac{\Delta n_{eff}}{n_{eff}} \tag{5.8}$$

Here, the full etching curve is referred to a completely removed cladding and $r_{clad}$ is the cladding radius.

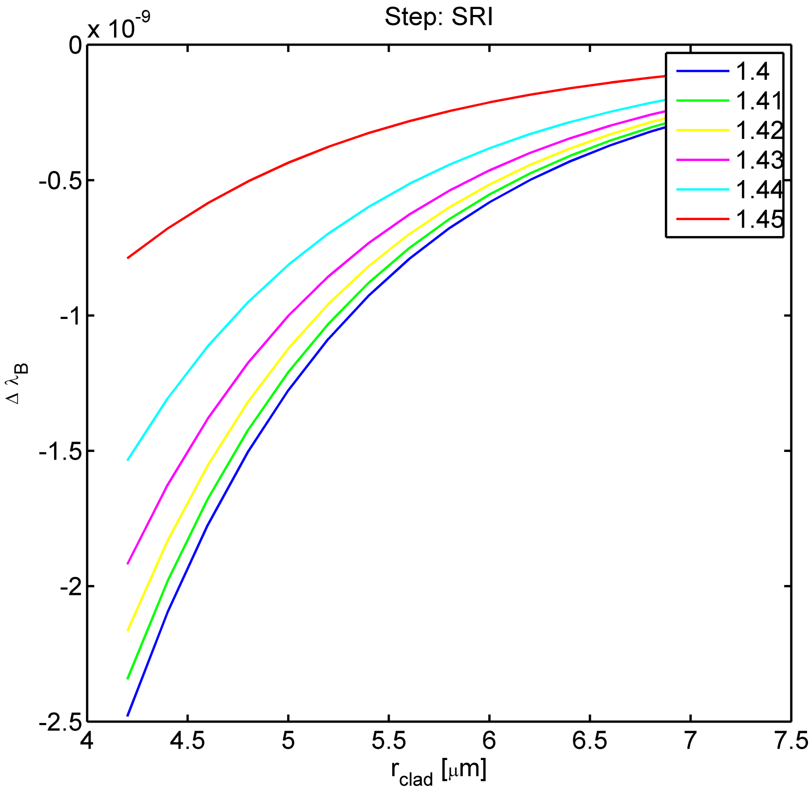

**Figure 5.4:** Bragg wavelength as a function of the cladding radius, for different outer medium refractive index ($SRI$).

Since the principle of operation relies on the interaction between the evanescent wave of the fundamental guided mode and the surrounding medium, it is obvious to expect that the effective refractive index variations, and, then, the Bragg wavelength shift increase as cladding diameter is reduced. In particular, for SRI around 1.330, the guided mode is well confined in the core region, leading to a weak evanescent wave and, thus, to a low dependence of the wavelength shift on the outer medium refractive index. As SRI increases, higher wavelength shift is observed, since the fundamental mode is less confined in the core region leading to a higher evanescent field and, thus, to a more efficient interaction with the surrounding medium. It is worth noting that such interaction and, as a consequence, the Bragg wavelength shift can be considered relevant if cladding diameter is reduced under 20 m.

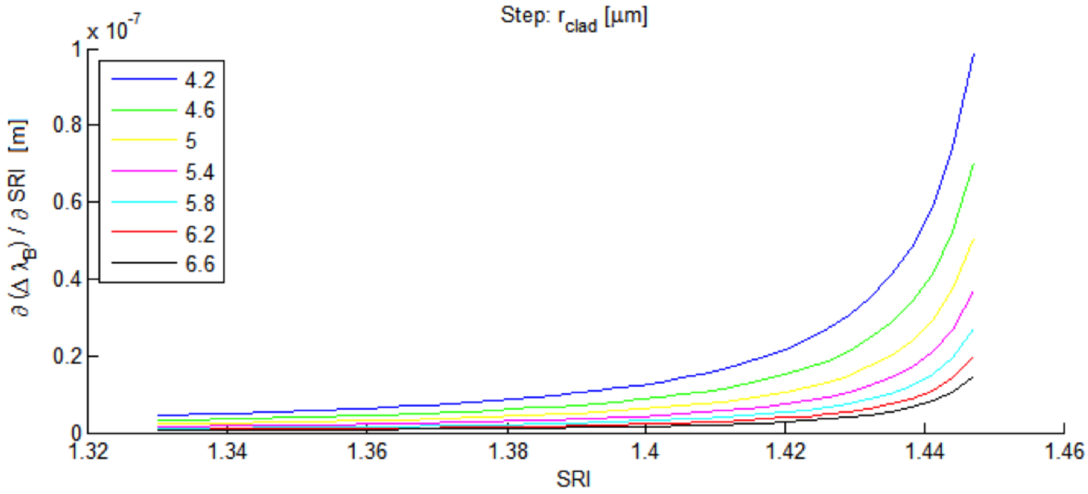

**Figure 5.5:** Sensor sensitivity as function of the refractive index of the outer medium ($SRI$) plotted for different cladding radius.

Figure 5.5 shows the sensor sensitivity in terms of $\partial\lambda_B/\partial SRI$ versus the SRI for several cladding diameters. As expected from above analysis, the sensitivity is an increasing function of the external medium refractive index reaching its maximum in the case of full-etching ($r_{clad} = 4.2\mu m$).

## 5.5 Sensor fabrication

The sensor fabrication has involved a detailed design phase for a sensor holder capable to host the sensor both during the clad-etching stage and in the sensing operation.

The ideal holder must have the following features:

- hydrofluoric acid (HF) resistant;
- no metallic parts;
- lightness;
- small size;
- ease of integration with optical fiber.

It was decided to realize a Teflon holder since it is highly resistant to HF, non metallic, light weight, and has a low friction coefficient. By using Catia, a 3D mechanical CAD, the sensor holder was designed paying much attention to optimize it for the two functionalities which are demanded. Figure 5.6 reports some 3D representation of our holder.

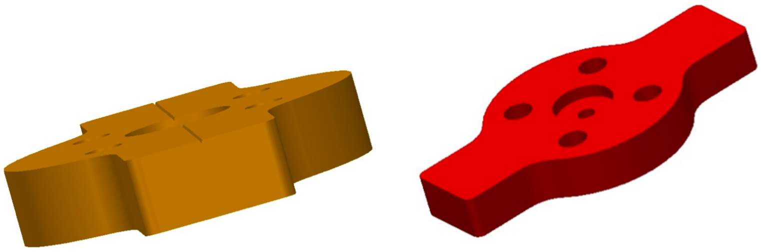

**(a)** Base layer: lateral view.

**(b)** Middle layer: down-side view.

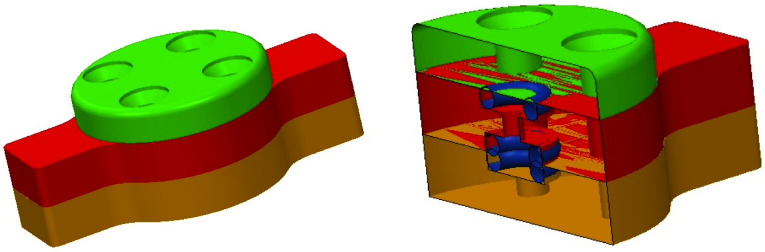

**(c)** The 3-layer holder assembled.

**(d)** 3D cross section view.

**Figure 5.6:** 3D CAD of the magnetic sensor holder.

The holder is characterized by three functional layers. The first layer (40 x 14 x 3 mm) has a longitudinal groove to hold the fiber and a small tank ($\phi = 4$ mm, depth = 1.5 mm) in the middle to inject the HF (during the etching) or the magnetic fluid (during the operation). The second layer (40 x 14 x 3 mm) helps to fix the fiber on the base layer and allows to create a closed tank fillable through a hole in its upper side. The third layer ($\phi = 14$ mm) is designed as tank cover. The sensor holder has been realized by means of a high-precision milling machine; have been employed n. 6 nylon screws for the mounting of the layers, and n. 3 silicon o-rings to prevent liquid leakage from the inner tank. Figure 5.7 report some pictures of the realized holder.

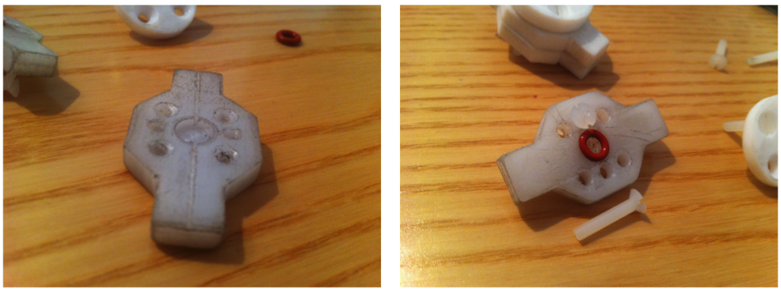

**(a)** Base layer: the groove and the inner tank are clearly visible.

**(b)** Middle layer: silicon o-ring and nylon screws are fixed to it..

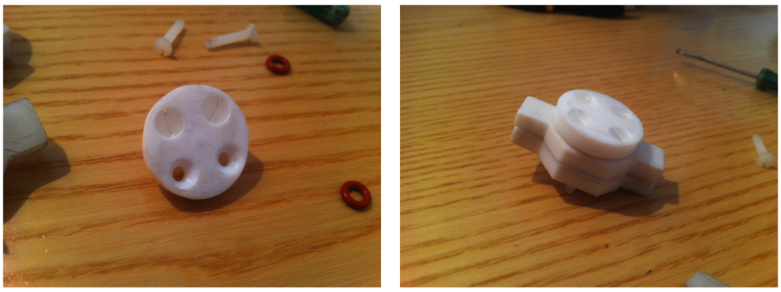

**(c)** Cover layer.

**(d)** The 3-layer holder assemled with nylon screws.

**Figure 5.7:** Pictures of the magnetic sensor holder.

## 5.6 Conclusions

A novel sensor for the detection of magnetic fields has been proposed. Starting from the integration of a magneto-optical nanoparticles fluid to a FBG surrounding refractive index sensor, it exploits the changes in the refractive index of the magnetic fluid which depends indirectly on the applied magnetic field. After a brief dissertation on the magnetic fluid properties, the design of the sensor was carried out by using a finite element simulator, which has shown interesting results in terms of range of detectability and sensitivity. Moreover, the sensitivity and ranges can be tuned by adjusting the etching depth (cladding diameter). The sensor design has involved the design of a proper holder to fix the fiber and keep it safe during the operation.

Unfortunately, there are no reports on the results of the experimental testing because, at the time, the sensor is still under fabrication. However, the simulation results are very encouraging and have allowed us to precisely define the physical and geometrical properties of the sensor and to arouse the interest of some industrial actors, particularly attracted by the promising applications of these sensors.

# Conclusions

In this thesis, the fundamental aspects of fiber Bragg gratings sensors were examined: from the formation of their particular spectral response to the fabrication methods, and also from the multiplexing of FBGs to the opportunity for temperature and strain sensing.
The exhaustive studies conducted, allowed to make possible the implementation of an important FBG-based temperature sensing system capable to operate under the harsh environmental conditions of CERN, which contributed to considerably reduce both the physical size in comparison with the classical electronic sensing systems, and eliminate malfunctioning due to the strong radiations and EM interference.

The research work presented in the third chapter, represents an interesting extension of the temperature sensing system, intended to operate along the cooling systems of the LHC in which the operative temperature can reaches 4.2 K (Liquid Helium $^3$He) or 1.9 K (Superfluid Helium $^4$He). The developed sensing devices demonstrate good performance and a high flexibility of operation. In particular, the coated FBG represents a great improvement of the state-of-art and they constitute a very promising class of sensors for such kind of applications.

Great importance has been given to the development of FBG-based magnetic field sensors, in particular, the work on this topic interested first the development of FBG sensors integrated with magnetostrictive material. The magnetostrictive FBG sensors have been demonstrated to work well under static magnetic fields up to 0.5 Tesla. Moreover, due to the hysteresis and the small range of detection, this sensing approach is no longer been deepened and the attention was focused on most promising sensing techniques.

The magneto-optic properties of some ferri/ferromagnetic material has attracted our attention and ispired us to analyze, first, and develop a magnetic field sensor based on the integration with a magnetic fluid and a FBG sensor. We found that Magnetite $Fe_3O_4$ nanoparticles magnetic fluid changes its refractive index as a function of an external magnetic field. This activities has involved the development of a finite element simulator to design a evanescent wave FBG sensor, able to detect the changes in refractive index of a surrounding medium. The numerical results, from the FEM model, encouraged the development of this kind of sensor and supported our ideas. At present, the prototype "0" is under construction.

# References

[1] D. Gloge. **Weakly Guiding Fibers**. *Applied Optics*, **10**(10), 1971. 5, 27

[2] R. Kashyap. **Fiber Bragg Gratings**. *Second Edition, Academic Press*, 2009. 6

[3] D. Marcuse. **Theory of Dielectric Optical Waveguides**. *Academic Press*, 1974. 6

[4] A. Cutolo. **Optoelettronica**. *Academic Press*, 1997. 9

[5] K. O. Hill, Y. Frujii, D. C. Johnson, and B. S. Kawasaky. **Photosensitivity in Optical Fiber Waveguides: Applications to Reflection filter fabrication**. *Applied Physics Letters*, **32**:647, 1978. 20

[6] G. Meltz, W. W. Morey, and W. H. Glam. **Formation of Bragg Grating in Optical fibers by a transverse holographic method**. *Optics Letters*, **14**:823, 1989. 21

[7] D. Lam and B. Garside. **Characterization of Single Mode Optical fibers**. *Applied Optics*, **20**:440, 1981. 21

[8] K. O. Hill and G. Meltz. **Fiber Bragg Grating Technology Fundamentals and Overview**. *Journal of Lightwave Technology*, **15**:1263, 1997. 21

[9] A. Yariv. **Coupled-mode theory for guided-wave optics**. *IEEE Journal of Quantum Electronics*, **9**:919, 1973. 22

[10] T. Erdogan. **Fiber Grating spectra**. *Journal of Lightwave Technology*, **15**:1277, 1997. 22

[11] P. J. Lemaire, R. M. Atkins, V. Mizrahi, K. L. Walker, K. S. Kranz, and W. A. Reed. **High pressure H2 loading as a technique for achieving ultrahigh UV photosensitivity and thermal sensitivity in GeO2 doped optical fibers**. *Electronics Letters*, **29**:1191, 1993. 23

[12] K. O. Hill, B. Malo, F. Bilodeau, D.C. Johnson, and J. Albert. **Bragg Gratings Fabricated in Monomode Photosensitive Optical fibers by UV exposure through a Phase Mask**. *Applied Physical Letters*, **62**:1035, 1993. 23

[13] A. Othonos and Xavier Lee. **Novel and Improved Methods of Writing Bragg gratings with Phase Mask**. *IEEE Photonics Technology Letters*, **7**:1183, 1995. 24

[14] B. Malo, S. Theriault, D. C. Johnson, F. Bilodeau, J. Albert, and K. O.Hill. **Apodised in-fiber Bragg grating reflectors photoimprinted using a phase mask**. *Electronics Letters*, **31**:223, 1995. 25

[15] J. E. Sipe, L. Poladian, and C. M. de Sterke. **Propagation through nonuniform grating structures**. *Journal of Optic Society of America A*, **11**:1307, 1994. 25

[16] T. Erdogan and J. E. Sipe. **Tilted fiber phase gratings**. *Journal of Optic Society of America A*, **13**:296, 1996. 25

[17] A. M. Vengsarkar, P. J. Lemaire, J. B. Judkins, V. Bhatia, T. Erdogan, and J. E. Sipe. **Long-period fiber gratings as band-rejection filters**. *Journal of Lightwave Technology*, **14**:58, 1996. 25

[18] W. H. Loh and R. I. Laming. **1.55 $\mu m$ phase-shifted distributed feedback fiber laser**. *Electronics Letters*, **31**:1440, 1995. 25

[19] B. J. Eggleton, P. A. Krug, L. Poladian, and F. Ouellette. **Long periodic superstructure Bragg gratings in optical fibers**. *Electronic Letters*, **30**:1620, 1994. 25

[20] T. Erdogan. **Cladding-mode resonances in short and long period fiber grating filters**. *Journal of Optical Society of America A*, **14**:1760, 1997. 25

[21] R. M. Measures. *Structural monitoring with fiber optic Technology.* Academic Press, London, 2001. 26, 29, 32

[22] S. M. Melle, K. Liu, and R. Measures. **A passive wavelength demodulation system for guided-wave Bragg grating sensors**. *IEEE Photonics Technology Letters*, **4**:516, 1992. 26

[23] P. St. J. Russel and J. L. Archambault. *Fiber Gratings in Optical Fiber Sensors, B.* Culshaw and J. Dakin Eds., Artech House, 1997. 26

[24] A. D. Kersey, M. A. Davis, H. J. Patrick, M. LeBlanc, C. G. Askins K. P. Koo, M. A. Putnam, and E. J. Friebele. **Fiber Grating Sensors**. *Journal of Lightwave Technology*, **15**:1442, 1997. 26, 31

[25] R.Kashyap. *Fiber Bragg Gratings.* Academic Press, second edition. 26, 31

[26] A. Mendez. **Fiber Bragg grating sensors: a market overview**. *Proceedings of SPIE*, (6619), 2007. 26

[27] A. Iadicicco, A. Cusano, S. Campopiano, A. Cutolo, and M. Giordano. *IEEE Sensors Journal.* 28, 109

[28] A. Iadicicco, A. Cusano, A. Cutolo, R. Bernini, and M. Giordano. **Thinned Fiber Bragg Gratings as High Sensitivity Refractive Index Sensor**. *IEEE Photonics Technology Letters*, **16**, 2004. 28, 106, 109

[29] Zhi Zhou and Jinping Ou. **Development of FBG sensors for structural health monitoring in civil infrastructure**. 29

[30] **http://www.micronoptics.com/sensing.htm**. 30

[31] **http://www.hbm.com/**. 30

[32] A. Csipkes, S. Ferguson, T.W. Graver, T. C. Haber, A. Mndez, and J. W. Miller. **The maturing of optical sensing technology for commercial applications**. *Micron Optics Inc., 1852 Century Place, Atlanta, Georgia 30345 (USA)*. 31

[33] B. Culshaw and J. Dakin. *Optical Fiber Sensors: Principle and Components*. Artech House inc., Norwood, 1988. 32

[34] E. Udd. **Fiber Optic Sensors: An Introduction for Engineerings and Scientists**. 1991. 32

[35] B. Culshaw and J. Dakin. *Optical Fiber Sensors: Applications, analysis, and future Trends*. Artech House inc., Norwood, 1997. 32

[36] B. Culshaw and J. Dakin. *Optical fiber Sensors: components and subsystems*, **3**. Artech House inc., Norwood, 1996. 32

[37] E. Udd. *Fiber Optic Smart Structures*. John Wiley and Sons, New York, 1995. 32

[38] A. Fernandez Fernandez andF. Berghmans, A. Fern, Ez Fern, M. Decreton, P. Megret, M. Blondel, A. Delchambre, Ez A, F. Berghmans A, B. Brichard, and M. Van Uffelen. **Radiation Hardness of Passive Fibre Optic Components for the Future Thermonuclear Fusion Reactor Instrumentation Links**. 2001. 33

[39] A.I. Gusarov, D.S.Starodubov, F. Berghmans, O. Deparis, A. Fernandez Fernandez Y.Defosse, M. Decreton, P. Megret, and M. Blondel. **Comparative study of MGy dose level g-radiation effect on FBGs written in different fibres**. *Optical Fiber Sensors*, **13**, 1999. 33

[40] A. I. Gusarov, F. Berghmans, O. Deparis, A. Fernandez Fernandez, Y. Defosse, P. Megret, M. Decreton, , and M. Blondel. **High Total Dose Radiation Effects on Temperature Sensing Fiber Bragg Gratings**. *IEEE Photonics Technology Letters*, **11**(9):1159–1161, 1999. 33

[41] A. Gusarov, C. Chojetzki, I. Mckenzie, H. Thienpont, , and F. Berghmans. **Effect of the Fiber Coating on the Radiation Sensitivity of Type I FBGs**. *IEEE Photonics Technology Letters*, **20**(21):1802–1805, 2008. 33

[42] F. Berghmans, A. Fernandez Fernandez, B. Brichard, F. Vos, M. Decreton, A. Gusarov, O. Deparis, P. Megret, and M. Blondel. **Radiation hardness of fiber-optic sensors for monitoring and remote handling applications in nuclear environments**. *SPIE International Symposium on Industrial Environmental Monitors and Biosensors Harsh Environment Sensors*, 1998. 33

[43] A. Saccomanno, A. Laudati, Z. Szillasi, N. Beni, A. Cutolo, A. Irace, M. Giordano, S. Buontempo, A. Cusano, and G. Breglio. **Long-Term Temperature Monitoring in CMS Using Fiber Optic Sensors**. *Sensors Journal, IEEE*, **12**(12):3392–3398, Dec. 2012. 33

[44] **LHC Experiments Prepare for Summer Conferences**. *[online] Available: http://www.cern.ch*. 34

[45] F. Berghmans, O. Deparis, A. F. Fernandez, Y. Defosse, P. Megret, M. Decreton, and M. Blondel. **High total dose radiation effects on temperature sensing fiber Bragg gratings**. *IEEE Photon. Technol. Lett., vol. 11, pp. 1159-1161*, 1999. 35

[46] A. Gusarov, D. S. Starodubov, F. Berghmans, O. Deparis, Y. Defosse, A. F. Fernandez, M. Decreton, P. Megret, and M. Blondel. **Comparative study of MGy dose level $\gamma$-radiation effect on FBGs written in different fibres**. *Proc.SPIE, vol. 3746, pp. 608-611*, 1999. 35

[47] A. F. Fernandez, F. Berghmans, O. Deparis, A. F. Fernandez, Y. Defosse, P. Megret, M. Decreton, and M. Blondel. **Radiation-resistant WDM optical link for thermonuclear fusion reactor instrumentation**. *Proc. RADECS, pp. 1708-1712*, 2000. 35

[48] D. L. Griscom. **$\gamma$-ray-induced optical attenuation in Ge-doped-silica optical-fiber waveguides**. *J. Appl.Phys., vol. 78, no. 11, pp. 6696-6704*, 1995. 35

[49] D. Griscom. **Optical properties and structure of defects in silica glass**. *J. Ceram. Soc. Jpn., vol. 99, no. 1154, pp. 899-916*, 1991. 35

[50] K. O. Hill, B. Malo, F. Bilodeau, D. Johnson, and J. Albert. **Bragg gratings fabricated in a monomode photosensitive optical fibre by UV exposure through a phase mask**. *Appl. Phys. Lett., vol. 62, no. 10, pp. 1035-1037*, 1993. 35

[51] A.D. Kersey, M. A. Davis, T. A. Berkoff, D. G. Bellemore, K. P. Koo, and R. T. Jones. **Progress toward the development of practical fiber Bragg grating instrumentation systems**. *Proc. SPIE, vol. 2839, pp. 40-63*, 1996. 35

[52] A. Othonos and K. Kalli. **Fiber Bragg Gratings: Fundamentals and Applications in Telecommunications and Sensing**. *Accademic Press*, 1999. 35

[53] P. C. Peng, H. Y. Tseng, and S. Chi. **Long-distance FBG sensor system using a linear-cavity fiber Raman laser scheme**. *IEEE Photon. Technol. Lett., vol. 16, pp. 575-577*, 2004. 35, 42

[54] Y.J. Rao. **In-fibre Bragg grating sensors**. *Meas. Sci. Technol., vol. 8, no. 4, pp. 355-375*, 1997. 35, 42

[55] Z. Szillasi, S. Buontempo, N. Beni, G. Breglio, A. Cusano, A. Laudati, M. Giordano, A. Saccomanno, D. Druzhkinh, and A. Tsirou. **One year of FOS measurements in CMS experiment at CERN**, 2011. 38

[56] Y. Zhao and Y. Liao. **Discrimination methods and demodulation techniques for ber Bragg grating sensors**. *Optics and Lasers in Engineering*, **41**:1–18, 2004. 42

[57] A.D. Kersey et al. **Fiber Grating sensors**. *J. Lightwave Technol.*, **15**:1442–1462, 1997. 42

[58] F. Berghmans et al. **Radiation hardness of ber-optic sensors for monitor ing and remote handling applications in nuclear environments**. *Proc. SPIE*, **3538**:28–39, 1998. 42

[59] F. Berghmans and A. Gusarov. **Fiber Bragg grating sensors in space and nuclear environments, in Fiber Bragg Gratings Sensors: Thirty Years from Research to Market**. *A. Cusano, A. Cutolo, and J. Albert, Editors. Bentham Publishing.* 42

[60] A. Cusano et al. **Applications of modern FOS techniques in high energy particle physic detectors for the LHC at CERN**. *5th European Workshop on Structural Health Monitoring, Sorrento*, 2010. 43

[61] J. H. Lee, J. H. Kim, Y. G. Han, S. H. Kim, , and S. B. Lee. **Investigation of Raman fiber laser temperature probe based on fiber Bragg gratings for long distance remote sensing applications**. *Opt. Express*, **12**:1747–1752, 2004. 44

[62] **Micron Optics technical sheet**. *[online] Available: http://www.micronoptics.com.* 44

[63] R. Arcidiacono et al. **CMS DCS design concepts**. *ICALEPCS 2005*, 2005. 49

[64] **DIM, a Portable, Light Weight Package for Information Publishing, Data Transfer and Inter-process Communication**. *International Conference on Computing in High Energy and Nuclear Physics, Padua*, 2000. 49

[65] **ETM, PVSII**. *[online] Available: http://www.etm.at.* 49

[66] **JCOP framework**. *[online] Available: http://itcobe.web.cern.ch/.* 49

[67] G. Riddone and R. Trant. **The compound cryogenic distribution line for the LHC: status and prospects**. *paper presented at ICEC19, Grenoble, France*, 2002. 56

[68] Ph. Lebrun, G. Riddone, L. Tavian, and U. Wagner. **Demands in refrigeration capacity for the Large Hadron Collider**. *Proc. ICEC16, Elsevier Science, Oxford, UK*, pages 95–98, 1997. 57

[69] J. A. Agapito, J. Casas-Cubillos, A. Fernandes, F. J. Franco, I. Goncalves, and A. H. Cachero et al. **Rad-Tol Pt-100 Isolation Amplifiers for the LHC Cryogenic System**. 10th *Workshop on Electronics for LHC and Future Experiments, Boston, MA, USA*, pages 402–406, 1997. 58

[70] S. S. Courts and P.R. Swinehart. **Rad-Tol Pt-100 Isolation Amplifiers for the LHC Cryogenic System**. *Advances in Cryogenics Engineering*, **45**, 1999. 58

[71] S. Gupta, T. Mizunami, T. Yamao, and T. Shimomura. **Fibre Bragg grating cryogenic temperature sensor**. *Appl. Opt.*, **35**:5202–5206, 1996. 60

[72] M. B. Reid and M. Ozcan. **Temperature dependence of fibre optic Bragg gratings at low temperatures**. *Opt. Eng.*, **37**:237–240, 1998. 60

[73] S. W. James et al. **Strain response of fibre Bragg grating sensors at cryogenic temperatures**. *Meas. Sci. Technol.*, **13**(10), 2002. 62

[74] I. Latka et al. **Fiber-optic Bragg gratings as magnetic field-insensitive strain sensors for the surveillance of cryogenic devices**. *Cryogenics*, **49**:490–496, 2009. 62

[75] J. Roths, G. Andrejevic, R. Kuttler, and M. Suβer. **18th International optical fiber sensors conference, Optical Society of America**. *Calibration of fiber Bragg cryogenic temperature sensors*, 2006. 62, 76

[76] T. Mizunami, H. Tathata, and H. Kawashima. **High sensitivity cryogenic fibre-Bragg grating temperature sensors using Teflon substrates**. *Meas. Sci. Technol.*, **12**:914–917, 2001. 62

[77] R. Rajini, M. Suesser, K. G. Narayankhedkar, G. Krieg, and M. D. Atrey. **Performance evaluation of metal-coated fiber Bragg grating sensors for sensing cryogenic temperature**. *Cryogenics*, **48**:142–147, 2008. 62

[78] A. Saccomanno, G. Breglio, A. Irace, M. Bajko, Z. Szillasi, S. Buontempo, M. Giordano, and A. Cusano. **A calibration method based on look-up-table for cryogenic temperature Fiber Bragg Grating sensors**, 2012. 80

[79] M. Esposito, S. Buontempo, A. Petriccione, M. Zarrelli, G. Breglio, A. Saccomanno, Z. Szillasi, A. Makovec, A. Cusano, A. Chiuchiolo, M. Bajko, and M. Giordano. **Fiber Bragg Grating sensors to measure the coefficient of thermal expansion of polymers at cryogenic temperatures**, 2012. 91

[80] M. Giordano, N. Beni, A. Makovec, Z. Szillasi, M. Bajko, S. Buontempo, M. Esposito, A. Petriccione, G. Breglio, A. Saccomanno, A. Chiuchiolo, and A. Cusano. **Strain and Temperature Monitoring at Cryogenic Operative Conditions**, 2012. 91

[81] ABB AB. *Outdoor instrument transformers. Buyer's Guide.* ABB AB, 2006. 94

[82] J. Lenz and A. S. Edelstein. **Magnetic Sensors and Their Applications**, 2006. 94, 95, 97

[83] S.A. Macintyre. *Magnetic Field Measurement.* CRC Press LLC, 2000. 95, 96

[84] J. Heremans. **Solid State Magnetic Field Sensors and Application**. *Applied Physics*, **26**:1149–1168, 1993. 95

[85] P. L. Richards. **Bolometric detectors for measurements of the cosmic microwave background**. *Journal of Superconductors*, **17**:545–550, 2004. 96

[86] H. G. Meyer et al. **SQUID technology for geophysical exploration**. *Phys. Stat. Sol. C*, **5**:1504–1509, 2005. 96

[87] **Current and future technologies for biomagnetism**, 2004. 96

[88] Emerging Technologies Working Group and Fiber Optic Sensors Working Group. **Optical current transducers for power systems: A review**. *IEEE Trans. Power Delivery*, **9**:1778–1788, 1994. 96

[89] A. H. Rose, S. M. Etzel, and K. B. Rochford. **Optical fiber current sensors in high electric field environments**. *Journal of Lightwave Technology*, **17**:1042–1048, 1999. 96

[90] A. Yariv and H. V. Winsor. **Proposal for detection of magnetic fields through magnetostrictive perurbation of optical fiber**. *Optics Letters*, **5**(3):87–89, 1980. 98

[91] J. P. Willson and R. E. Jones. **Magnetostrictive fiber-optic sensor system for detecting DC magnetic fields**. *Optics Letters*, **8**(6):333–335, 1980. 98

[92] A. E. Clark. **Magnetostrctive rare earth Fe2 compounds in Ferromagnetic materials**. **1**:531–589, 1980. 98

[93] J. Tellinen, I. Suorsa, A. Jskelinen, I. Aaltio, and K. Ullakko. $8^{th}$ *international conference ACTUATOR, Bremen Germany*, 2002. 98

[94] D. J. Feng, G. Y. Kao, and Q. D. Zhao et al. **Study on the electric current sensor of fiber Bragg grating**. *Journal of Infrared and Millimeter Waves*, **20**(4):241–243, 2001. 98

[95] B. Yi and B.C.B. Chu et al. **Temperature compensation for a fiber-Bragg-grating-based magnetostrictive sensor**. *Microwave and Optical Technology Letters*, **36**(3):211–213, 2003. 98

[96] K.S. Chiang, R. Kancheti, and V. Rastogi. **Temperature compensated Fiber Bragg grating based magnetostrictive sensor for DC and AC currents**. *Optical Engineering*, **42**:1906, 2003. 98, 106

[97] Y. Q. Liu, K. S. Chiang, and P. L. Chu. **Multiplexing of Temperature-compensated fiber Bragg grating magnetostrictive sensors with a dual wavelength pulse laser**. *IEEE Photonics Technology Letters*, **16**(2):572–574, 2004. 98

[98] D. Satpathi, J.A. Moore, and M.G. Ennis. **Design of a terfenol-D based fiber-optic current transducer**. *IEEE Sensors Journal*, **5**:1057, 2005. 98

[99] J. Mora, L. Martinez-Leon, A. Diez, J. L. Cruz, and M. V. Andres. **Simultaneous temperature and AC-current measurements for high voltage lines using fiber Bragg gratings**. *Sensors and Actuators A*, **125**(5):313–316, 2006. 98

[100] **Handbook of Giant Magnetostrictive Materials**. *Academic Press*, 2000. 98, 100

[101] M. A. Krasnoselskii and A. V. Pokrovskii. *Systems with Hysteresis*. Springer-Verlag, 1989. 99

[102] I. D. Mayergoyz. *Mathematical Models of Hysteresis*. Springer, 1991. 99

[103] J.L. Cruz M.V. Andres J. Mora, A. Diez. **A magnetostrictive sensor interrogated by fiber gratings for DC-current and temperature discrimination**. *IEEE Photonics Technology Letters*, **12**:1680–1682, 2000. 106

[104] C. Shi, J. Chen, G. Wu, X. Li, J. Zhou, and F. Ou. **Stable dynamic detection scheme for magnetostrictive fiber optic interferometric sensors**. *Optics Express*, **14**:5098–5102, 2006. 106

[105] M. Yang, J. Dai, C. Zhou, and D. Jiang. **Optical fiber magnetic field sensors with TbDyFe magnetostrictive thin films as sensing materials**. *Optics Express*, **17**:20777–20782, 2009. 106

[106] N. Itoh, H. Minemoto, D. Ishiko, and S. Ishizuka. **Optical magnetic field sensor with high linearity using Bi-substituted rare earth iron garnet**. *IEEE Transaction on Magnetism*, **31**:3191–3193, 1995. 106

[107] O. Kamada, T. Nakaya, and S. Higuchi. **Magnetic field optical sensors using Ce:YIG single crystals as a Faraday element**. *Sensors and Actuators A*, **119**:345–348, 2005. 106

[108] H. Lin and S.C. Huang. **Fiber-optics multiplexed interferometric current sensors**. *Sensors and Actuators A*, **121**:333–338, 2005. 106

[109] T. Liu, X. Chen, D. Yun, J. Zhang, X. Li, and J. Chen. **Tunable magneto-optical wavelength filter of long-period fiber grating with magnetic fluids**. *Applied Physics Letters*, **2007**:1–3, 91. 106, 108

[110] L. Martinez, F. Cecelja, and R. Rakowski. **A novel magneto-optic magnetic fluid material for sensor applications**. *Sensors and Actuators A*, **123**:438–443, 2005. 106

[111] J. Dai, M. Yang, X. Li, H. Liu, and X. Tong. **Magnetic field sensor based on magnetic fluid clad etched fiber Bragg grating**. *Optical Fiber Technology*, **17**:210–213, 2011. 106

[112] A.D. Kersey, M.A. Davis, H.J. Patrick, M. LeBlac, K.P. Koo, C.G. Askins, M.A. Putnam, and E.J. Friebele. **Fiber grating sensors**. *Journal of Lightwave Technology*, **15**:1442–1463, 1997. 106

[113] R.E. Rosensweig. *Ferrohydrodynamics.* Cambridge University Press, Cambridge, 1985. 107

[114] Y. Laiqiong, Z. Luji, and Y. Jixiao. **Study of preparation and properties on magnetization and stability for ferromagnetic fluids**. *Materials Chemistry and Physics*, **66**:6–9, 2000. 107

[115] J. Huang, R. Zhao, H. Wang, W.Q. Zhao, and L.Y. Ding. **Immobilization of glucose oxidase on $Fe_3O_4/SiO_2$ magnetic nanoparticles**. *Biotechnology Letters*, **6**:817–821, 2010. 107

[116] E. Tombacz, A. Majzik, Zs. Horvat, and E. Illes. **Magnetite in aqueous medium: coating its surface and surface coated with it**, 2006. 107

[117] C. Scherer and A.M. Figueiredo Neto. **Ferrofluids: properties and applications**. *Brazilian Journal of Physics*, **35**(3a):718, 2005. 107

[118] B.G. Hyde and S. Andersson. *Inorganic Crystal Structures.* Wiley and Sons, New York, 1989. 107

[119] O. Brunke and S. Odenbach. **In situ observation and numerical calculations of the evolution of metallic foams**. *Journal of Physics: Condensed Matter*, **18**(28):6493, 2006. 107

[120] S.Y. Yang, Y.F. Chen, H.E. Horng, C.-Y. Hong, W.S. Tse, and H.C. Yang. **Magnetically-modulated refractive index of magnetic fluid films**. *Applied Physics Letters*, **81**:4931–4933, 2002. 108

[121] H.E. Horng, C.-Y. Hong, S.Y. Yang, and H.C. Yang. **Designing the refractive indices by using magnetic fluids**. *Applied Physics Letters*, **15**:2434–2436, 2003. 108

[122] C.-Y. Hong, S.Y. Yang, H.E. Horng, and H.C. Yang. **Control parameters for the tunable refractive index of magnetic fluid films**. *Journal of Applied Physics*, **94**:3849–3852, 2003. 108

[123] S. Sun and H. Zeng. **Size-Controlled Synthesis of Magnetite Nanoparticles**. *Journal of Applied Chemical Society*, **124**:8204, 2002). 108

[124] R. Vijayakumar, Y. Koltypin, I. Felner, and A. Gedanken. **Sonochemical synthesis and characterization of pure nanometer-sized $Fe_3O_4$ particles**. *Material Science and Engineering A*, **286**:101, 2000. 108

[125] R. Kornak, D. Niznansky, K. Haimann, W. Tylus, and K. Maruszewski. **Synthesis of magnetic nanoparticles via the sol-gel technique**. *Materials Science*, **23**(1):87, 2005. 108

[126] W.W. Wang, Y.J. Zhu, and M.L. Ruan. **Microwave-assisted synthesis and magnetic property of magnetite and hematite nanoparticles**. *Journal of Nanoparticle Research*, **9**:419–426, 2007. 108

[127] C.R. Lin, Y.M. Chu, and S.C. Wang. **Magnetic properties of magnetite nanoparticles prepared by mechanochemical reaction**. *MAterials Letters*, **60**(4):447–450, 2006. 108

[128] M. Gotic, T. Jurkin, and S. Music. **Factors that may influence the micro-emulsion synthesis of nanosize magnetite particles**. *Colloid and Polymer Science*, **285**(7):793, 2007. 108

[129] M. Zhang, B.L. Cushing, and C.J. OConnor. **Synthesis and characterization of monodisperse ultra-thin silica-coated magnetic nanoparticles**. *Nanotechnology*, **19**, 2008. 108

[130] Y. Hou, J. Yu, and S. Gao. **Solvothermal reduction synthesis and characterization of superparamagnetic magnetite nanoparticles**. *Journal of Material Chemistry*, **13**:1983, 2003. 108

[131] M. Racuciu. **Synthesis protocol influence on aqueous magnetic fluid properties**. *Current Applied Physics*, **9**:1062–1066, 2009. 108

[132] Yong Zhao, Ri qing Lv, Yu Ying, and Qi Wang. **Hollow-core photonic crystal fiber FabryPerot sensor for magnetic field measurement based on magnetic fluid**. *Optics & Laser Technology*, **44**(4):899–902, 2012. 108

[133] H. Kumazaki, Y. Yamada, H. Nakamura, , and S. I. K. Hane. **Tunable wavelength filter using a Bragg grating fiber thinned by plasma etching**. *IEEE Photonics Technology Letters*, **13**(11):1206–1208, 2001. 109

[134] M. Monerie. **Propagation in doubly clad single-mode fibers**. *IEEE Journal of Quantum Electronics*, **18**(4):381–388, 1982. 111, 112

[135] S. Kawakami and S. Nishida. **Characteristics of a doubly clad optical fiber with a low-index inner cladding**. *IEEE Journal of Quantum Electronics*, **10**(10):879–887, 1974. 111

[136] A. Saccomanno, A. Irace, A. Cusano, M. Giordano, and G. Breglio. **On the design of a clad-etched fiber Bragg grating sensor for magnetic field sensing applications**, 2013. 114